U.PORTO
FEUP FACULDADE DE ENGENHARIA
UNIVERSIDADE DO PORTO

Analysis of mode II and mixed mode I-II in fracture and fatigue:

A numerical and experimental study

José Baganha Marques

Dissertation submitted to
Faculdade de Engenharia da Universidade do Porto
for the degree of:

Mestre em Engenharia Mecânica

Advisor: Prof. Sérgio M. O. Tavares
Co-Advisor: Prof. Paulo M. S. Tavares de Castro

Departamento de Engenharia Mecânica
Faculdade de Engenharia da Universidade do Porto

Porto, 2018

The work presented in this dissertation was performed at the
Department of Mechanical Engineering
Faculty of Engineering
University of Porto
Porto, Portugal.

José Baganha Marques
E-mail: em10012@fe.up.pt

Faculdade de Engenharia da Universidade do Porto
Departamento de Engenharia Mecânica
Rua Dr. Roberto Frias s/n
4200-465 Porto
Portugal

Abstract

The present work consists of a numerical and experimental study concerning fracture mechanics and fatigue problems.

The aim of this work is to analyse fatigue crack propagation under pure mode II and mixed mode I-II loading conditions. For this effect bidimensional numerical simulations were carried out using models created with ABAQUS software, where the results obtained were compared with theoretical results, when possible, and experimental data. The models created in ABAQUS made use of the conventional finite element method in order to predict the stress intensity factors at the crack tip and the extended finite element method to predict the crack propagation path.

The experimental tests were performed on a single edge notch specimen, manufactured and pre-cracked following certain standards, under an asymmetrical four-point bending set up. By varying the position of supports and loads relativily to the crack several situations of mixed mode loading I-II and pure mode II were achieved.

The equivalent stress intensity factor for mixed mode I-II and pure mode II was calculated using the finite element method and ABAQUS software. The $da/dN = f(\Delta K_{eq})$ for the used material was obtained and compared with the mode I Paris law equation for the given material and NASGRO material database.

The agreement between numerical and experimental results for the situations studied was not very high. Several factors like pre-existing flaws in the material, accumulation of experimental and/or post-processing errors and roughness-induced crack closure may have played a part in the differences obtained between the experimental material curve based on K_{eq} and the NASGRO and Paris law equations based upon K_I. It is however noted that other authors also found some difference in the da/dN *versus* ΔK_{eq} or *versus* ΔK_I relationships.

Keywords: Fracture mechanics, Fatigue, Mixed mode loading I-II, Mode II loading, Stress intensity factor, Extended finite element method

Resumo

O presente trabalho consiste num estudo numérico e experimental relativamente à fadiga e mecânica da fratura.

O objectivo é analisar a propagação de fendas de fadiga em condições de carregamento em modo II puro e modo misto. Para este efeito foram feitas simulações numéricas de modelos bidimensionais criados no software ABAQUS, sendo os resultados obtidos comparados com resultados analíticos, quando possivel, e dados obtidos experimentalmente. Os modelos criados recorrem ao método dos elementos finitos convencional para efetuar a determinação dos fatores de intensidade de tensão na ponta da fenda e ao método dos elementos finitos estendido para prever a trajetória da fenda.

Os procedimentos experimentais foram efectuados num provete de flexão em quatro pontos, onde foi feita uma pré-fenda segundo determinadas normas. O ensaio de flexão de quatro pontos foi feito com uma configuração assimétrica, que permite, através da variação dos apoios e cargas, relativamente ao plano da fenda, induzir solicitações de modo II puro e modo misto I-II.

Os fatores de intensidade de tensão para modo misto I-II e modo II puro foram calculados numéricamente recorrendo ao método dos elementos finitos e software ABAQUS. A curva $da/dN = f(\Delta K_{eq})$ para o material utilizado foi traçada com base nos dados obtidos e comparada com a lei de Paris e dados da NASGRO do material em questão, para modo I.

Não foi atingida uma concordância elevada entre a curva obtida experimentalmente e as curvas relativas à lei de Paris e NASGRO do material. Vários factores podem ter contribuído para isto, como a pré-existência de defeitos no material e a acumulação de erros de natureza experimental e de pós-processamento. A possibilidade da ocorrência de fecho de fenda induzido por rugosidade superficial pode também ser uma possível causa para a diferença obtida. Nota-se, contudo, que outros autores também encontraram algumas diferenças nas relações da/dN *versus* ΔK_{eq} ou *versus* ΔK_I.

Palavras-Chave: Mecânica da fratura, Fadiga, Modo misto I-II, Modo II, Fator de intensidade de tensão, Método dos elementos finitos estendido

Acknowledgements

I would like to express my deepest gratitude to my advisor Professor Sérgio Tavares and to my co-advisor Professor Paulo Tavares de Castro for all the motivation, assistance, guidance and valuable insight during the realization of this thesis. I would also like to thank Engineers Miguel Figueiredo and Rui Silva for all the patience, availability and crucial help with all the experimental work.

List of acronyms

AA - Aluminum Association

ASTM - American Society of Mechanical Engineers

BSI - British Standards Institution

CPS4 - Four-node plane stress element without reduced integration

CPS4R - Four-node plane stress element with reduced integration

CPS8 - Eight-node plane stress element without reduced integration

CPS8R - Eight-node plane stress element with reduced integration

ISO - International Organization for Standardization

MTS - Maximum tangential stress

MERR - Maximum energy release rate

SED - Strain energy density

SIF(s) - Stress intensity factor(s)

VCCT - Virtual crack closure technique

xFEM - Extended Finite Element Method

Contents

Abstract i

Resumo ii

Acknowledgements v

List of acronyms vii

1 Fracture mechanics basic concepts 1
- 1.1 Stress analysis of cracks . . . 1
- 1.2 Stress intensity factors under mixed mode loading . . . 2
- 1.3 Crack tip plasticity . . . 4
- 1.4 Fatigue crack propagation . . . 4
  - 1.4.1 Paris law . . . 5
- 1.5 Energy release rate . . . 5
  - 1.5.1 Constant load *vs* constant displacement . . . 6
- 1.6 Equivalent stress intensity factor . . . 7
  - 1.6.1 Irwin's model . . . 7
  - 1.6.2 The maximum energy release rate model . . . 7
  - 1.6.3 Richard's model . . . 7
  - 1.6.4 Tanaka's model . . . 8
- 1.7 Crack growth under mixed mode I-II loading . . . 8
  - 1.7.1 Erdogan and Sih criterion . . . 9
  - 1.7.2 Sih criterion . . . 9
  - 1.7.3 Richard criterion . . . 10
  - 1.7.4 J.G. Williams . . . 10
- 1.8 Crack growth under Mode II loading . . . 12
  - 1.8.1 Specimens for mode II and mixed mode I-II loading testing . . . 12
- 1.9 The J integral . . . 16
- 1.10 Virtual Crack Closure Technique . . . 17

2 Mixed mode fracture with four-point bending test 19

3 Tested Material AA 6082-T6 25
- 3.1 Material properties - AA 6082-T6 . . . 25
  - 3.1.1 Mechanical properties . . . 25
  - 3.1.2 Fatigue properties . . . 25

4 Preliminary studies **29**
4.1 Case study 1 - Mode I crack growth in infinite plate . . . 29
4.1.1 Analytical solution for crack displacements . . . 29
4.1.2 Analytical solution for crack mode I stress intensity factor along an infinite cracked plate with central transverse crack . . . 30
4.1.3 ABAQUS modeling . . . 30
4.1.4 Results: Crack nodal displacements . . . 31
4.1.5 Results: Crack mode I stress intensity factor for infinite plate . . . 33
4.1.6 Results: Crack mode I stress intensity factor for finite plate . . . 33
4.2 Case study 2: Inclined crack - crack growth path and mixed mode SIFs . . 35
4.2.1 SIF determination in plate with inclined crack . . . 36
4.2.2 Analytical soltion for the mixed mode SIFs in a plate with a inclined crack . . . 36
4.2.3 ABAQUS modeling . . . 37
4.2.4 Results: SIFs for inclined crack in infinite plate . . . 38
4.2.5 Determination of crack growth direction and SIFs in mixed mode loading through the MERR and MTS criteria . . . 42
4.2.6 ABAQUS modeling . . . 43
4.2.7 Results: SIFs and crack propagation direction for inclined crack in infinite plate . . . 44

5 Experimental procedure: pre-crack **47**
5.1 Pre-crack load according to BS DD 19:1972 . . . 47
5.2 Pre-crack load according to ASTM:E399 . . . 48
5.3 Pre-crack load according to ISO 12135-2016 . . . 50
5.4 Pre-crack results after three-point bending . . . 50
5.4.1 Surface polish . . . 51

6 Experimental procedures, results and discussion **53**
6.1 Pure Mode II loading: Experimental set up and fatigue load calculation . . 53
6.1.1 Shear force and bending moment diagrams . . . 57
6.1.2 Numerical model: Crack propagation path . . . 60
6.1.3 Discussion . . . 62
6.2 Mixed mode I-II loading ($\beta = 13°$): Experimental set up and fatigue load calculation . . . 63
6.2.1 Shear force and bending moment diagrams . . . 65
6.2.2 Numerical model: Crack propagation path . . . 66
6.2.3 Discussion . . . 68
6.3 Mixed mode I-II loading ($\beta = 48°$): Experimental set up and fatigue load calculation . . . 69
6.3.1 Shear force and bending moment diagrams . . . 70
6.3.2 Numerical model: Crack propagation path . . . 71
6.3.3 Discussion . . . 73
6.4 Mixed mode I-II loading ($\beta = 70°$): Experimental set up and fatigue load calculation . . . 74
6.4.1 Shear force and bending moment diagrams . . . 76
6.4.2 Numerical model: Crack propagation path . . . 77
6.4.3 Discussion . . . 78
6.5 Equivalent stress intensity factor determination . . . 79

7 Conclusions **91**

References **92**

Annex **96**

A Pre study case 1 ABAQUS models **97**

B Pre study case 2 ABAQUS models **105**

C Experimental procedures ABAQUS models **115**

List of Figures

1.1 Definition of the coordinate axis ahed of a crack tip, [5]. 1
1.2 Stress singularity at crack tip, [5]. 2
1.3 Three modes of loading that can be applied to a crack, [5]. 2
1.4 Irwin plastic zone correction, [5]. 4
1.5 Typical fatigue crack grwoth behaviour in metals, [5]. 5
1.6 Linear-elastic load-displacement relation dependent on crack length, [7]. . . 6
1.7 Plate under tensile stress with an inclined crack of length $2a$, [8]. 8
1.8 Stress field in polar coordinates, [8]. 9
1.9 Crack deflection angle under mixed mode loading ($\phi_0 = \psi_0$), [12]. 10
1.10 Crack propagation in the angled crack problem, [16]. 11
1.11 Relation between $\frac{K_I}{K_{II}}$ and ψ_0, [17]. 11
1.12 Fatigue crack growth for mode II loading on the initial crack, [12]. 12
1.13 Specimens for mixed mode experiments, [18]. 13
1.14 a - Specimen for mode II loading. b - Device for load application [12]. . . . 15
1.15 a - Specimen for mixed mode tests. b - Device with load application angle α, [12]. 15
1.16 Flat surfaced notch in 2D deformation field [19]. 16
1.17 Crack closure method for 2D, 4 node element, [20]. 17
1.18 Crack closure method for 2D, 8 node elements, [20]. 18

2.1 Four-point bend specimen under asymmetric loading (I-II mixed mode fracture) [21]. 19
2.2 Mixed-mode geometry factors Y_I and Y_{II} [21]. 20
2.3 Correction factor for mode II intensity factor [22]. 21
2.4 Adimensional SIFs *vs* load distance from crack plane 21
2.5 β *vs* load distance from crack plane 22
2.6 Four-point bend specimen under symmetric loading (pure mode I fracture) [21]. 23
2.7 Four-point bend specimen under asymmetric loading (load in crack plane ($B = t$)) [24]. 23

3.1 Crack growth curves of various materials for R=0.1, [12]. 26
3.2 NASGRO material fitting curve for R=0.1, [32]. 27
3.3 NASGRO material fitting curve for R=-1, R=0.1, R=0.5, [32]. 28

4.1 Cracked in infinite body under tensile stress, [17]. 29
4.2 Plate model for the currrent case study (W=H), [33]. 30
4.3 Cracked in infinite body under tensile stress 31
4.4 Displacements along the crack plane 32
4.5 Mesh 1 crack using CPS4R elements 32

4.6 Mesh 1 crack using CPS4 elements 32
4.7 Mesh 3 crack using CPS8R elements 33
4.8 Mesh 3 crack using CPS8R elements $a = 1$ mm 35
4.9 Mesh 3 crack using CPS8R elements $a = 2$ mm 35
4.10 Mesh 3 crack using CPS8R elements $a = 3$ mm 35
4.11 Infinite plate under tensile stress with an inclined crack, [33]. 36
4.12 Infinite plate under tensile stress with an inclined crack used in case study 2, [35]. 37
4.13 Infinite plate with inclined crack $\alpha = 15°$ 38
4.14 Infinite plate with inclined crack $\alpha = 15°$ 38
4.15 Plate with inclined crack $\alpha = 60°$, $\Delta a = 0$ 39
4.16 Plate with inclined crack $\alpha = 60°$, $\Delta a = 0.5$ using MTS criteria 39
4.17 Plate with inclined crack $\alpha = 60°$, $\Delta a = 1$ using MTS criteria 39
4.18 Plate with inclined crack $\alpha = 60°$, $\Delta a = 0.5$ using MERR criteria 41
4.19 Plate with inclined crack $\alpha = 60°$, $\Delta a = 1$ using MTS criteria 41
4.20 Analytical mode I SIF *vs* SIFs obtained via ABAQUS 41
4.21 Analytical mode II SIF *vs* SIFs obtained via ABAQUS 42
4.22 Plate under tensile load with inclined crack ($\Delta K_v = \Delta K_e$), [12]. 42
4.23 ABAQUS sketch for the first increment $\Delta a = 0.5$ mm 43
4.24 ABAQUS sketch for the second increment $\Delta a = 1$ mm 44
4.25 ψ_0 *vs* β relation 45
4.26 Crack propagation direction obtained by ABAQUS (MTS criteria) 46
4.27 Crack propagation direction obtained by ABAQUS (MERR criteria) 46

5.1 Single edge notch specimen. 47
5.2 Test pieces dimensitions according to BS DD 19:1972, [36]. 48
5.3 Notch details and minimum fatigue pre-cracking requirements, [38]. 49
5.4 Cracking deviation limits, [38]. 51

6.1 Experimental set up for four-point bend specimen under asymmetric loading (mode II loading). 53
6.2 Experimental set up for four-point bend specimen under asymmetric loading (mode II loading). 54
6.3 Experimental set up for four-point bend specimen under asymmetric loading (mode II loading). 55
6.4 Single edge notch bending specimen 1 set up sketch. 55
6.5 Single edge notch bending specimen (W=35). 56
6.6 Single edge notch bending specimen with reduced width (W=28). 56
6.7 Simplified representation of the forces acting on top beam. 57
6.8 Simplified representation of the forces acting on the specimen. 58
6.9 Shear force diagram for the experimental pure mode II loading. 59
6.10 Bending moment diagram for the experimental pure mode II loading. 59
6.11 Crack path obtained with image digitizer for one face of specimen 1. 60
6.12 Crack path obtained with image digitizer for the other face of specimen 1. . 60
6.13 Crack path obtained with xFEM for coarse mesh - specimen 1. 61
6.14 Crack path obtained with xFEM for fine mesh - specimen 1. 61
6.15 Comparison between crack path obtained with xFEM for fine mesh, coarse mesh and experimental crack path - specimen 1. 61
6.16 Roughness-induced crack closure, [12]. 62

6.17 Experimental set up for four-point bend specimen number 4 under asymmetric loading (mixed mode I-II $\beta = 13°$) 63
6.18 Single edge notch bending specimen 4 set up sketch. 63
6.19 Shear force diagram for the experimental mixed mode loading I-II(β = 13.22°, $P = 46000$ N 65
6.20 Bending moment diagram for the experimental mixed mode loading I-II(β = 13.22°, $P = 46000$ N 65
6.21 Crack path obtained with image digitizer for one face of specimen 4. 66
6.22 Crack path obtained with image digitizer for the other face of specimen 4. . 66
6.23 Crack path obtained with xFEM for specimen 4. 67
6.24 Crack path obtained with xFEM specimen 4 (corrected). 67
6.25 Comparison between crack path obtained with xFEM for specimen 4 and experimental crack path. 67
6.26 Left hand side of specimen 68
6.27 Right hand side of specimen 68
6.28 Single edge notch bending specimen with reduced width (W=25 mm). . . . 69
6.29 Single edge notch bending specimen 3 set up sketch. 69
6.30 Shear force diagram for the experimental mixed mode loading I-II (β = 47.8°, $P = 21000$ N). 70
6.31 Bending moment diagram for the experimental mixed mode loading I-II ($\beta = 47.8°$, $P = 21000$ N). 70
6.32 Crack path obtained with image digitizer for one face of specimen 3. 71
6.33 Crack path obtained with image digitizer for the other face of specimen 3. . 71
6.34 Crack path obtained with xFEM for coarse mesh - specimen 3. 72
6.35 Crack path obtained with xFEM for fine mesh - specimen 3 72
6.36 Comparison between crack path obtained with xFEM for fine mesh, coarse mesh and experimental crack path - specimen 3. 72
6.37 Single edge notch bending specimen 5 initial set up sketch. 74
6.38 Single edge notch bending specimen 5 corrected set up sketch. 75
6.39 Shear force diagram for the experimental mixed mode loading I-II($\beta = 70°$, $P = 11500$ N 76
6.40 Bending moment diagram for the experimental mixed mode loading I-II(β = 70°, $P = 11500$ N 76
6.41 Crack path obtained with xFEM for coarse mesh - specimen 5 77
6.42 Crack path obtained with xFEM for fine mesh - specimen 5 77
6.43 Crack path obtained with xFEM for fine mesh - specimen 5 78
6.44 Set of chosen pictures for specimen 1 79
6.45 Plot of the coordinates obtained from image post processing - specimen 1 . 80
6.46 Mesh with 32227 linear quadrilateral elements of type CPS4 for specimen 1 - Photo 4 80
6.47 Undeformed shape for specimen 1 - Photo 4 81
6.48 Deformed shape for specimen 1 - Photo 4 81
6.49 Partition at crack tip specimen 1 - Photo 4 82
6.50 Mesh contours used for the J integral 82
6.51 Free body cut and coordinate system used for the VCCT 82
6.52 Set of chosen pictures for specimen 3 84
6.53 Plot of the coordinates obtained from image post processing - specimen 3 . 85
6.54 Mesh with 7215 linear quadrilateral elements of type CPS4 for specimen 3 - Photo 5 85

6.55 Undeformed shape for specimen 3 - Photo 5 87
6.56 Deformed shape for specimen 3 - Photo 5 87
6.57 Comparison between NASGRO material fitting curve, Paris law and points obtained from the experimental procedures post processing 88
6.58 Crack growth rate *vs* ΔK_v, [42]. 90

A.1 Mesh 1 for 1/4 plate - CPS4R 97
A.2 Mesh 1 for 1/4 plate (CPS4R) - von Mises stress 97
A.3 Mesh 1 for 1/4 plate - CPS4 98
A.4 Mesh 1 for 1/4 plate (CPS4) - von Mises stress 98
A.5 Mesh 1 for 1/4 plate - CPS8R 98
A.6 Mesh 1 for 1/4 plate (CPS8R) - von Mises stress 99
A.7 Mesh 2 for 1/4 plate - CPS4R 99
A.8 Mesh 2 for 1/4 plate (CPS4R) - von Mises stress 99
A.9 Mesh 2 for 1/4 plate - CPS8R 100
A.10 Mesh 2 for 1/4 plate (CPS8R) - von Mises stress 100
A.11 Mesh 3 for 1/4 plate - CPS4R 100
A.12 Mesh 3 for 1/4 plate (CPS4R) - von Mises stress 101
A.13 Mesh 3 for 1/4 plate - CPS8R 101
A.14 Mesh 3 for 1/4 plate ($a = 1$, CPS8R) - von Mises stress 101
A.15 Mesh 3 for 1/4 plate ($a = 2$, CPS4R) - von Mises stress 102
A.16 Mesh 3 for 1/4 plate ($a = 2$, CPS8R) - von Mises stress 102
A.17 Mesh 3 for 1/4 plate ($a = 3$, CPS4R) - von Mises stress 102
A.18 Mesh 3 for 1/4 plate ($a = 3$, CPS8R) - von Mises stress 103

B.1 Infinite plate with inclined crack $\alpha = 0°$ - Mesh 105
B.2 Infinite plate with inclined crack $\alpha = 0°$ - von Mises stress 105
B.3 Infinite plate with inclined crack $\alpha = 15°$ - Mesh 106
B.4 Infinite plate with inclined crack $\alpha = 15°$ - von Mises stress 106
B.5 Infinite plate with inclined crack $\alpha = 30°$ - Mesh 106
B.6 Infinite plate with inclined crack $\alpha = 30°$ - von Mises stress 107
B.7 Infinite plate with inclined crack $\alpha = 45°$ - Mesh 107
B.8 Infinite plate with inclined crack $\alpha = 45°$ - von Mises stress 107
B.9 Infinite plate with inclined crack $\alpha = 60°$ - Mesh 108
B.10 Infinite plate with inclined crack $\alpha = 60°$ - von Mises stress 108
B.11 Infinite plate with inclined crack $\alpha = 75°$ - Mesh 108
B.12 Infinite plate with inclined crack $\alpha = 75°$ - von Mises stress 109
B.13 Infinite plate with inclined crack $\alpha = 90°$ - Mesh 109
B.14 Infinite plate with inclined crack $\alpha = 90°$ - von Mises stress 109
B.15 Plate with inclined crack ($\alpha = 60°, \Delta a = 0.5$) using the MTS criteria - Mesh 110
B.16 Plate with inclined crack ($\alpha = 60°, \Delta a = 0.5$) using the MTS criteria - Mesh 110
B.17 Plate with inclined crack ($\alpha = 60°, \Delta a = 0.5$) using the MTS criteria - von Mises stress 110
B.18 Plate with inclined crack ($\alpha = 60°, \Delta a = 1$) using the MTS criteria - Mesh . 111
B.19 Plate with inclined crack ($\alpha = 60°, \Delta a = 1$) using the MTS criteria - Mesh . 111
B.20 Plate with inclined crack ($\alpha = 60°, \Delta a = 1$) using the MTS criteria - von Mises stress 111
B.21 Plate with inclined crack ($\alpha = 60°, \Delta a = 0.5$) using the MERR criteria - Mesh 112

B.22 Plate with inclined crack ($\alpha = 60°, \Delta a = 0.5$) using the MERR criteria - Mesh . . . 112
B.23 Plate with inclined crack ($\alpha = 60°, \Delta a = 0.5$) using the MERR criteria - von Mises stress . . . 112
B.24 Plate with inclined crack ($\alpha = 60°, \Delta a = 1$) using the MERR criteria - Mesh 113
B.25 Plate with inclined crack ($\alpha = 60°, \Delta a = 1$) using the MERR criteria - Mesh 113
B.26 Plate with inclined crack ($\alpha = 60°, \Delta a = 1$) using the MERR criteria - von Mises stress . . . 113

C.1 Specimen 1 Mesh (CPS4 elements) - Pre-crack . . . 115
C.2 Specimen 1 Mesh (CPS4 elements) - Pre-crack (undeformed) . . . 115
C.3 Specimen 1 Mesh (CPS4 elements) - Pre-crack (deformed) . . . 116
C.4 Specimen 1 Mesh (CPS4 elements) - Photo 1 . . . 116
C.5 Specimen 1 Mesh (CPS4 elements) - Photo 1 (undeformed) . . . 116
C.6 Specimen 1 Mesh (CPS4 elements) - Photo 1 (deformed) . . . 117
C.7 Specimen 1 Mesh (CPS4 elements) - Photo 2 . . . 117
C.8 Specimen 1 Mesh (CPS4 elements) - Photo 2 (undeformed) . . . 117
C.9 Specimen 1 Mesh (CPS4 elements) - Photo 2 (deformed) . . . 118
C.10 Specimen 1 Mesh (CPS4 elements) - Photo 3 . . . 118
C.11 Specimen 1 Mesh (CPS4 elements) - Photo 3 (undeformed) . . . 118
C.12 Specimen 1 Mesh (CPS4 elements) - Photo (deformed) . . . 119
C.13 Specimen 1 Mesh (CPS4 elements) - Photo 4 . . . 119
C.14 Specimen 1 Mesh (CPS4 elements) - Photo 4 (undeformed) . . . 119
C.15 Specimen 1 Mesh (CPS4 elements) - Photo (deformed) . . . 120
C.16 Specimen 3 Mesh (CPS4 elements) - Pre-crack . . . 120
C.17 Specimen 3 Mesh (CPS4 elements) - Pre-crack (undeformed) . . . 120
C.18 Specimen 3 Mesh (CPS4 elements) - Pre-crack (deformed) . . . 121
C.19 Specimen 3 Mesh (CPS4 elements) - Photo 1 . . . 121
C.20 Specimen 3 Mesh (CPS4 elements) - Photo 1 (undeformed) . . . 121
C.21 Specimen 3 Mesh (CPS4 elements) - Photo 1 (deformed) . . . 122
C.22 Specimen 3 Mesh (CPS4 elements) - Photo 2 . . . 122
C.23 Specimen 3 Mesh (CPS4 elements) - Photo 2 (undeformed) . . . 122
C.24 Specimen 3 Mesh (CPS4 elements) - Photo 2 (deformed) . . . 123
C.25 Specimen 3 Mesh (CPS4 elements) - Photo 3 . . . 123
C.26 Specimen 3 Mesh (CPS4 elements) - Photo 3 (undeformed) . . . 123
C.27 Specimen 3 Mesh (CPS4 elements) - Photo 3 (deformed) . . . 124
C.28 Specimen 3 Mesh (CPS4 elements) - Photo 4 . . . 124
C.29 Specimen 3 Mesh (CPS4 elements) - Photo 4 (undeformed) . . . 124
C.30 Specimen 3 Mesh (CPS4 elements) - Photo 4 (deformed) . . . 125
C.31 Specimen 3 Mesh (CPS4 elements) - Photo 5 . . . 125
C.32 Specimen 3 Mesh (CPS4 elements) - Photo 5 (undeformed) . . . 125
C.33 Specimen 3 Mesh (CPS4 elements) - Photo 5 (deformed) . . . 126

List of Tables

3.1 Mechanical properties of the aluminium alloy 6082-T6. 25

4.1 Meshes used for case study 1 31
4.2 Mode I SIF for infinite plate using diferent elements/meshes 33
4.3 Difference between VCCT and J integral methods with analytical solution-infinite plate 34
4.4 Mode I SIF for crack increment on finite plate 34
4.5 Difference between VCCT and J integral methods with analytical solution - finite plate 34
4.6 Dimensions and material properties for study case 2 36
4.7 K_I,K_{II} for different inclined cracks 40
4.8 Differences obtained relative to the analytical solution 40
4.9 Mesh partitions and respective seedsize 43
4.10 SIFs for various Δa increments with $\alpha = 60°$ 44
4.11 SIFs for various Δa increments with $\alpha = 60°$ 45
4.12 Differences between MTS and MERR criteria with analytical solutions . . . 45

5.1 Pre-crack dimensions 51

6.1 Data for the fatigue tests for specimen 1 under pure Mode II loading 57
6.2 Data for the fatigue test for specimen 4 under mixed mode I-II loading ($\beta = 13°$) 64
6.3 Data for the fatigue test for specimen 3 under mixed mode I-II loading ($\beta = 48°$) 69
6.4 Data for the fatigue tests for specimen 5 under mixed mode I-II loading ($\beta = 70°$) 74
6.5 Data for the fatigue test for specimen 5 under mixed mode I-II loading ($\beta = 70°$) 75
6.6 Mode I SIFs for specimen 1 - J integral 83
6.7 Mode II SIFs for specimen 1 - J integral 83
6.8 Mode I and Mode II equivalent SIFs for specimen 1 83
6.9 Values of the equivalent SIFs and the correspondent $\frac{da}{dN}$ for specimen 1 . . . 84
6.10 Mode I SIFs specimen 3 - J integral 86
6.11 Mode II SIFs for specimen 3 - J integral 86
6.12 Mode I and Mode II equivalent SIFs for specimen 3 86
6.13 Values of the equivalent SIFs and the correspondent $\frac{da}{dN}$ for specimen 3 . . . 88

Chapter 1

Fracture mechanics basic concepts

1.1 Stress analysis of cracks

The presence of notches in mechanical components when these are subjected to external forces and exposed to harsh enviroments leads to the appearence and growth of cracks. Westergaard [1], Irwin [2], Sneddon [3], Williams [4], published solutions to some cracked configurations under certain loads. Considering a polar coordinate axis with the origin at the crack tip (figure 1.1), it can be shown that the stress field in a linear elastic cracked body is given by [5],

$$\sigma_{ij} = \left(\frac{k}{\sqrt{r}}\right) f_{ij}(\theta) + \sum_{m=0}^{\infty} A_m r^{\frac{m}{2}} g_{ij}^{(m)}(\theta) \tag{1.1}$$

where,

- σ_{ij} – stress tensor
- k - constant
- f_{ij} - dimensionless function of θ in the leading term
- r and θ - defined in figure 1.1

For the higher order terms, A_m is the amplitude and $g_{ij}(m)$ is a adimensional function of θ for the mth term. The higher order terms depend on geometry but any solution to the stress field is proportional to $\frac{1}{\sqrt{r}}$. So when positioned at the crack tip, $r \longrightarrow 0$, the first term of the equation tends to infinity, thus the stress near the tip also tends to infinity. In this way, equation 1.1 describes a stress singularity at the crack tip [5].

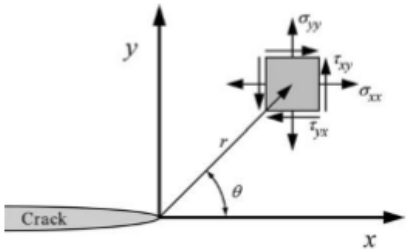


Figure 1.1: Definition of the coordinate axis ahed of a crack tip, [5].

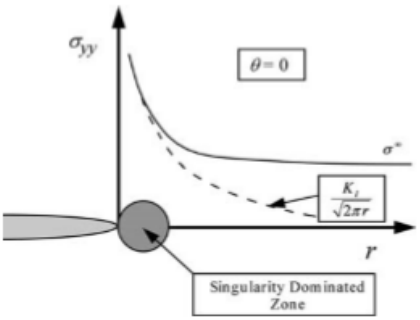


Figure 1.2: Stress singularity at crack tip, [5].

1.2 Stress intensity factors under mixed mode loading

In a cracked body there are three basic modes of loading that can be applied to the crack region: Mode I, Mode II and Mode III loading.

In Mode I loading, also called opening mode, the principal load is normal to the crack surface and the displacements of the crack surface are perpendicular to the crack plane.

In Mode II loading, or shear mode, one face tends to slide with respect to the other due to in-plane shear loading. The displacements occour in the crack plane and normal to the leading edge of the crack.

Mode III, or tear mode, is caused by out-of-plane shear. The displacements of the crack surface take place in the crack plane parallel to the leading edge of the crack, [5, 6].

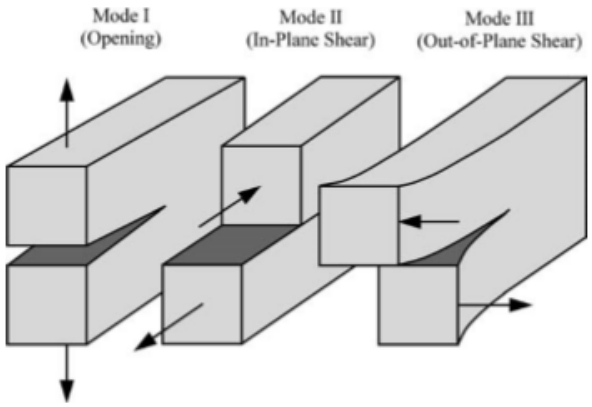


Figure 1.3: Three modes of loading that can be applied to a crack, [5].

The stress intensity factor is usually given a subscript to denote the mode of loading, i.e., K_I, K_{II}, K_{III} [5].The whole stress field at the crack tip is known when the stress intensity factor is known [6]. In another words, the SIFs reflect the redistribuition of stresses in a body due to the introduction of a crack [7].

For a linear elastic isotropic material the stress fields for mode I and II are given as [5] [6] [8], respectively,

$$\begin{cases} \sigma_{xx} = \dfrac{K_I}{\sqrt{2\pi r}} \cos\dfrac{\theta}{2}\Big[1 - \sin\dfrac{\theta}{2}\sin\dfrac{3\theta}{2}\Big] \\ \sigma_{yy} = \dfrac{K_I}{\sqrt{2\pi r}} \cos\dfrac{\theta}{2}\Big[1 + \sin\dfrac{\theta}{2}\sin\dfrac{3\theta}{2}\Big] \\ \tau_{xy} = \dfrac{K_I}{\sqrt{2\pi r}} \cos\dfrac{\theta}{2}\sin\dfrac{\theta}{2}\sin\dfrac{3\theta}{2} \end{cases} \tag{1.2}$$

$$\begin{cases} \sigma_{xx} = -\dfrac{K_{II}}{\sqrt{2\pi r}} \sin\dfrac{\theta}{2}\Big[2 + \cos\dfrac{\theta}{2}\cos\dfrac{3\theta}{2}\Big] \\ \sigma_{yy} = \dfrac{K_{II}}{\sqrt{2\pi r}} \sin\dfrac{\theta}{2}\sin\dfrac{\theta}{2}\cos\dfrac{3\theta}{2} \\ \tau_{xy} = \dfrac{K_{II}}{\sqrt{2\pi r}} \cos\dfrac{\theta}{2}\Big[1 - \sin\dfrac{\theta}{2}\sin\dfrac{3\theta}{2}\Big] \end{cases} \tag{1.3}$$

$$\begin{cases} \sigma_{zz} = 0 & \text{(plane stress)} \\ \sigma_{zz} = \upsilon(\sigma_{xx} + \sigma_{yy}) & \text{(plane strain)} \\ \tau_{xz}, \tau_{yz} = 0 \end{cases} \tag{1.4}$$

The stress intensity factors are related to the strain energy release rate (G), being [9],

$$G = \frac{1}{E'}\left(K_I^2 + K_{II}^2\right) + \frac{1}{2\mu}K_{III}^2 \tag{1.5}$$

Where μ is the shear modulus and,

$$\begin{cases} E' = E & \text{(plane stress)} \\ E' = \dfrac{E}{(1-\nu^2)} & \text{(plane strain)} \\ \mu = \dfrac{E}{2(1-\nu)} \end{cases} \tag{1.6}$$

From equation 1.5 the relationships between the strain energy release rate and each stress intensity factor.

In case of pure mode I loading ($K_{II} = 0$ and $K_{III} = 0$) the relationship between the K_I and G_I is given by,

$$G_I = \frac{K_I^2}{E'} \tag{1.7}$$

For pure mode II ($K_I = 0$ and $K_{III} = 0$),

$$G_{II} = \frac{K_{II}^2}{E'} \tag{1.8}$$

And finally for pure mode III ($K_I = 0$ and $K_{II} = 0$),

$$G_{III} = \frac{1}{2\mu}K_{III}^2 \tag{1.9}$$

1.3 Crack tip plasticity

The elastic stress field solutions (1.2, 1.3) assume a stress singularity exists at the tip of an elastic crack. Typically materials, especially metals, tend to exhibit a yield stress above which they deform plastically [6]. This implies that there exists a region around the tip of a crack where plastic deformation occurs and hence a stress singularity cannot exist, this region is known as the crack tip plastic zone.

In order to account for this effect Irwin introduced a plastic zone correction by considering a crack of a somewhat larger size, since he argued that the occurrence of plasticity makes the crack behave as if it was longer than its actual physical length [6].

So the physical crack size a is replaced by a longer crack with size $a + r_y$ allowing the plasticity to be accounted for, making the elastic stress field solutions (1.2, 1.3) still applicable. According to [5] r_y can be defined by,

$$r_y = \frac{1}{2\pi}\left(\frac{K}{\sigma_{yield}}\right)^2 \quad \text{(Plane stress)} \tag{1.10}$$

$$r_y = \frac{1}{6\pi}\left(\frac{K}{\sigma_{yield}}\right)^2 \quad \text{(Plane strain)} \tag{1.11}$$

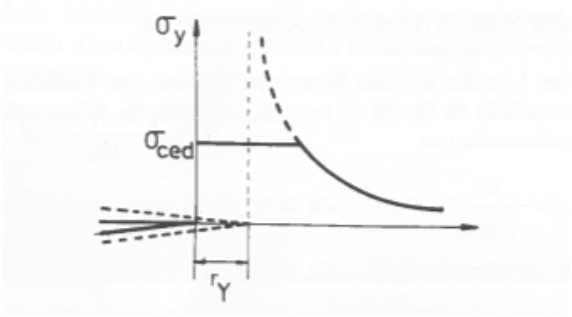


Figure 1.4: Irwin plastic zone correction, [5].

It is worth noting that the model assumes the plastic zone has a circular shape [6]. For pratical aplications the Irwin plastic zone should not be used [5], (page 63), it is included in this section to provide context to the analysis of crack tip behavior in linear fracture mechanics.

1.4 Fatigue crack propagation

Fatigue is the phenomenon associated with the weakening of a material due to repeatedly applied loads, therefore knowing how a material behaves under a cyclic load and the capability of estimating its life time are extremelly important aspects in engineering.

Fatigue crack caracterization is made using specimens, with a known K value, which are under cyclic loading. The crack propagation along the cycles is measured using optic or electric processes and all the information is represented by the curve $\ln(\frac{da}{dN})$ *vs* $ln\Delta K$.

Figure 1.5 can be divided in three distinct regions. In region I the propagation velocity is extremelly low, and the crack doesn't grow bellow the threshold value (ΔK_{th}). Region II is where the stable crack propagation takes place, in this region the slope of the curve, when represented in a logarithmic scale, is very close to being linear and can be described by the Paris law. Lastly, region III is where the unstable crack propagation occurs, where

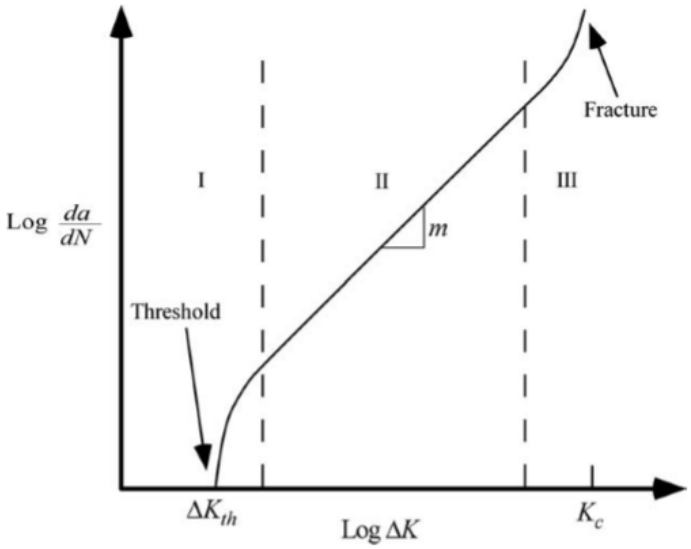


Figure 1.5: Typical fatigue crack grwoth behaviour in metals, [5].

crack growth takes place even for a small number of cycles. The upper limit of this region is given by ΔK_c, that represents the fracture toughness of the brittle materials or the plastic collapse of ductile materials.

1.4.1 Paris law

The Paris law, proposed by Paul Paris, is an empirical equation 1.12 that describes the behavior of crack growth in region II displayed in figure 1.5. Through the use of this law, its possible to determine the number of cycles needed to propagate a crack from an initial dimension of a_0 to a_f. This allows engineers to estimate how many cycles a cracked structure can withstand until failure due to fatigue.

$$\frac{da}{dN} = C \times \Delta K^m \tag{1.12}$$

The Paris law is usually displayed in a logaritimic scale and is independent of crack size and load amplitude, depending only on ΔK and constants C and m. Theese constants, on the other hand, depend on the load ratio value R ($R = \frac{\sigma_{min}}{\sigma_{max}}$)).

1.5 Energy release rate

According to Griffith's theory the energy release rate per crack tip, G, also called the crack extension force or crack driving force [6], is defined by,

$$G = -\frac{dU}{dA} \tag{1.13}$$

Where U is the strain energy and $dA = Bda$ is the growth of the crack surface. The B corresponds to the thickness and da to half the length of the crack.

The condition for crack growth can also be written as,

$$\frac{d(F-U)}{da} = \frac{dW}{da} \tag{1.14}$$

Where $F = Pv$, which is the work produced by a force P, v the displacement of the points exposed to that load and W is the energy required to make the crack grow. In other words the first term of equation 1.14 represents the avaiable force to cause cracking and the second term the resistance to cracking [7].

1.5.1 Constant load *vs* constant displacement

Considering a plate with thickness B, under a force P in which the displacements from the points under loading are v. If the crack is growing a small quantity (da) then the displacements also grow dv. One can therefore say the work caused by the load P is Pdv, so,

$$G = \frac{d(F-U)}{da} = \frac{1}{B}\Big(P\frac{dv}{da} - \frac{dU}{da}\Big) \tag{1.15}$$

As long as there is no crack growth, it can be considered that the displacement v is proportional to the load [7] meaning,

$$v = CP \tag{1.16}$$

Where C is the flexibility constant or the compliance of the system [7]. On the other side the strain energy stored by the plate is,

$$U = \frac{1}{2}Pv = \frac{1}{2}CP^2 \tag{1.17}$$

Meaning,

$$G = \frac{1}{B}\Big(P^2\frac{dC}{da} + CP\frac{dP}{da} - \frac{1}{2}P^2\frac{dC}{da} - CP\frac{dP}{da}\Big) = \frac{P^2}{2B}\frac{dC}{da} \tag{1.18}$$

Since the term $\frac{dP}{da}$ disappeared one can say G isn't a function of the variation of the load.

A graphical representation of the curve P *vs* v is shown on figure 1.6 for an elastic body with two different crack lengths a and $a + da$ being the last length (da) an infinitesimal increment of the crack.

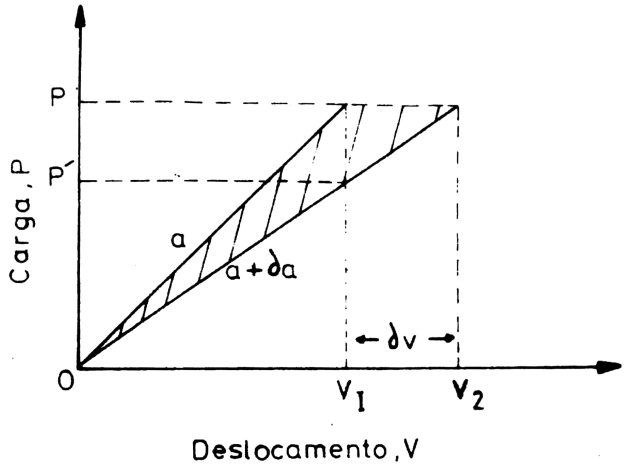


Figure 1.6: Linear-elastic load-displacement relation dependent on crack length, [7].

With a constant displacement $v = v_1$ the growth of the crack from a to $a + da$ lowers the strain energy stored by the body, going from $\frac{1}{2}Pv_1$ to $\frac{1}{2}P'v_1$. The body with the longest crack behaves like a weaker spring and the other a stronger one. To achieve the same displacement the weakest spring requires a lower load, storing less strain energy, being the released energy $\frac{1}{2}v_1(P - P')$.

With a constant force P the weaker spring will display larger displacements compared to the stronger one, leading to a higher strain energy, $\frac{1}{2}Pv_2 > \frac{1}{2}Pv_1$. However the weaker spring moved and additional distance $v_2 - v_1$ meaning the energy $P(v_2 - v_1)$ was not stored. The variation of total potencial energy is given by,

$$\frac{1}{2}Pv_1 - \left[\frac{1}{2}Pv_2 - P(v_2 - v_1)\right] = \frac{1}{2}P(v_2 - v_1) \tag{1.19}$$

So the energy released is equal to $\frac{1}{2}P(v_2 - v_1)$ and it corresponds to the traced area on figure 1.6, which is equal to $GBda$ [7].

In sum, for constant displacement $dv = CdP$ and for constant load $dv = dCP$, either way results in $\frac{P^2}{2B}\frac{dC}{da}$. The energy release rate is independent of the load P, meaning this equation is of high importance for linear elastic fracture mechanics because it can be applied in any case.

1.6 Equivalent stress intensity factor

The equivalent stress itensity factor, K_e, is an important variable used to correlate crack behavior when a cracked structure is under mixed mode loading.

1.6.1 Irwin's model

According to [2] the equivalent stress intensity factor at the crack tip can be described by,

$$K_e = \sqrt{K_I^2 + K_{II}^2} \tag{1.20}$$

1.6.2 The maximum energy release rate model

According to [10] the combined or equivalent stress intensity factor at the crack tip can be obtained by,

$$\begin{cases} K_e = \sqrt{E \cdot G} & \text{(plane stress)} \\ K_e = \sqrt{\dfrac{E \cdot G}{(1 - \upsilon^2)}} & \text{(plane strain)} \end{cases} \tag{1.21}$$

Using the stress intensity factor for every mode presented in equations 1.7, 1.8 and 1.9 combined with equation 1.21, K_e is equal to,

$$\begin{cases} K_e = \sqrt{(K_I^2 + K_{II}^2) + (1 + \upsilon) \cdot K_{III}^2} & \text{(plane stress)} \\ K_e = \sqrt{(K_I^2 + K_{II}^2) \cdot (1 - \upsilon^2) + (1 + \upsilon) \cdot K_{III}^2} & \text{(plane strain)} \end{cases} \tag{1.22}$$

1.6.3 Richard's model

Richard in [11] presents a equivalent stress intensity factor for mixed mode I-II loading,

$$K_e = \frac{K_I}{2} + \frac{1}{2}\sqrt{K_I^2 + 4(\alpha_1 K_{II}^2)} \tag{1.23}$$

Consequently the unstable crack growth occurs when $K_e > K_{Ic}$ for mode I. Richard also states that if the material parameter α_1 is set to 1.155 the approximation of the fracture limit curve of the maximum tangencial stress criterion is excellent [11].

On a more recent work [12] the equivalent stress intensity factor for mixed mode I-II loading is defined as,

$$K_e = \frac{K_I}{2} + \frac{1}{2}\sqrt{K_I^2 + 5.336K_{II}^2)} \tag{1.24}$$

1.6.4 Tanaka's model

The model proposed by Chen and Keer in [13] is as follows,

$$K_e = (K_I^4 + 8K_{II}^4)^{\frac{1}{4}} \tag{1.25}$$

1.7 Crack growth under mixed mode I-II loading

In practice structures are subjected to more than one loading mode, in this section the combination of mode I and II loading also named mixed mode loading I-II is going to be addressed. An inclined crack problem is depicted in figure 1.7.

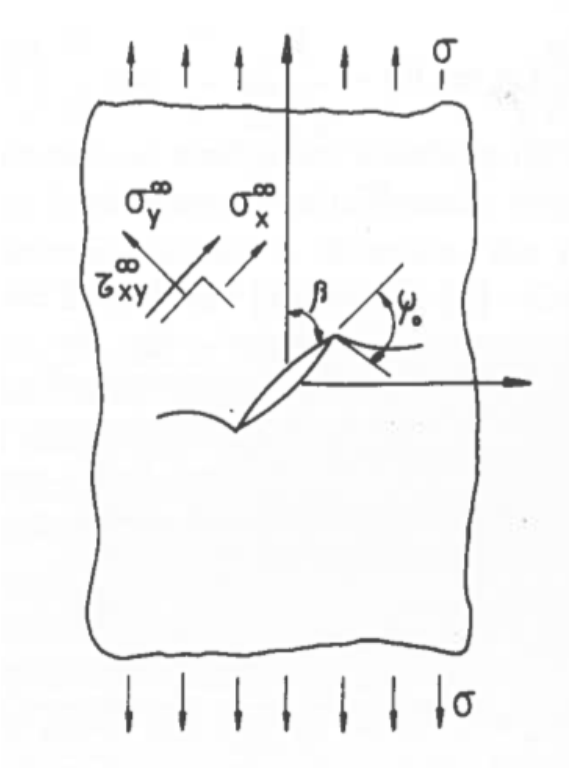


Figure 1.7: Plate under tensile stress with an inclined crack of length $2a$, [8].

The crack, in practice, tends to propagate in a direction orthogonal to the normal stress because it tends to propagate in the path of least resistence or the path that allows the maximum release of energy. One of the most widely used criterion for the initial crack growth direction is the Maximum Tangential Stress (MTS) criterion [14] which states the direction of crack growth occurs in a direction perpendicular to the maximum principal

stress [6, 14, 15]. Another heavily used criteria is that the crack growth will take place in the direction of Maximum Energy Release Rate (MERR) and that the growth occurs where the Strain Energy Density (SED) is minimum.

In mixed mode loading (mode I and II) the near field solution for the stress distribution (plane stress) at the crack front are [5],

$$\sigma_r = \frac{K_I}{4\sqrt{2\pi r}}\Big[5\cos\frac{\theta}{2} - \cos\frac{3\theta}{2}\Big] - \frac{K_{II}}{4\sqrt{2\pi r}}\Big[5\sin\frac{\theta}{2} - 3\sin\frac{3\theta}{2}\Big] \tag{1.26}$$

$$\sigma_\theta = \frac{K_I}{4\sqrt{2\pi r}}\Big[3\cos\frac{\theta}{2} + \cos\frac{3\theta}{2}\Big] - \frac{K_{II}}{4\sqrt{2\pi r}}\Big[3\sin\frac{\theta}{2} + 3\sin\frac{3\theta}{2}\Big] \tag{1.27}$$

$$\tau_{r\theta} = \frac{K_I}{4\sqrt{2\pi r}}\Big[\sin\frac{\theta}{2} + \sin\frac{3\theta}{2}\Big] + \frac{K_{II}}{4\sqrt{2\pi r}}\Big[\cos\frac{\theta}{2} - 3\cos\frac{3\theta}{2}\Big] \tag{1.28}$$

All the stress field equations are based on a polar coordinate system (figure 1.8).

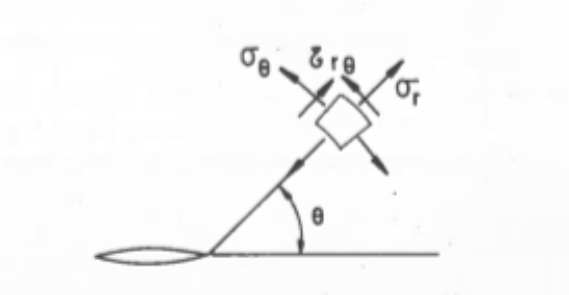


Figure 1.8: Stress field in polar coordinates, [8].

As the crack propagates in mixed mode loading I-II it will kink by the angle ψ_0 (figures 1.7 and 1.9). Several criteria to approximate the kinking angle are presented in the sub section bellow. It's also worth noting that with increasing crack growth the amount of mode II loading decreases and both the mode I and the equivalent SIFs increase, with unstable crack propagation occuring for when $K_{equivalent} \geq K_{Ic}$, where K_{Ic} represents the material fracture toughness [12].

1.7.1 Erdogan and Sih criterion

The predictions by Erdongan and Sih are based on the MTS criterion, where the crack growth starts radial from the crack tip with an angle $\theta = \psi_0$ (see figure 1.7) perpendicular to the maximum tangential stress $\sigma_{\theta,max}$. As soon as the material limiting value $\sigma_{\theta,c}$ is exceeded by $\sigma_{\theta,max}$ or the stress equivalent stress intensity factor K_e exceeds the fracture toughness K_{Ic} [11]. So the crack deflection angle is given by solving,

$$K_I \sin\psi_0 + K_{II}(3cos\psi_0 - 1) = 0 \tag{1.29}$$

Equating to,

$$\psi_0 = -\arccos\Big(\frac{3K_{II}^2 + K_I\sqrt{K_I^2 + 8K_{II}^2}}{K_I^2 + 9K_{II}^2}\Big) \tag{1.30}$$

1.7.2 Sih criterion

Sih's criterion is based on the strain energy density criterion, where the crack extends from the crack tip in the direction of the smallest energy density factor S_{min}, becoming unstable when S_{min} reaches $S_{min,c}$ which represents the material limiting value [11].

1.7.3 Richard criterion

According to Richard [11] the equivalent stress intensity factor can be given by 1.23, being that the condition for crack growth is given when K_e exceeds the fracture toughness K_{Ic} for mode one. Richard states that the determination of the crack deflection (kinking) angle ψ_0 can be given by,

$$\psi_0 = \pm\Big[155.5^\circ \frac{|K_{II}|}{|K_I| + |K_{II}|}\Big] - 83.4^\circ\Big[\frac{|K_{II}|}{|K_I| + |K_{II}|}\Big]^2 \tag{1.31}$$

Thereby a positive shear stress produces a positive K_{II} factor and a negative deflection/kink angle ψ_0 and vice versa [11] (figure 1.9),

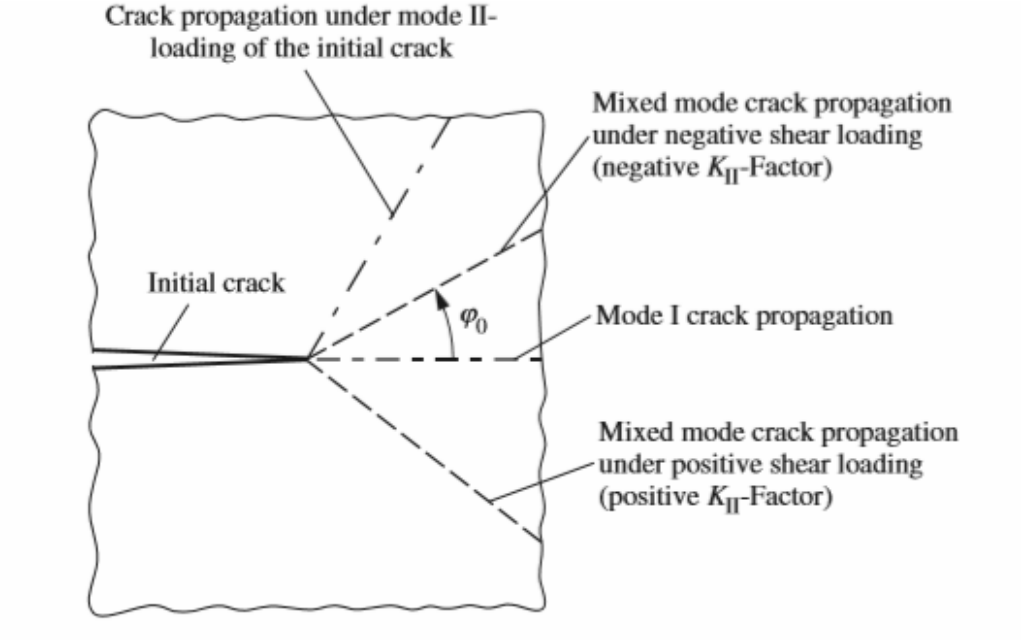


Figure 1.9: Crack deflection angle under mixed mode loading ($\phi_0 = \psi_0$), [12].

On a more recent work [12] it is stated that the crack deflection angle ψ_0, for mixed mode I-II, can be obtained by,

$$\psi_0 = \pm\Big[140^\circ \frac{|K_{II}|}{K_I + |K_{II}|}\Big] - 70^\circ\Big[\frac{|K_{II}|}{K_I + |K_{II}|}\Big]^2 \tag{1.32}$$

1.7.4 J.G. Williams

J.G Williams also looked into the inclined crack problem which is represented in 1.7 [16] [17].

The stress intensity factors, 1.7, are given by,

$$K_I = \sigma \sin^2\beta\sqrt{\pi a} \tag{1.33}$$

$$K_{II} = \sigma \sin\beta\cos\beta\sqrt{\pi a} \tag{1.34}$$

Combining 1.29 and the equations above one can obtain,

$$\cot\beta = \frac{-\sin\psi_0}{3\cos\psi_0 - 1} \tag{1.35}$$

This equation is represented in figure 1.10.

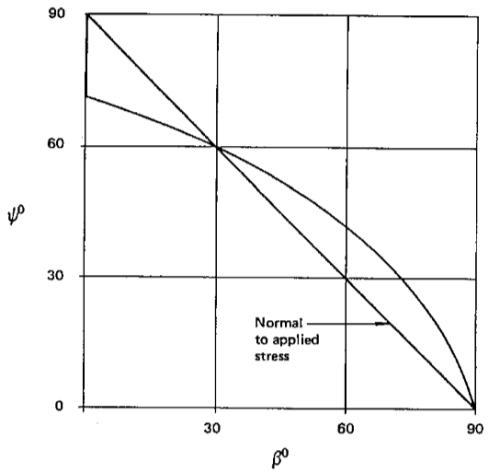


Figure 1.10: Crack propagation in the angled crack problem, [16].

When $0 < \beta < \frac{\pi}{2}$, ψ_0 is negative and the crack propagates as the curves shown in figure 1.7 [17]. Through equation 1.29 the relationship between the SIF's with the angle ψ_0 can be done by plotting $\frac{K_I}{K_{II}}$ *vs* ψ_0 when $\frac{K_I}{K_{II}} < 1$ and $\frac{K_{II}}{K_I}$ *vs* ψ_0 when $\frac{K_I}{K_{II}} > 1$. The value for ψ_0 where this transition occurs can be obtained by solving equation 1.36 [17] [16],

$$\frac{K_I}{K_{II}} = 1 \rightarrow \psi = -0.92729 = 53.13^\circ \tag{1.36}$$

This plot is showed in figure 1.11 for the MTS and SED criterion,

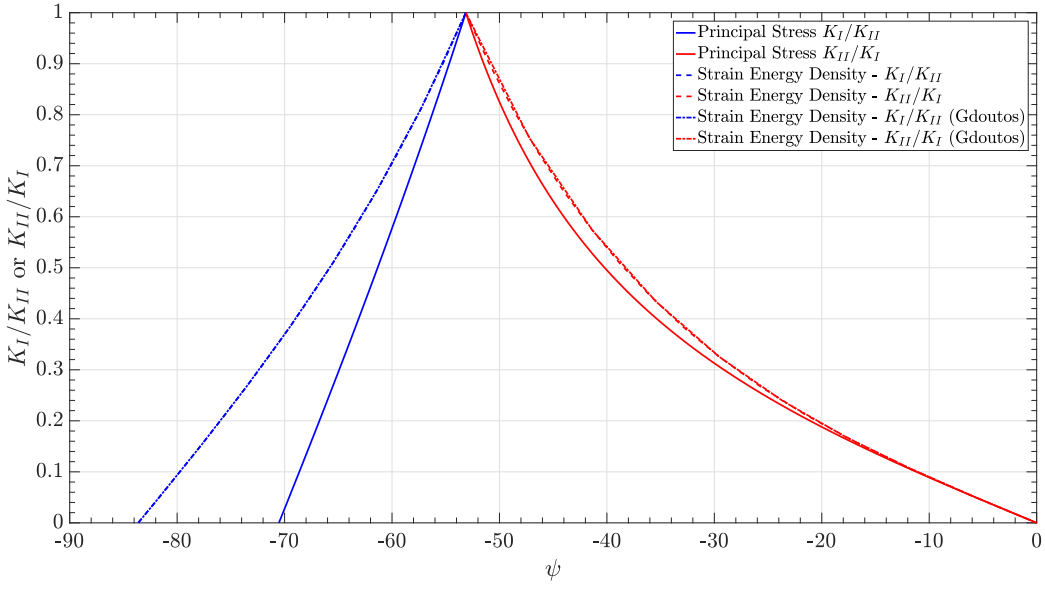


Figure 1.11: Relation between $\frac{K_I}{K_{II}}$ and ψ_0, [17].

1.8 Crack growth under Mode II loading

Similarly to pure mode I loading, a crack under pure mode II loading grows if the cyclic stress intensity factor ΔK_{II} surpasses the threshold value $\Delta K_{II,th}$. However, the mode II threshold values are generally unknown [12], so usually the risk of crack propagation can be assessed by using,

$$\Delta K_{II,th} \geq 0.87 \Delta K_{I,th} \tag{1.37}$$

During crack propagation, the loading condition changes and the mode I stress intensity factor increases turning this situation into a mixed-mode loading. The fatigue crack becomes unstable if [12],

$$\Delta K_{eq} \geq \Delta K_{Ic} \tag{1.38}$$

This situation is represented in figure 1.12,

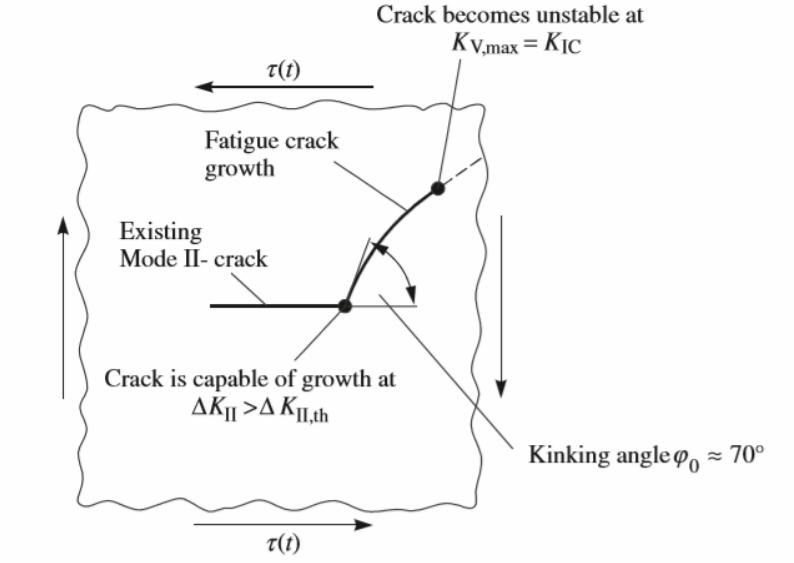


Figure 1.12: Fatigue crack growth for mode II loading on the initial crack, [12].

For pure mode II ($K_I = 0$), using equation 1.29 the crack deflection, according to [16], is,

$$\psi_0 = \cos^{-1}\left(\frac{1}{3}\right) = 70.5° \tag{1.39}$$

1.8.1 Specimens for mode II and mixed mode I-II loading testing

Standardized test specimens for mode II and mixed mode I-II still don't exist, as opposed to mode I loading. However various specimens have been sugested for this purpose.

The optimal mixed mode specimen, designed for fracture and fatigue tests should meet some criteria according to [18], that being:

- Full range of mixed mode I-II combinations;
- Compactness of the specimen;

- Simple manufacturing process;
- Ability to create fatigue pre-cracks under mode I loading;
- Clamping and loading conditions must be easy to achieve;
- Simple test procedure and evaluation;
- Realizability of a state of plane strain;
- Small minimum dimensions to give small fracture loads.

In figure 1.13 Richard [18] presents a few sugestions for mixed mode loading specimens.

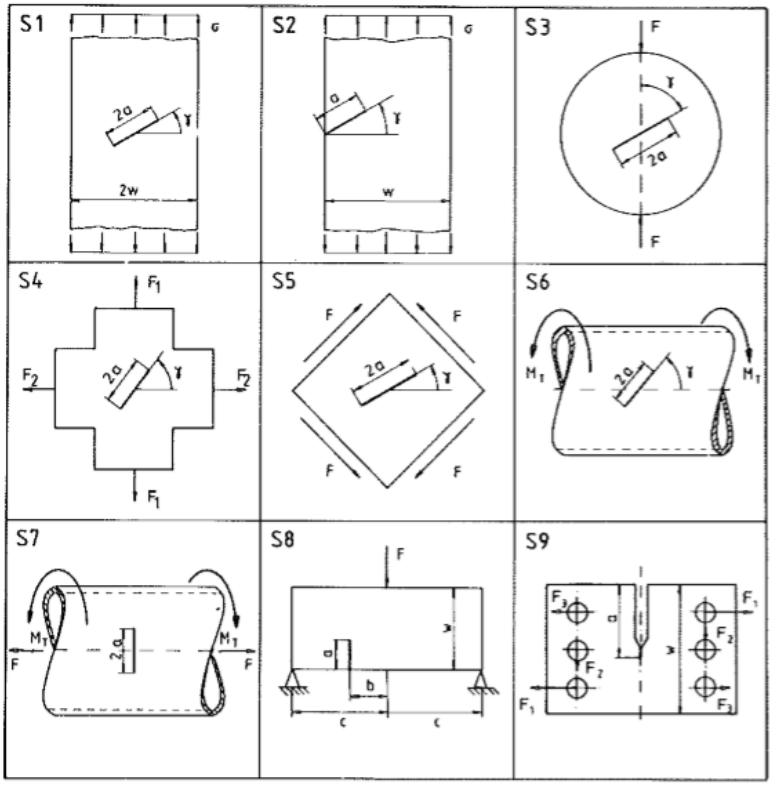


Figure 1.13: Specimens for mixed mode experiments, [18].

According to [18];

Specimen S1 consists in a plate under tensile stresses with an oblique central crack. On one hand by varying the angle γ it is possible to obtain pure mode I stresses at the crack ($\gamma = 0°$), pure mode II stresses ($\gamma = 90°$) and mixed mode stresses ($0° < \gamma < 90°$). On the other hand no transition from pure mode I to pure mode II is possible on this specimen and generating fatigue cracks would cause the crack to instantly be deflected when the tensile stresses are applied. Other problems may arise as there are two crack tips involved, which may lead to crack propagation not starting at both crack tips simultaneously. So in the end this specimen doesn't appear to be very pratical for a series of investigations.

Although specimen S2 contains only one crack tip and allows the variation of the $\frac{K_{II}}{K_I}$ ratio by changing the crack inclination angle γ, the generation of fatigue cracks on specimen S2 presents the same problems as specimen S1.

Specimen S3 is a very compact specimen that alows the transition from pure mode I stresses to pure mode II stresses in the range of $0° < \gamma < 25°$, being $\gamma = 0°$ equivalent to

pure mode I and $\gamma = 25°$ to pure mode II. However the angle range is very small and the stress intensity factors would be very sensitive to a small angle varitation which may lead to problems during testing, resulting in a loss of accuracy. The occurrence of compressive stresses is also a concern and the fracture surface may be damaged when the specimen breaks. Once again there is the presence of two crack tips, which is undesirable for the reasons stated in specimen S1.

Specimen S4 also allows the variation of $\frac{K_{II}}{K_I}$ ratio by changing the crack inclination angle γ and the force ratio $\frac{F_2}{F_1}$ acting on the specimen. It is worth noting that if F_1 and F_2 are tensile forces, no mode II stresses can be obtained in the crack, only if $F_2 = -F_1$ can mode II be generated for $\gamma = 45°$. This case creates a risk of buckling of the thin plates, and once again the presence of two crack tips is not desirable. To sum up, this specimen is extremelly tricky to work out.

Specimen S5 allows the variation of the $\frac{K_{II}}{K_I}$ ratio at will by changing the crack inclination angle γ (mode I stresses for $\gamma = 0°$ and mode II for $\gamma = 45°$). The downsides are that loading application conditions and fatigue crack generation are complicated. Furthermore, owing to the weak stress intensity field, large testing forces and specimen dimensions are required.

Specimen S6 allows the obtention of pure mode II and mode I stresses for $\gamma = 0°$ and $\gamma = 45°$ respectivly meaning the $\frac{K_{II}}{K_I}$ ratio can be varied in the range of $0 \leq \frac{K_{II}}{K_I} \leq \infty$. Specimen S6 presents several problems, for starters it is practically impossible to initiate a fatigue crack in the direction of the starter notch. To add up, for a plain stress problem the ratio between wall thickness and pipe radius has to be very small and for a plain strain problem the wall thickness would have to be large. Trying to fuffil both conditions would result in an extremely large specimen.

Specimen S7 like specimen S6 allows the variation of the $\frac{K_{II}}{K_I}$ ratio. When under tensile stresses mode I occurs, and when exposed to torsional stresses mode II occurs. But, just as specimen S6, the generation of fatigue cracks is hard and tests can only be done with the help of special machines.

Specimen S8 derives from the three-point bend specimen used to generate fatigue pre-cracks and determining K_{IC} value. Mode I stresses can be obtained for $b/c = 0$ and by varying the b/c and a/w ratios different SIFs (K_I and K_{II}) can be obtained, it is not however possible to obtain pure mode II stresses at the crack with this method. Nevertheless this specimen can be used as a four-point shear specimen with an offset crack to produce predominantly mode II stresses, while obtaining pure mode I is difficult (requires a four-point bend symmetrical set up). In the current study an asymmetrical four-point bend set up was used to induce pure mode II and mixed mode I-II, this set up will be further discussed in chapter 4. To add on, this specimen is very compact, creating a pre-cracke under mode I loading is easly done by using a three-point bend set up and it permits a state of plane strain. However, in the event of fatigue stresses, the $\frac{K_{min}}{K_{max}}$ relationship of SIF cannot become negative [18], (page 233).

Finally specimen S9 consists in a rectangular specimen with an edge crack and six holes. Using the loading device displayed in figure 1.14 b pure mode II stresses are obtained, and using the divice in figure 1.15 b, pure mode I, pure mode II and mixed mode I-II stresses can be produced. Furthermore, this specimen is very compact, provides simple loading condition, enables initiation of a pre-crack under mode I conditions with ease. However, the CTS specimen manufacturing cost is higher.

The compact shear specimen (CS specimen) shown in figure 1.14 allows the determination of the K_{IIC} [12].

For two-dimensional mixed mode loading the CTS specimen has shown to be particu-

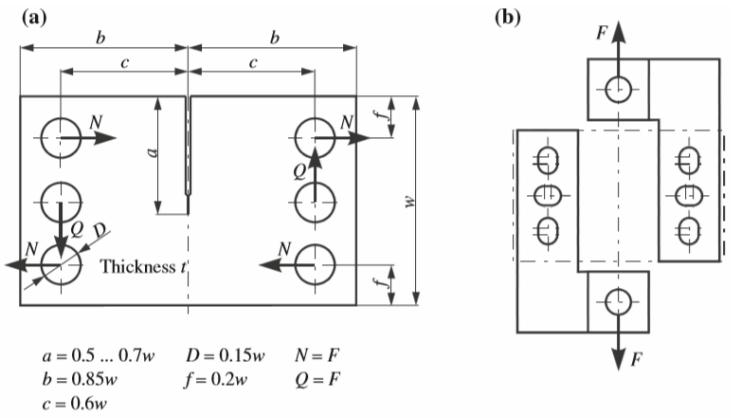


Figure 1.14: a - Specimen for mode II loading. b - Device for load application [12].

larly effective. In figure 1.15 the CTS specimen is presented along with its loading device. By rotating the specimen by an angle α various mixed mode situations can be generated ($0° < \alpha < 90°$) as well as pure mode I ($\alpha = 0°$) and pure mode II ($\alpha = 90°$) [12].

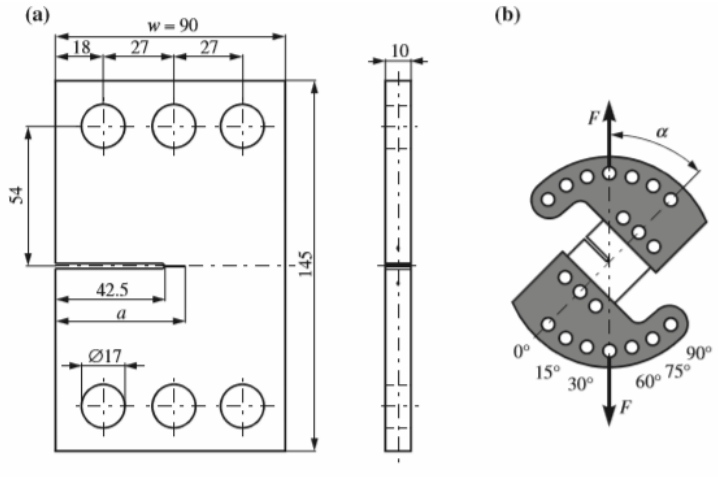


Figure 1.15: a - Specimen for mixed mode tests. b - Device with load application angle α, [12].

1.9 The J integral

The J integral is a contour integral, that can be used in linear-elastic fracture mechanics (LEFM) and elastic-plastic fracture mechanics (EPFM), to determine the energy release rate. According to [19], the J integral is independent of the path of integration around the crack, making it a path-independent integral. The two-dimensional form of the J integral can be written as,

$$J = \int_{\Gamma} (wdy - T\frac{\delta u}{\delta x} ds) \tag{1.40}$$

Where,

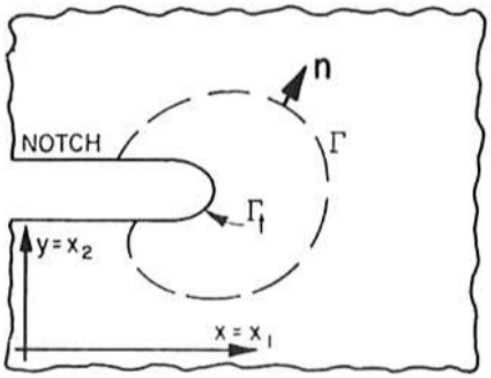


Figure 1.16: Flat surfaced notch in 2D deformation field [19].

- w – strain energy density.
- T - traction vector.
- u - displacement vector.
- ds - length increment along the contour Γ.

It was shown that the J integral as defined along a contour around the crack tip is equal to the change in potential energy for a virtual crack extension da [6]. So for linear-elastic fracture mechanics (LEFM) it means that,

$$J = -\frac{dU}{da} = G \tag{1.41}$$

1.10 Virtual Crack Closure Technique

The Virtual Crack Closure Technique, also know as VCCT, allows the determination of the stress intensity factors (K_I, K_{II}, K_{III}) through the calculation of the energy release rate (G_I, G_{II}, G_{III}, respectively).

This method is based on the premise that the energy released when a crack is extended from a to $a + \delta a$ is the same amount of energy necessary to close the crack from $a + \delta a$ to a.

The required work (ΔE) to virtually close the crack modeled with finite element methods, as presented in figure 1.17, [20], is:

$$\Delta E = \frac{1}{2}(X_i \Delta \cdot u_l + Z_i \cdot \Delta w_l) \tag{1.42}$$

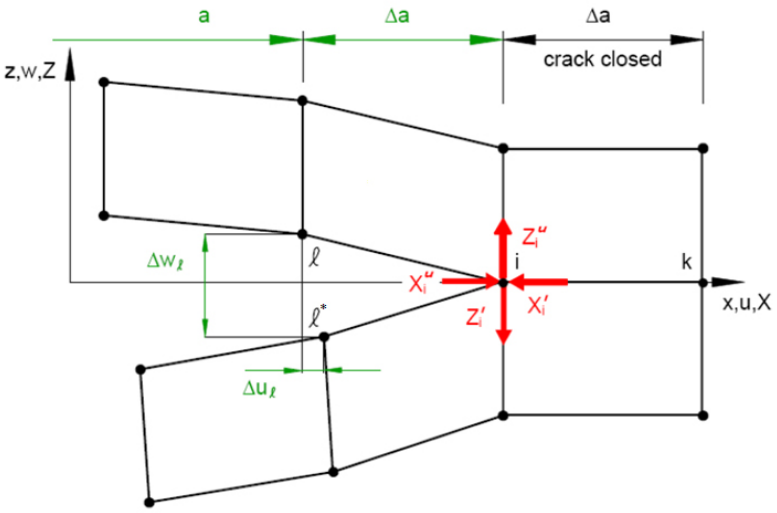


Figure 1.17: Crack closure method for 2D, 4 node element, [20].

Where,

- X_i e Z_i are the nodal reactions x and z on the nodal point i
- Δu_l e Δw_l - are the nodal displacements x and z of the nodal point l

The energy release rate is given by the variation of the strain energy due to the crack size a,

$$G = -\frac{\partial U}{\partial a} \tag{1.43}$$

Or, through the fraction between the required work to virtually grow a crack from a to $a + \Delta a$,

$$G = -\frac{\Delta E}{\Delta A} = -\frac{\Delta E}{\Delta a \cdot b} \tag{1.44}$$

Where,

- Δ A – is the crack surface area after its growth
- b - is the plate's thickness

From equations 1.42 and 1.44 for 4 node finite elements the energy release rate for mode I and mode II for either plane strain or plane stress can be given by [20],

$$G_I = -\frac{1}{2\Delta a} Z_i \Delta w_l = -\frac{1}{2\Delta a} Z_i (w_l - w_{l*}) \tag{1.45}$$

$$G_{II} = -\frac{1}{2\Delta a} X_i \Delta u_l = -\frac{1}{2\Delta a} X_i (u_l - u_{l*}) \tag{1.46}$$

Where,

- Δa - is the length of the element at the crack front.
- u_l e w_l - are the upper displacements x and z, repectivly, at node l.
- u_{l*} e w_{l*} - are the lower displacements x and z, repectivly, at node l.

For an 8 node finite element the procedure follows the same logic as in the previous case, considering figure 1.18, according to [20] it can be said that,

$$G_I = -\frac{1}{2\Delta a} [Z_i (w_l - w_{l*}) + Z_j (w_m - w_{m*})] \tag{1.47}$$

$$G_{II} = -\frac{1}{2\Delta a} [X_i (u_l - u_{l*}) + X_j (u_m - u_{m*})] \tag{1.48}$$

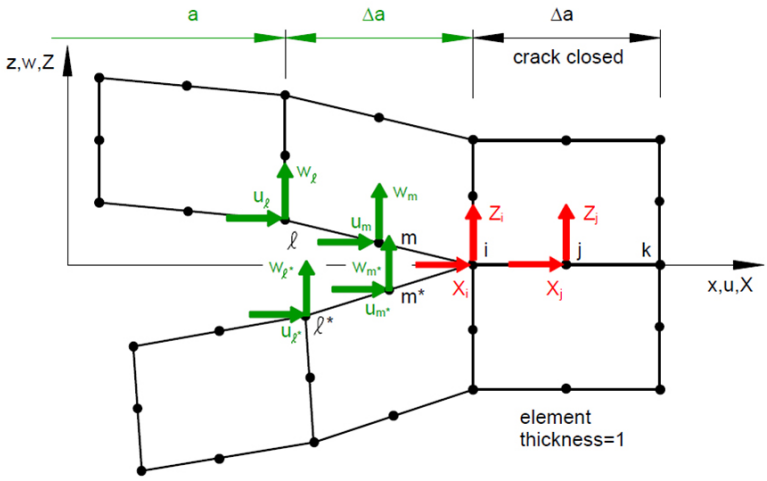


Figure 1.18: Crack closure method for 2D, 8 node elements, [20].

The stress intensity factors for mode I and II, K_I and K_{II} respectivly, can be determined for plane stress/strain using equations 1.7, 1.8 along with,

$$\begin{cases} E' = E & \text{(plane stress)} \\ E' = \dfrac{E}{1-\nu^2} & \text{(plane strain)} \end{cases} \tag{1.49}$$

Chapter 2

Mixed mode fracture with four-point bending test

The asymmetrical four-point bending set up allows the study of fracture behaviors of a specimen under pure mode II and mixed mode I-II.

Using an asymmetric loading, which has the configurations displayed in figures 2.1 and 2.7, one can measure the mode II fracture toughness K_{IIc} and the mixed mode stress intensity factors K_I and K_{II} by varying the distance of the applied load P to the pre-crack plane (S_0).

Using the set up shown in figure 2.1 in order to obtain pure mode II the distance between the load P and the pre-crack plane has to be 0 ($S_0 = 0$), this corresponds to a null bending moment along the crack plane making the crack tip only exposed only to shear force.

For mixed mode analysis varying the value of S_0 will make the mode I component increase, leading to various combinations of shear force and bending moment at the crack tip. According to [21], the stress intensity factors for mixed mode loading I-II can be given by,

$$K_I = \frac{\eta Q\sqrt{\pi a}}{Wt} Y_I \tag{2.1}$$

$$K_{II} = \frac{Q\sqrt{\pi a}}{Wt} Y_{II} \tag{2.2}$$

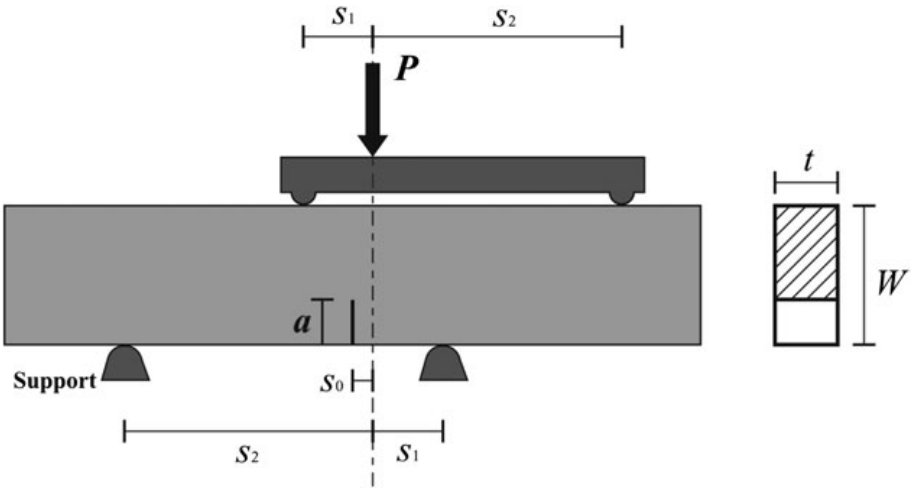


Figure 2.1: Four-point bend specimen under asymmetric loading (I-II mixed mode fracture) [21].

Where Q is the shear force at the crack tip and $Q = \frac{S_2 - S_1}{S_2 + S_1} P$ being P the applied load. The width, thickness and crack length are given by W, t and a respectivly. The relative distance of the applied load location to the pre-crack plane is given by $\eta = \frac{S_0}{W}$. Y_I and Y_{II} are the geometry factors which are functions of relative crack length $\frac{a}{W}$, and can be obtained by figure 2.2 according to [21].

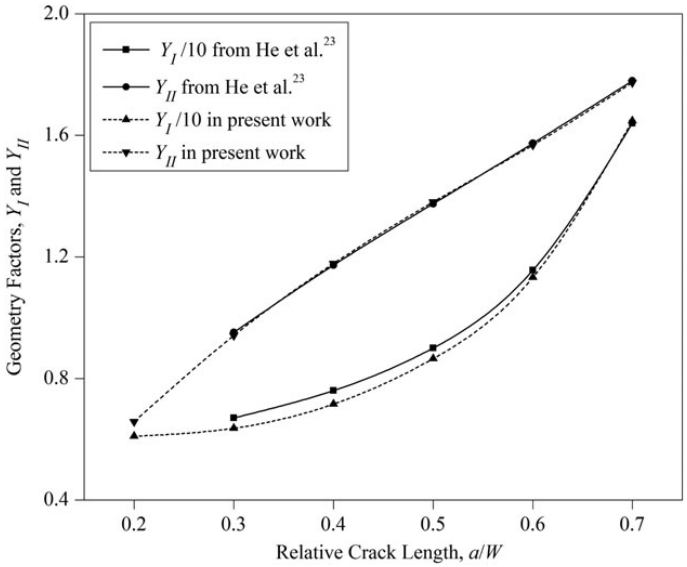


Figure 2.2: Mixed-mode geometry factors Y_I and Y_{II} [21].

The stress intensity factors, according to [22] can also be obtained through,

$$K_I = \frac{6(c - c_0) * Q}{W^2 t} \sqrt{\pi a} F_I\Big(\frac{a}{W}\Big) \tag{2.3}$$

$$K_{II} = \frac{\eta * Q}{W^{0.5} t} \frac{(\frac{a}{W})^{1.5}}{(1 - \frac{a}{W})^{0.5}} F_{II}\Big(\frac{a}{W}\Big) \tag{2.4}$$

where,

$$F_I\Big(\frac{a}{W}\Big) = \sqrt{\frac{2W}{\pi a} \tan \frac{\pi a}{2W}} \frac{0.923 + 0.199\Big(1 - \sin \frac{\pi a}{2W}\Big)^4}{\cos \frac{\pi a}{2W}} \tag{2.5}$$

or,

$$F_I\Big(\frac{a}{W}\Big) = 1.121\Big(\frac{a}{W}\Big) + 3.740\Big(\frac{a}{W}\Big)^2 + 3.873\Big(\frac{a}{W}\Big)^3 - 19.05\Big(\frac{a}{W}\Big)^4 + 22.55\Big(\frac{a}{W}\Big)^5 \tag{2.6}$$

$$F_{II}\Big(\frac{a}{W}\Big) = 7.264 - 9.37\Big(\frac{a}{W}\Big) + 2.74\Big(\frac{a}{W}\Big)^2 + 1.87\Big(\frac{a}{W}\Big)^3 - 1.04\Big(\frac{a}{W}\Big)^4 \tag{2.7}$$

According to [22] c_0 and η (figure 2.3) are correction factors that are functions of $\Big(\frac{a}{W}\Big), \Big(\frac{c}{W}\Big), \Big(\frac{s_1}{W}\Big)$ and $\Big(\frac{s_2}{W}\Big)$. Its important to note that equations 2.6 and 2.7 are only valid for $0 \leq \Big(\frac{a}{W}\Big) \leq 0.7$ and $0 \leq \Big(\frac{a}{W}\Big) \leq 1$, respectivly.

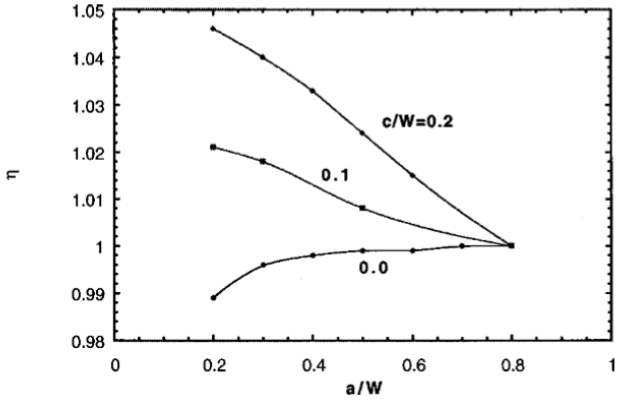


Figure 2.3: Correction factor for mode II intensity factor [22].

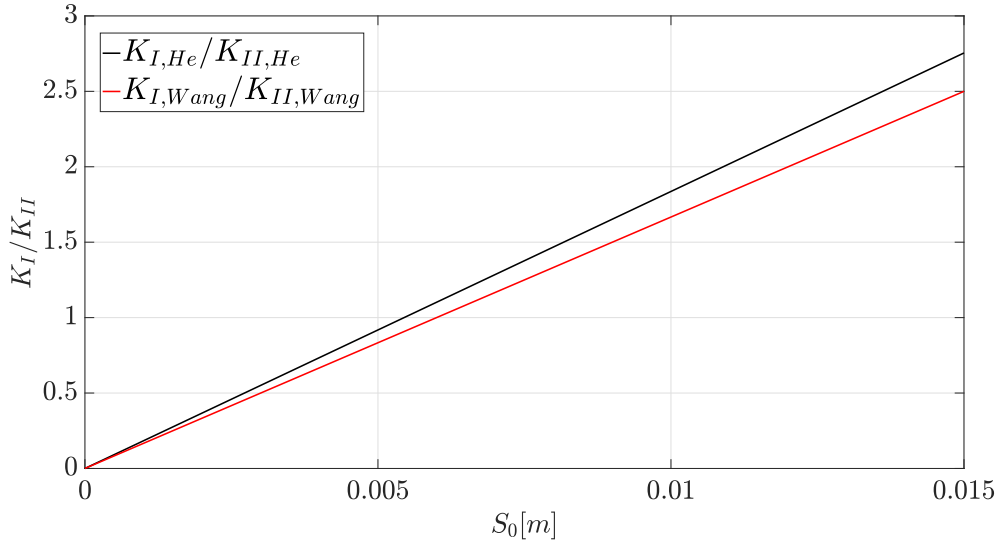


Figure 2.4: Adimensional SIFs *vs* load distance from crack plane

In figures 2.4 and 2.5 it is shown the relation of the adimensional SIF $\left(\frac{K_I}{K_{II}}\right)$ as well as β (atan$\left(\frac{K_I}{K_{II}}\right)$) with the load distance to the pre-crack plane (S_0) for $s_1 = 85$ mm,$s_2 = 15$ mm, $P = 36000$ N, $a = 14$ mm, $W = 35$ mm, $t = 20$ mm,

To measure the pure mode I stress intensity factor K_I the symmetric configuration, figure 2.6, is used since it causes the sole existence of a bending moment at the crack tip, and can be written as [21],

$$K_I = \frac{M\sqrt{\pi a}}{W^2 t} Y_I \tag{2.8}$$

where $M = \frac{(S_2 - S_1)}{2} P$ is the bending moment at the crack tip.

The author of [23] made some interesting remarks regarding the stress intensity factor K_{II} for pure mode II ($S_0 = 0$ and $d = S_1$) that should be highlighted,

- K_I presents negative values for low $\frac{d}{W}$ ratios (< 0.2) which suggests that when the load is applied too close to the plane the crack faces compress against each other.

This is not desirable because the influence of friction induced between the crack faces should be taken into account.

- K_I is positive for $\frac{d}{W} \geq 0.2$.
- K_I vanishes for $\frac{d}{W} > 1.5$.
- for $\frac{d}{W} < 0.3$, K_{II} increases for larger cracks $\frac{a}{W}$ and decrases for shorter ones.
- For $\frac{d}{W} > 0.5$, K_{II} generally decreases for all crack lenghts while only for extremelly short ones $\frac{a}{W} < 0.2$ it remains constant, this shows that the point at which the load is applied must be carefully choosen being that the further the load is placed from the crack plane the lower will K_{II} value be.
- In order to not nullify K_I, $\frac{d}{W}$ should be less than 1.
- For pure mode II loading $\frac{d}{W}$ should be at least bigger than 1, but for safety sake, $\frac{d}{W} \geq 1.5$.

The asymmetrical four point bending set up can also take the set up shown in 2.7, where the load is always applied in the crack plane. Pure mode II loading is induced by using an anti-symmetric loading of the specimen ($L_1 = L_4$ and $L_2 = L_3$), whereas pure mode I loading can be achieved by a symmetric configuration of the supports relative to the crack plane ($L_1 = L_2$ and $L_3 = L_4$ with $L_3 > L_1$). Mode mixcity can be induced for any other options of the locations of bottom or top supports.

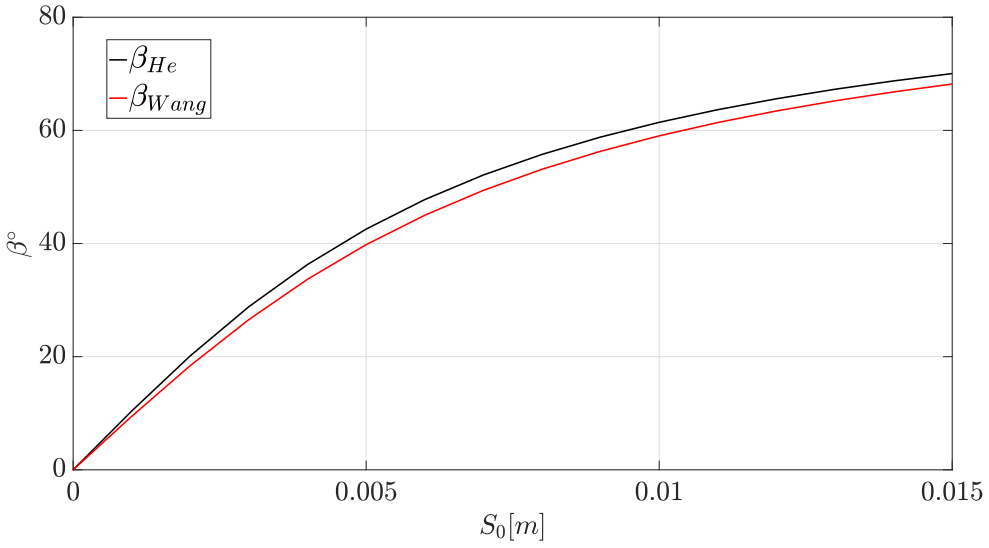


Figure 2.5: β *vs* load distance from crack plane

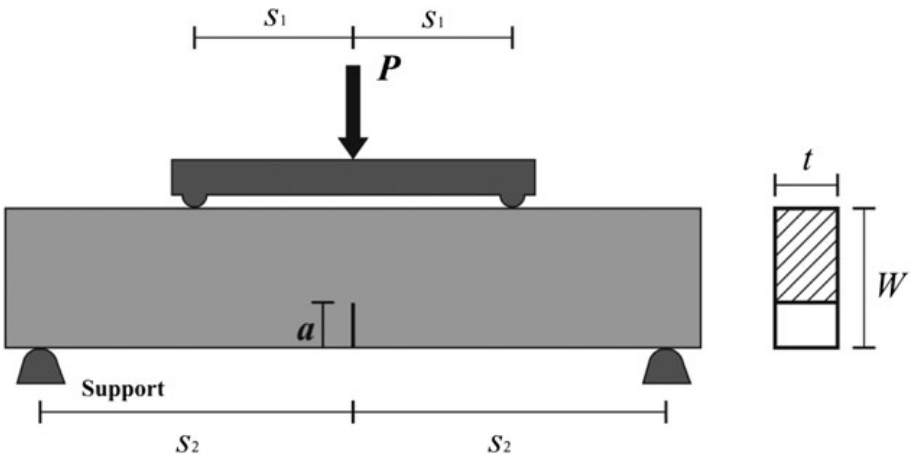


Figure 2.6: Four-point bend specimen under symmetric loading (pure mode I fracture) [21].

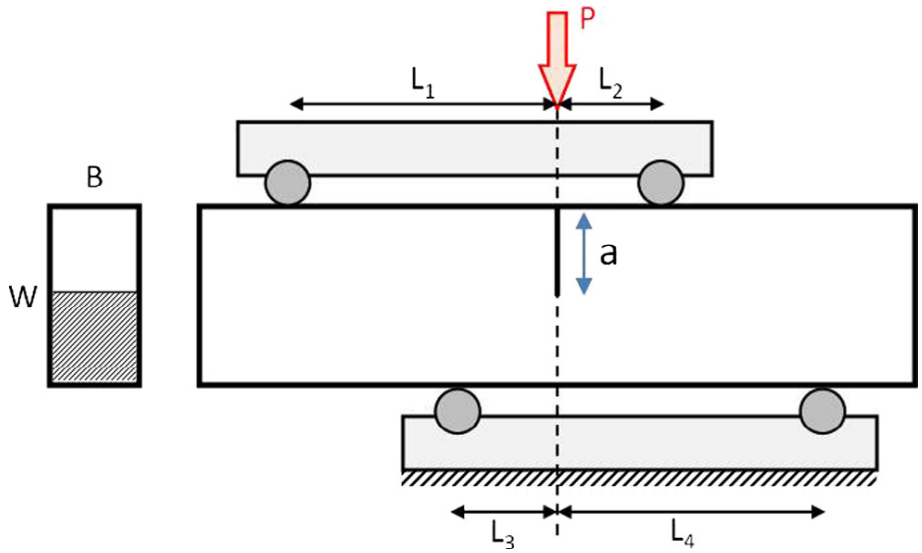


Figure 2.7: Four-point bend specimen under asymmetric loading (load in crack plane ($B = t$)) [24].

Chapter 3

Tested Material AA 6082-T6

In the following chapter the mechanical properties of the material used in this study will be presented. All specimens tested were made from the aluminum alloy 6082-T6.

3.1 Material properties - AA 6082-T6

3.1.1 Mechanical properties

The material in question has already been used by several students and researchers at FEUP so according to [25–27], its mechanical properties are presented in table 3.1,

Table 3.1: Mechanical properties of the aluminium alloy 6082-T6.

Al 6082-T6	
Young modulus [E] /GPa	69
Yield strength [σ_{Yield}] /MPa	>260
Ultimate strength [σ_U] /MPa	310
Poisson ratio	0.33

3.1.2 Fatigue properties

The fatigue properties of this aluminum alloy are hard to find, and are not exactly equal among all the sources, so several values will be presented.

The BS 7910:2005 document [28] states that the fatigue crack growth threshold for aluminium alloys in non aggressive environments is 0.7 MPa $mm^{0.5}$. It is known that the $K_{threshold}$ tends to increase with the decrease of the load ratio R ($\frac{\sigma_{min}}{\sigma_{max}}$) [29] [28] [30], so for an R=0.1 which is the load ratio used in this study, BS 7910:2005 presents the equation,

$$\Delta K_{threshold} = 170 - 214R \qquad \text{for } 0 \leq R < 0.5 \tag{3.1}$$

resulting in,

$$\Delta K_{threshold} = 148.6 \text{Nmm}^{-1.5} \approx 4.7 \quad \text{MPa}\sqrt{\text{m}} \tag{3.2}$$

This value is very conservative since this is a British standard for assessing the acceptability of flaws in metallic structures.

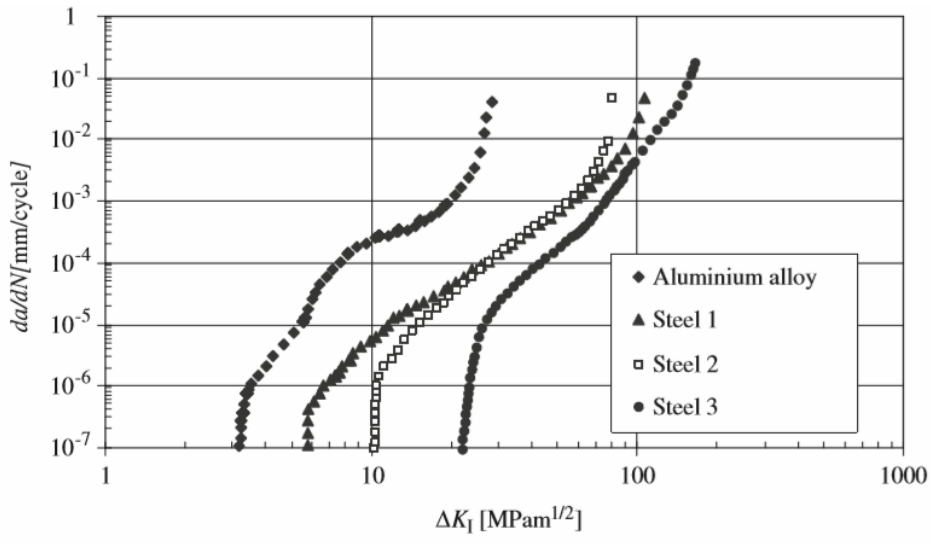


Figure 3.1: Crack growth curves of various materials for R=0.1, [12].

The book [12] of H. A. Richard and M. Sander also presents the crack growth curves of various materials for R=0.1, displayed in figure 3.1, and it can be seen that ΔK_{th} is around 3 MPa mm$^{0.5}$ for aluminium alloys, which is very broad.

According to [31] the values of the fracture toughness stress intensity factor (K_c) and threshold stress intensity factor (K_{th}) for the aluminium alloy 6082-T6 are the following,

$$K_c \approx 1295.7 \qquad \text{MPa}\sqrt{\text{mm}} \tag{3.3}$$

$$K_{th} \approx 136 \qquad \text{MPa}\sqrt{\text{mm}} \tag{3.4}$$

or

$$K_c \approx 41 \qquad \text{MPa}\sqrt{\text{m}} \tag{3.5}$$

$$K_{th} \approx 4.3 \qquad \text{MPa}\sqrt{\text{m}} \tag{3.6}$$

However, a more recent study [30] determined the threshold values for the SIF with an R=0.1 for the 6082-T6 aluminium for CT specimens with a V notch, being,

$$K_{th} = 246.64 \quad \text{Nmm}^{-1.5} \approx 7.8 \quad \text{MPa}\sqrt{\text{m}} \tag{3.7}$$

Finally according to the NASGRO database [32] the material curve for this material at a loading ratio is given in figure 3.2

Where according to the documentation [32] the stress intensity factor range ΔK_{th} can be approximated by the empirical equations,

$$\Delta K_{th} = \Delta K_1^* \Big[\frac{1-R}{1-f[R]}\Big]^{(1+RC_{th}^p)} / (1-A_0)^{(1-R)C_{th}^p} \qquad \text{for } R \geq 0 \tag{3.8}$$

in which,

$$\Delta K_1^* = \Delta K_1 \Big[\frac{a}{a+a_0}\Big]^{0.5} \tag{3.9}$$

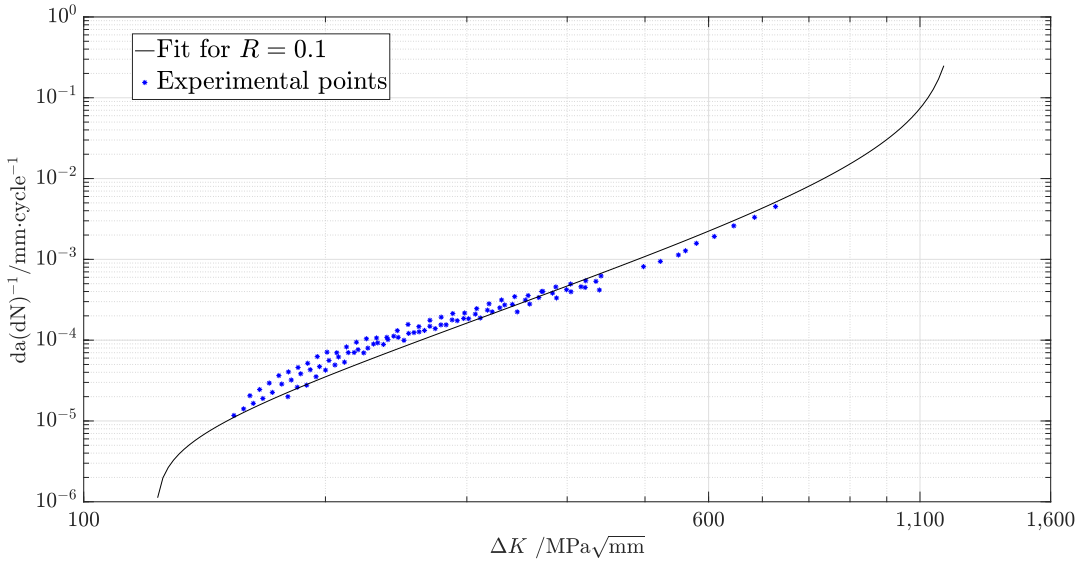


Figure 3.2: NASGRO material fitting curve for R=0.1, [32].

where R is the load ratio, A_0 is a constant used in the Newman closure function (f), a is the crack length and a_0 is a small crack parameter that is typically of the order of 0.0015 inches (0.0381 mm). The threshold stress intensity factor range as $R \longrightarrow 1.0$ is represented by ΔK_1 and C_{th} is an empirical fit constant.

$$f = \max(R, A_0 + A_1 R + A_2 R^2 + A_3 R^3) \qquad \text{for } R \geq 0 \tag{3.10}$$

where the coefficients A_0, A_1, A_2 and A_3 are given by,

$$A_0 = (0.825 - 0.34\alpha + 0.05\alpha^2)\left[\cos\left(\frac{\pi}{2} S_{max}/\sigma_0\right)\right]^{\frac{1}{\alpha}} \tag{3.11}$$

$$A_1 = (0.415 - 0.071\alpha) S_{max}/\sigma_0 \tag{3.12}$$

$$A_2 = 1 - A_0 - A_1 - A_3 \tag{3.13}$$

$$A_3 = 2A_0 + A_1 - 1 \tag{3.14}$$

where α is a plane stress/strain constraint factor and S_{max}/σ_0 the ratio of the maximum applied stress to the flow stress.

In figure 3.3 is represented the material fitting curve for this aluminium alloy for three different load ratios. From here the values of C_{th}, ΔK_1, S_{max}/σ_0 and α can be obtained.

The value obtained for the stress intensity factor range threshold according to equation 3.8 was $\Delta K_{th} = 113.34$ MPa mm$^{0.5}$=3.58 MPa m$^{0.5}$ which falls in line with figure 3.3.

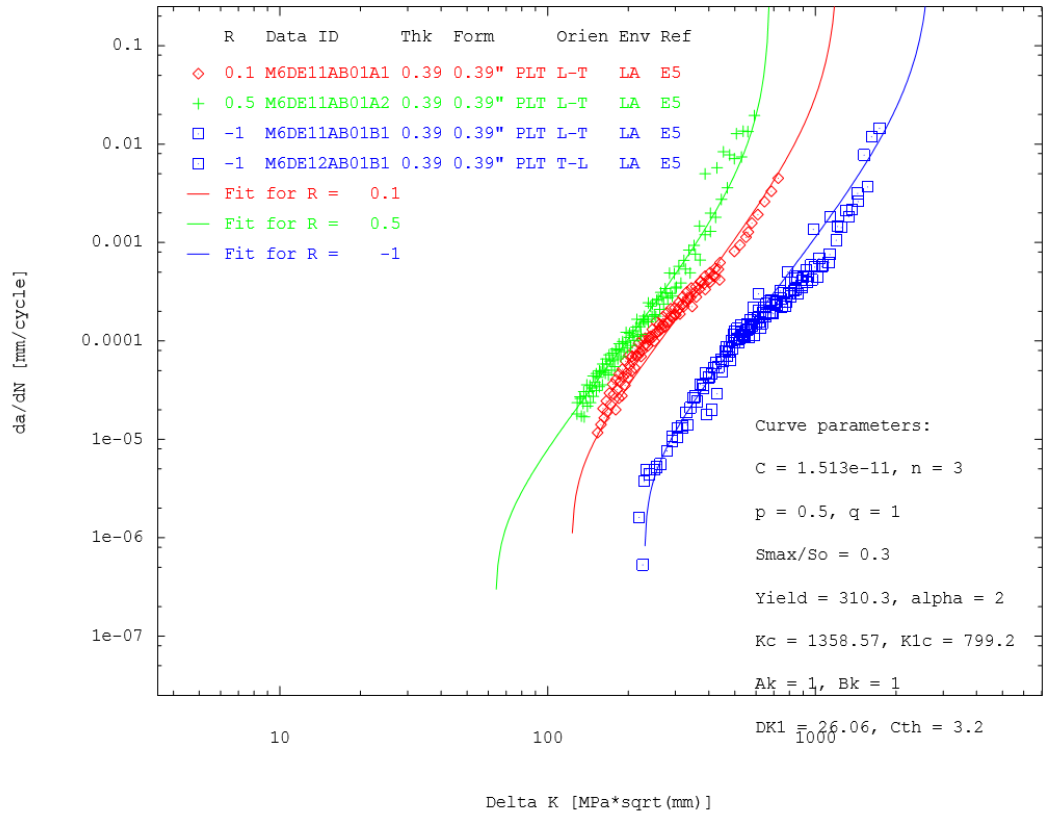


Figure 3.3: NASGRO material fitting curve for R=-1, R=0.1, R=0.5, [32].

Chapter 4

Preliminary studies

4.1 Case study 1 - Mode I crack growth in infinite plate

In this study case a comparation between the know analytical solution and the results returned by ABAQUS will be made, for the displacements of an infinite cracked plate (of unit thickness) with a central transverse crack of length $2a$ under mode I loading. The stress intensity factor (K_I) will also be obtained by the VCCT and J Integral methods and compared to the ABAQUS solution for diferent crack sizes. All the models used for this case study can be found in annex A.

4.1.1 Analytical solution for crack displacements

According to [6] the displacement field for an infinite ($W \gg 2a$) cracked plate with central transverse crack can be given by,

$$\upsilon = \frac{2\sigma}{E}\sqrt{a^2 - x^2} \qquad \text{(plane stress)} \tag{4.1}$$

The studied case is presented in figure 4.1.

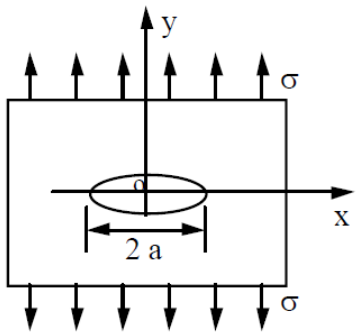


Figure 4.1: Cracked in infinite body under tensile stress, [17].

The plate is under stress at the top and bottom as indicated on 4.2 and the crack size is 10 times smaller than the plate dimensions ($\frac{a}{w} \leq 0.1$).

Diferent models were created that differ in the number and type of finite elements (CPS4R, CPS4, CPS8R) used, in order to assess the influence of finer meshes in the stress intensity factors obtained via ABAQUS.

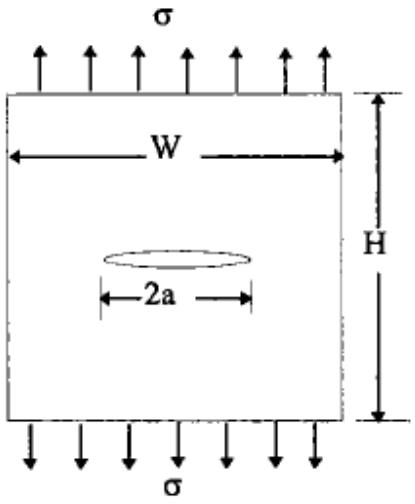


Figure 4.2: Plate model for the currrent case study (W=H), [33].

4.1.2 Analytical solution for crack mode I stress intensity factor along an infinite cracked plate with central transverse crack

The stress intensity factor for a infinite plate can be obtained by,

$$K_0 = \sigma\sqrt{\pi a} \tag{4.2}$$

where,

$$K_I = K_0\Big(\sqrt{\frac{1}{\cos(\pi a 2w)}}(1-0.025)\Big(\frac{a}{w}\Big)^2 + 0.06\Big(\frac{a}{w}\Big)^4\Big) \tag{4.3}$$

For a finite plate the analytical solution to the mode I SIF, according to [34], can be given by,

$$\begin{aligned} K_I =& \sigma\sqrt{\pi a}\Big[1 + 0.043\Big(\frac{a}{w}\Big) + 0.491\Big(\frac{a}{w}\Big)^2 + 7.125\Big(\frac{a}{w}\Big)^3 - 28.403\Big(\frac{a}{w}\Big)^4 + 59.583\Big(\frac{a}{w}\Big)^5 \\ & - 65.278\Big(\frac{a}{w}\Big)^6 + 29.762\Big(\frac{a}{w}\Big)^7\Big] \end{aligned} \tag{4.4}$$

being $w = \frac{W}{2}$.

4.1.3 ABAQUS modeling

The plate is quadrangular with a width of 20 mm and a crack ($2a$) with $a = 1$mm, under a tensile stress of 100 MPa.

The chosen material was aluminum with an elasticity modulus (E) of 70000 MPa and a Poisson coefficient (ν) of 0.3.

Due to symmetry, the plate was was modeled with just one quarter, where the boundry conditions applied can be seen in figure 4.3.

One can also tell, by figure 4.3, the plate is divided in three main areas were the seed size varies, allowing the obteintion of a finer mesh near the crack and a coarser mesh as we distance ourselfs from the region of interest. For mesh number 1 it is worth pointing out that the nodal displacements along the crack were obtained with and without reduced integration for comparison sake.

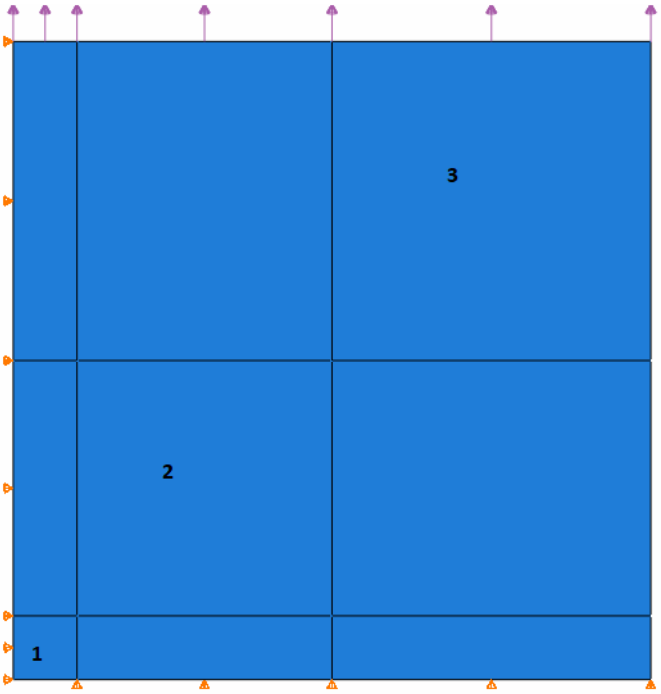


Figure 4.3: Cracked in infinite body under tensile stress

Table 4.1: Meshes used for case study 1

	Seed size		
Mesh	**Zone 1**	**Zone 2**	**Zone 3**
1	0.08	0.08	0.2
2	0.05	0.05	0.2
3	0.025	0.025	0.2

4.1.4 Results: Crack nodal displacements

In 4.4 the representation of the displacements along the crack for different meshes is presented.

It can be seen that the nodal displacements obtained with ABAQUS match the analytical equation 4.1 with high accuracy. It can also be observed that models with finer mesh and 8 node quadrangular elements (CPS8R) lead to more accurate predictions than their counterparts (CPS4).

Comparing figures 4.5 and 4.6 one can say that the nodal displacements at the crack look less distorted for 4 node quadrangular elements without reduced integration (CPS4).

Below in figure 4.7 it is seen that the use of CPS8R elements describe curve shapes better than CPS4 elements, resulting in this case in a crack with an elliptical shape, as expected.

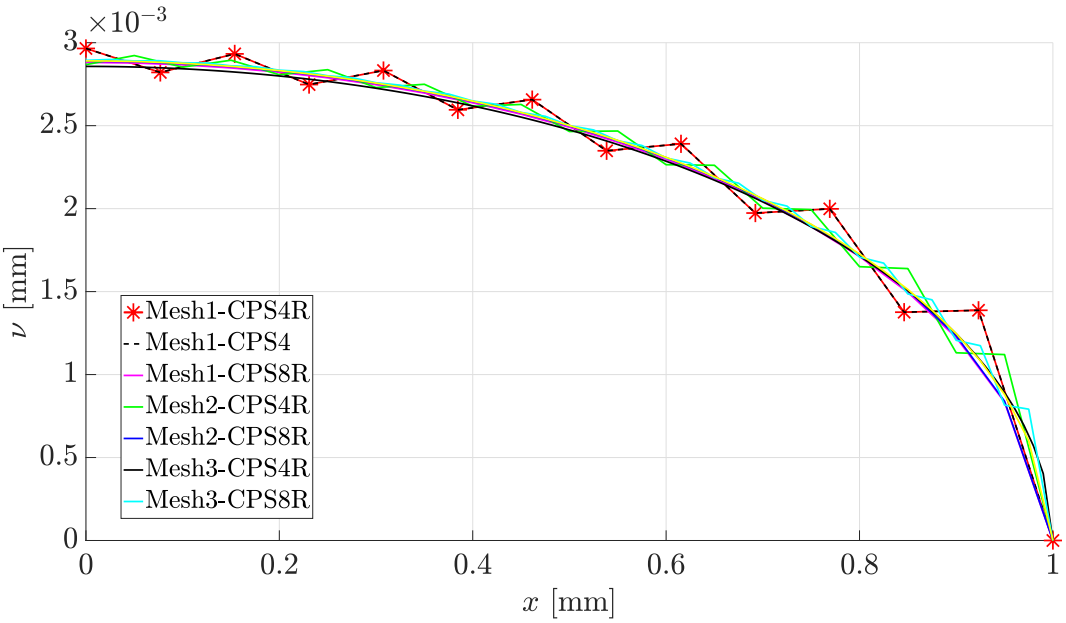


Figure 4.4: Displacements along the crack plane

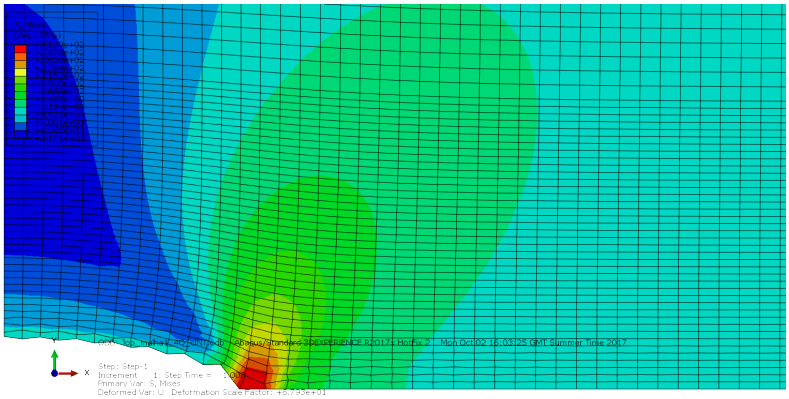


Figure 4.5: Mesh 1 crack using CPS4R elements

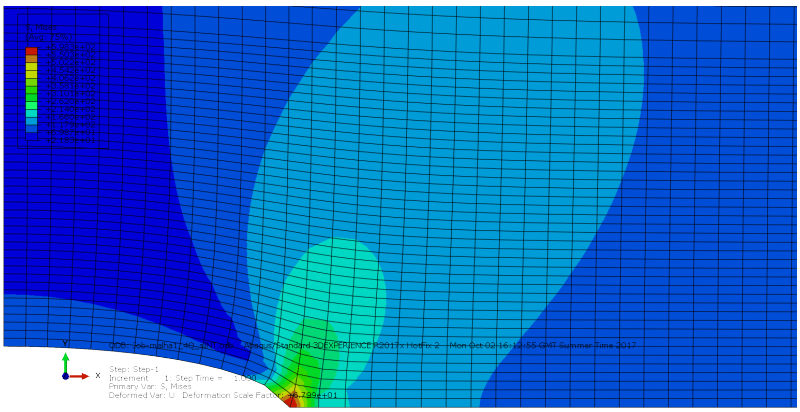


Figure 4.6: Mesh 1 crack using CPS4 elements

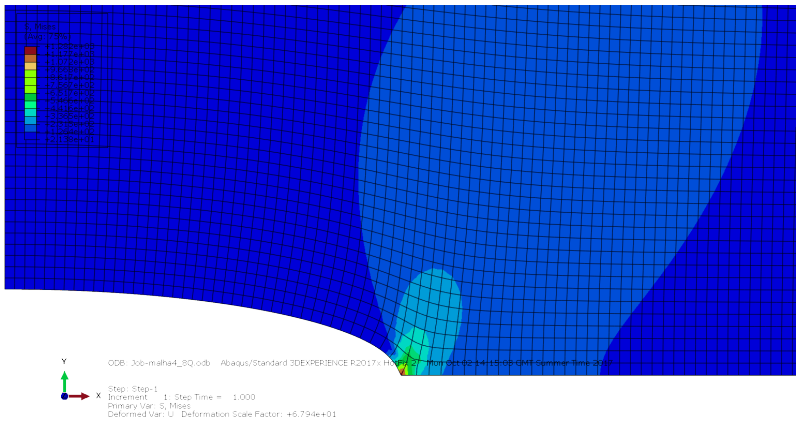


Figure 4.7: Mesh 3 crack using CPS8R elements

4.1.5 Results: Crack mode I stress intensity factor for infinite plate

Table 4.2 presents the results of the mode I SIF for each mesh in the infite plate situation ($\frac{a}{W} \leq 0.1$).

Table 4.2: Mode I SIF for infinite plate using diferent elements/meshes

K_I [**MPa mm**$^{0.5}$]			
a=1 mm; w=1 mm σ=100 MPa	**Analytical solution**	**VCCT**	**J integral**
M1-Q4	178.3	177.9	179.7
M1-Q8	178.3	177.6	179.6
M2-Q4	178.3	179.7	179.7
M2-Q8	178.3	179.4	179.6
M3-Q4	178.3	179.7	179.6
M3-Q8	178.3	179.5	179.7

From this table it can be stated that either the VCCT and J integral method lead to accurate predictions about the stress field at the crack tip, caracterized by the stress intensity factor.

4.1.6 Results: Crack mode I stress intensity factor for finite plate

To finalize this case study the mode I SIF was determined for two additional instances, the growth of the inicial crack ($a = 1$ mm) to $a = 2$ mm and $a = 3$ mm. The finer mesh, mesh 3, was chosen for this situation. It should be noted that the SIF analytical prediction for situations $a = 2$ mm and $a = 3$ mm was made using equation 4.4 since equation 4.3 its only valid for $\frac{a}{W} \leq 0.1$.

Once again, through table 4.5, it can be said that both the VCCT and J integral methods deliver very accurate results when compared to the analytical predictions. On a final note the mode I SIF increases with crack size, as expected.

Table 4.3: Difference between VCCT and J integral methods with analytical solution-infinite plate

Difference[%]		
	VCCT	**J integral**
M1-Q4	0.23	0.78
M1-Q8	0.39	0.73
M2-Q4	0.78	0.78
M2-Q8	0.62	0.73
M3-Q4	0.78	0.73
M3-Q8	0.67	0.78

Table 4.4: Mode I SIF for crack increment on finite plate

K_I [**MPa mm**$^{0.5}$]			
	Analytical solution	**VCCT**	**J integral**
M3-Q4 (a=1)	178.3	179.7	179.6
M3-Q4 (a=2)	264.5	264.5	264.2
M3-Q4 (a=3)	344.8	344.8	344.7
M3-Q8 (a=1)	178.3	179.5	179.7
M3-Q8 (a=2)	264.5	264.4	264.5
M3-Q8 (a=3)	344.8	344.6	344.7

Table 4.5: Difference between VCCT and J integral methods with analytical solution - finite plate

Difference[%]		
	VCCT	**J integral**
M3-Q4 (a=1)	0.78	0.73
M3-Q4 (a=2)	0	0.11
M3-Q4 (a=3)	0	0.03
M3-Q8 (a=1)	0.67	0.78
M3-Q8 (a=2)	0.04	0
M3-Q8 (a=3)	0.05	0.03

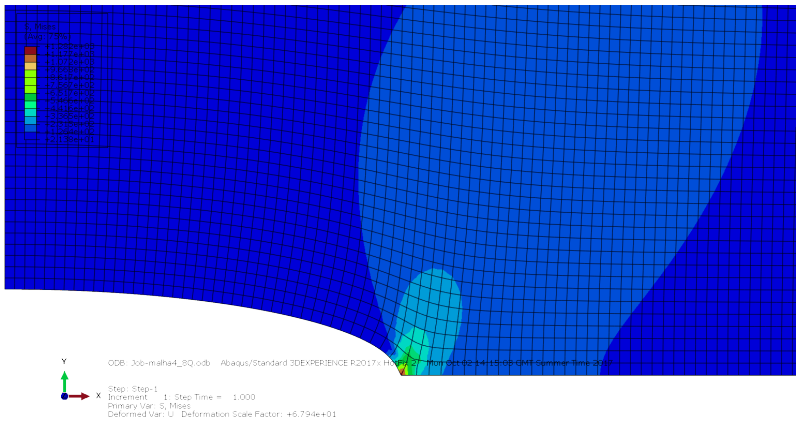


Figure 4.8: Mesh 3 crack using CPS8R elements $a = 1$ mm

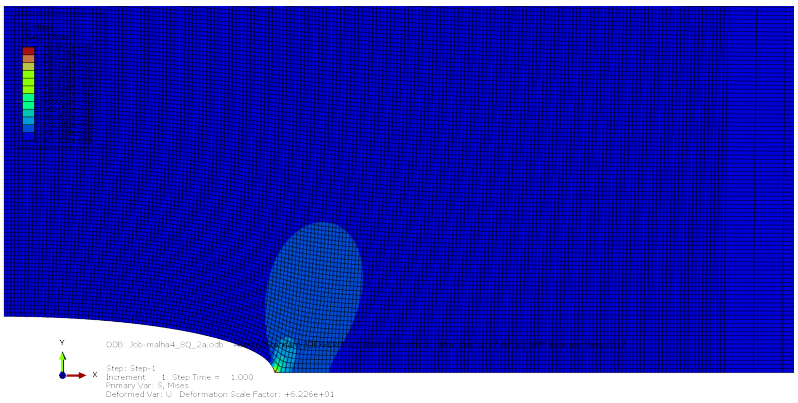


Figure 4.9: Mesh 3 crack using CPS8R elements $a = 2$ mm

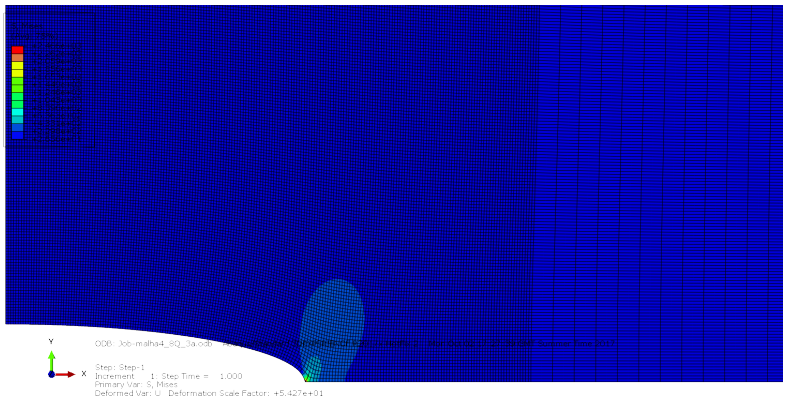


Figure 4.10: Mesh 3 crack using CPS8R elements $a = 3$ mm

4.2 Case study 2: Inclined crack - crack growth path and mixed mode SIFs

This case study can be divided in two sections; On the first the goal is to model the inclined crack situation for various angles using ABAQUS and obtain the SIFs through VCCT, MTS and MERR methods. On the second part the original crack will be incremented and

the propagation angle will be determined analytically and through ABAQUS simulation. All the models used for this case study can be found in annex B.

4.2.1 SIF determination in plate with inclined crack

In figure 4.11 it is presented a infinite plate ($\frac{a}{W} \leq 0.1$) under traction which contains an inclined crack of length $2a$ and an angle β relative to the applied load.

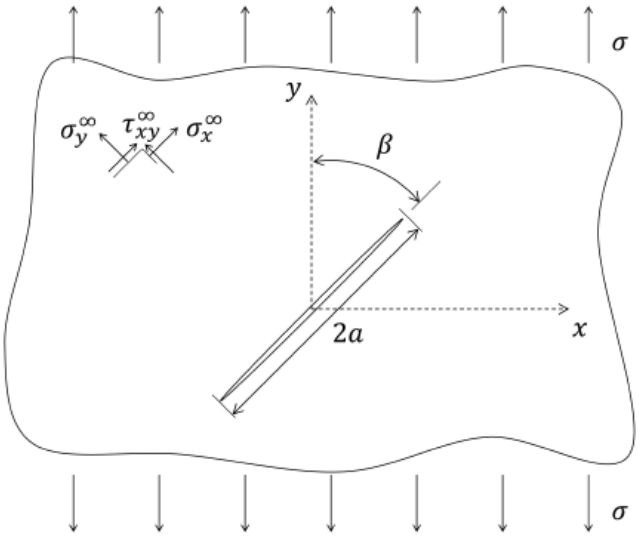


Figure 4.11: Infinite plate under tensile stress with an inclined crack, [33].

The study case in question is further caracterized in figure 4.12, along with table 4.6 containing its dimensions as well as the material mechanical properties.

Table 4.6: Dimensions and material properties for study case 2

a	0.5 [mm]
W	10 [mm]
E	70000 [MPa]
υ	0.3
σ	200[MPa]

A set of angles was picked to study the different mode contributions, and they were, $\beta = 0°$, $\beta = 15°$, $\beta = 30°$, $\beta = 45°$, $\beta = 60°$, $\beta = 75°$, $\beta = 90°$.

4.2.2 Analytical soltion for the mixed mode SIFs in a plate with a inclined crack

Since $\frac{a}{W} = 0.05$ the plate can be considerate infinite, and according to [17] the SIF for mode I and mode II loading can be given by, respectivly,

$$K_I = K_0 \cos(\alpha)^2 \tag{4.5}$$

$$K_{II} = K_0 \sin(\alpha) \cos(\alpha) \tag{4.6}$$

where,

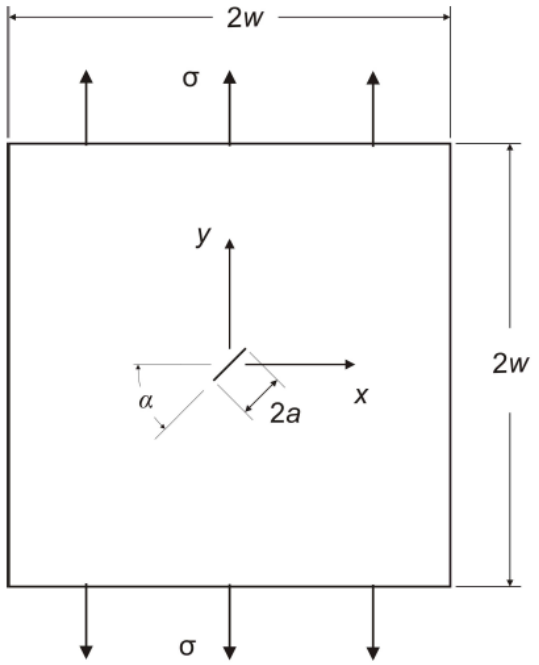


Figure 4.12: Infinite plate under tensile stress with an inclined crack used in case study 2, [35].

$$K_0 = \sigma\sqrt{\pi a} \tag{4.7}$$

and,

$$\alpha = 90^\circ - \beta \tag{4.8}$$

The SIFs can also be written in a dimensionless form,

$$\frac{K_I}{K_0} = \frac{K_0 \cos(\alpha)^2}{K_0} = \cos(\alpha)^2 \tag{4.9}$$

$$\frac{K_{II}}{K_0} = \frac{K_0 \sin(\alpha)\cos(\alpha)}{K_0} = \sin(\alpha)\cos(\alpha) \tag{4.10}$$

4.2.3 ABAQUS modeling

The plate was created in total and a quadrangular partition was created around the crack, allowing a finer control of the mesh around it, enabling accurate stress intensity factor predictions using the VCCT and J integral techniques. Four node quadrangular elements with reduced integration (CPS4R) were used along two zones, zone A (seed size=0.1) and zone B (seed size=0.5), shown in figure 4.13. For the J integral calculation the number of contours chosen was 10 since it showed good convergency towards the mode I and mode II SIFs (K_I and K_{II}).

In case study 1, to use the VCCT it was only required to ask ABAQUS for the reactions at the supports. In this case however, that is no longer possible, so to determine the nodal forces of the node located at the crack tip a free body cut at the crack tip element was created and the reactions at the nodes using the NFORC output were obtained (figure 4.14).

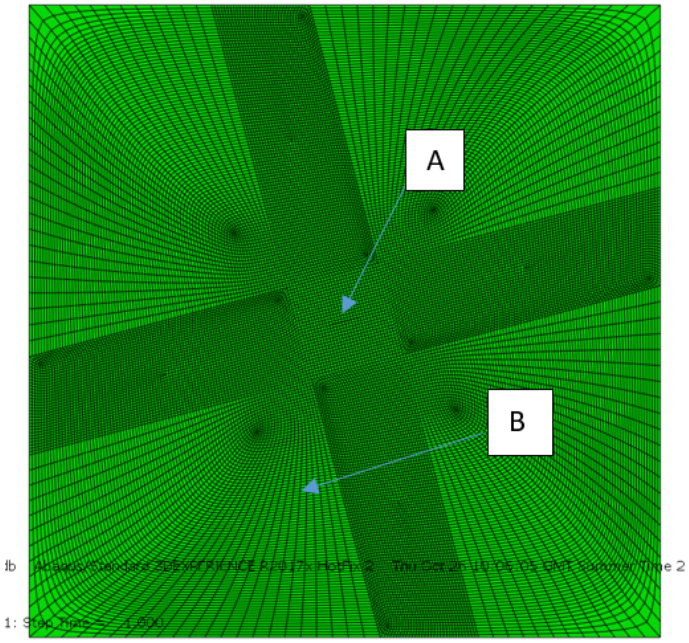


Figure 4.13: Infinite plate with inclined crack $\alpha = 15°$

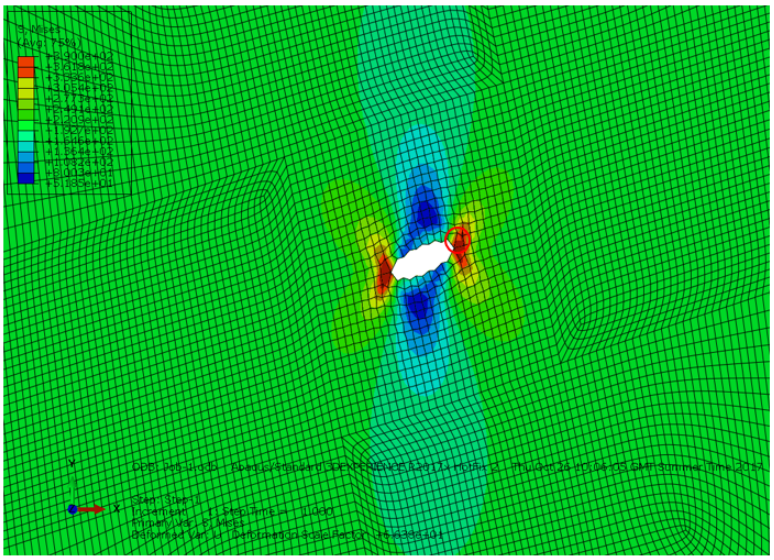


Figure 4.14: Infinite plate with inclined crack $\alpha = 15°$

4.2.4 Results: SIFs for inclined crack in infinite plate

In table 4.7 the results for the SIFs through the analytical solutions using equations 4.5 and 4.6 are presented, alongside with the SIFs obtained via ABAQUS by the MERR, MTS and VCCT criteria. In figures 4.15, 4.16, 4.17, 4.18, 4.19 show the obtained crack for each case ($\Delta a = 0$, $\Delta a = 0.5$ and $\Delta a = 1.5$, respectivly).

A second table, 4.8, was created with the errors (differences) relative to the analytical solution, following the equation,

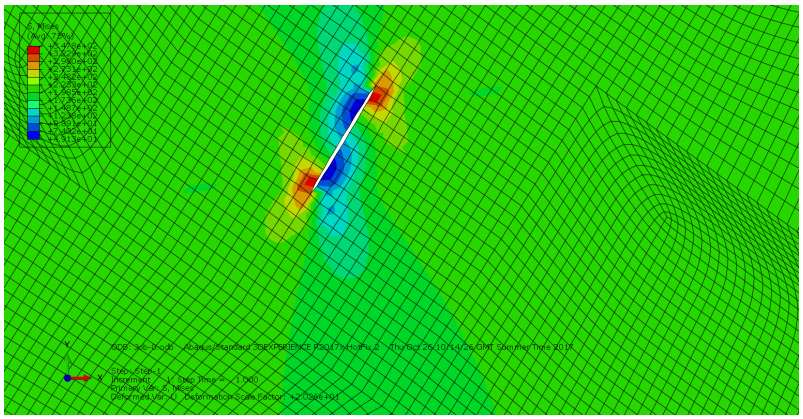


Figure 4.15: Plate with inclined crack $\alpha = 60°$, $\Delta a = 0$

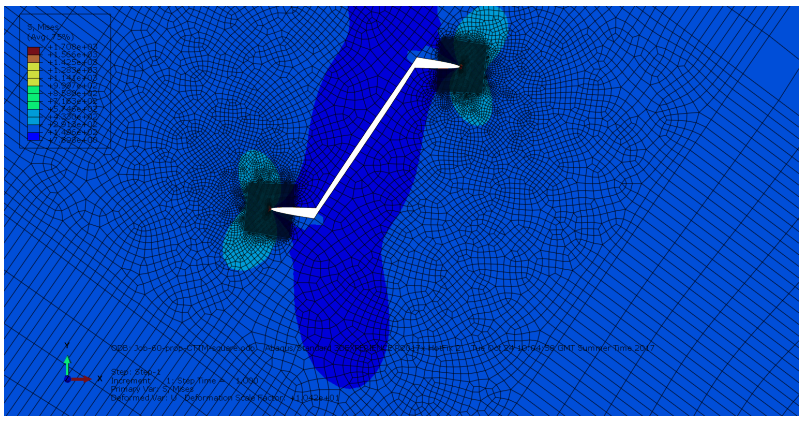


Figure 4.16: Plate with inclined crack $\alpha = 60°$, $\Delta a = 0.5$ using MTS criteria

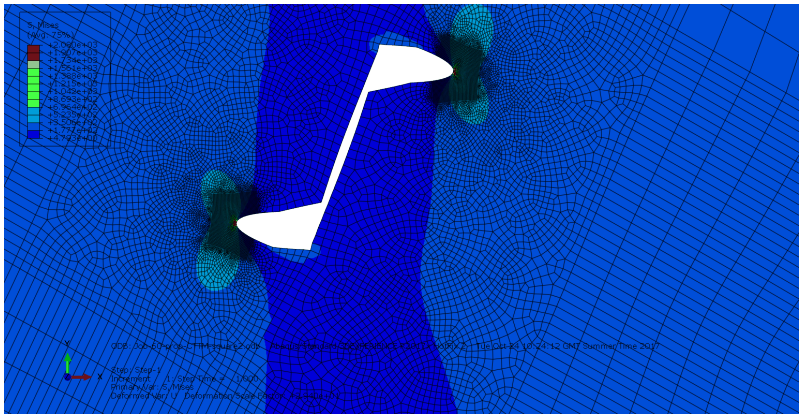


Figure 4.17: Plate with inclined crack $\alpha = 60°$, $\Delta a = 1$ using MTS criteria

$$\text{Relative error}(\%) = \left| \frac{K_{analyticalsolution} - K_{MERR,CTTM,VCCT}}{K_{analyticalsolution}} \right| * 100 \tag{4.11}$$

No values were calculated for $K_{II}(\alpha = 0°)$, $K_I(\alpha = 90°)$,$K_{II}(\alpha = 90°)$ since there solution is null.

Using equations 4.9 and 4.10 two graphs were built for better visualization of the

Table 4.7: K_I,K_{II} for different inclined cracks

	Analytical Solution		**MERR**		**MTS**		**VCCT**	
α	K_I	K_{II}	K_I	K_{II}	K_I	K_{II}	K_I	K_{II}
0°	250.66	0	250.31	0.22	250.31	0.22	251.42	0
15°	233.87	62.67	233.54	62.62	233.54	62.62	234.44	62.76
30°	188.14	108.5	188.14	108.5	188.15	108.64	188.53	108.71
45°	125.33	125.33	125.18	125.06	125.18	125.06	125.65	125.48
60°	62.67	108.54	62.65	108.22	62.65	108.22	62.81	108.66
75°	16.79	62.67	16.89	62.76	16.89	62.76	16.83	62.72
90°	0	0	0.05	-0.99	0.05	1.11	0	0

Table 4.8: Differences obtained relative to the analytical solution

	MERR Difference		**MTS Difference**		**VCCT Difference**	
α	K_I	K_{II}	K_I	K_{II}	K_I	K_{II}
0°	0.14	-	0.14	-	0.3	-
15°	0.14	0.07	0.14	0.07	0.24	0.15
30°	0.07	0.04	0.08	0.09	0.28	0.15
45°	0.12	0.22	0.12	0.22	0.26	0.12
60°	0.02	0.29	0.02	0.29	0.23	0.11
75°	0.61	0.15	0.61	0.15	0.23	0.08
90°	-	-	-	-	-	-

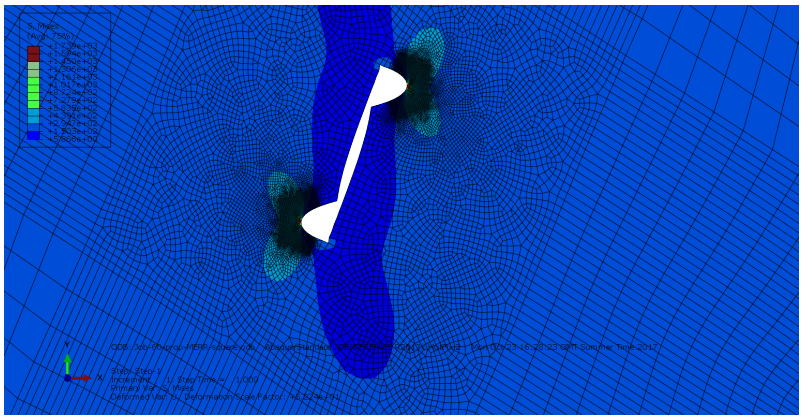


Figure 4.18: Plate with inclined crack $\alpha = 60°$, $\Delta a = 0.5$ using MERR criteria

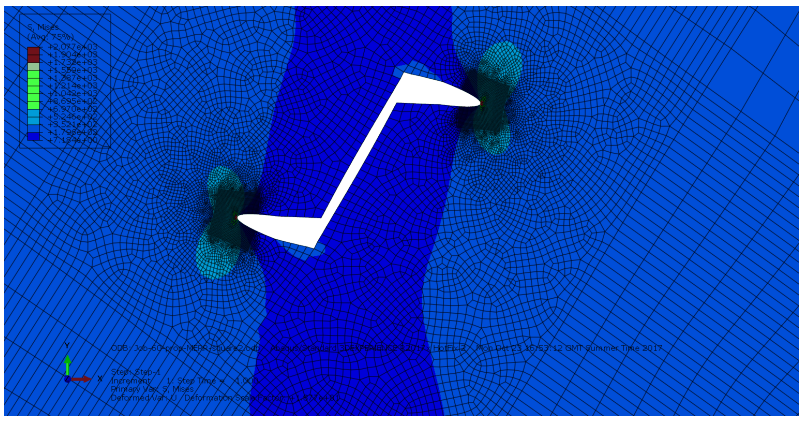


Figure 4.19: Plate with inclined crack $\alpha = 60°$, $\Delta a = 1$ using MTS criteria

variation of $\frac{K_I}{K_0}$ and $\frac{K_{II}}{K_0}$ for different angles(α).

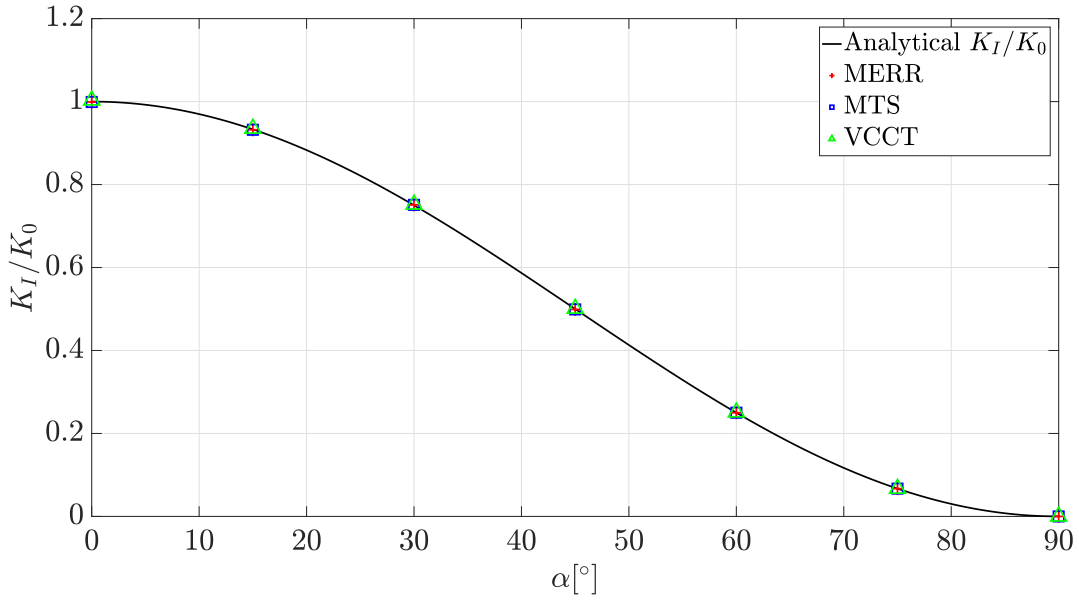


Figure 4.20: Analytical mode I SIF *vs* SIFs obtained via ABAQUS

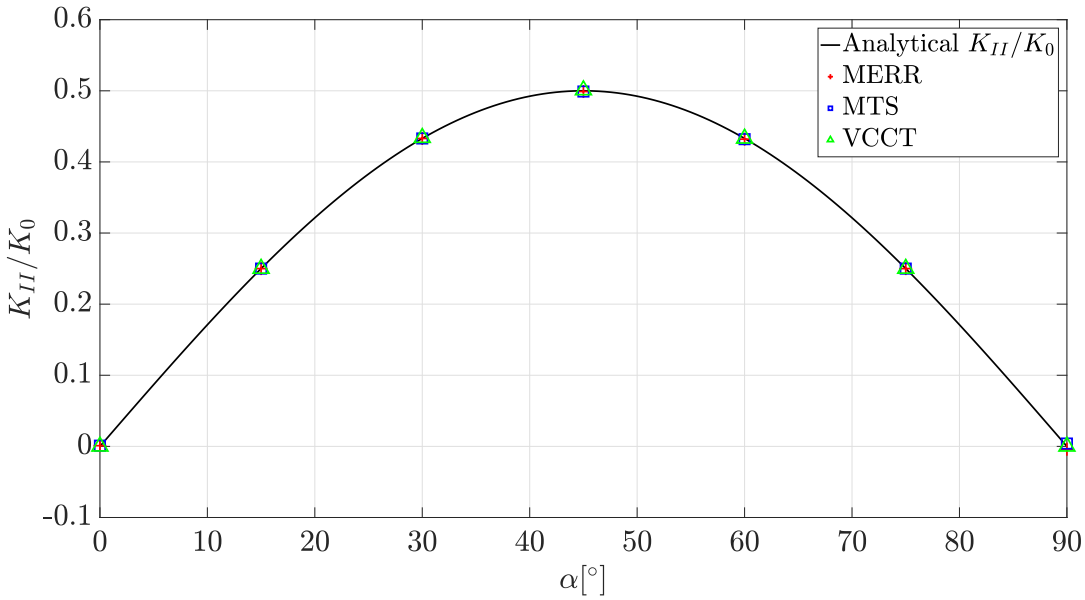


Figure 4.21: Analytical mode II SIF *vs* SIFs obtained via ABAQUS

It can be stated that the values obtained by finite element analysis are in excellent agreement with the analytical predictions.

4.2.5 Determination of crack growth direction and SIFs in mixed mode loading through the MERR and MTS criteria

For the inclined crack situation, the crack growth direction (ψ_0) will be slightly different when using the MTS and MERR criteria.

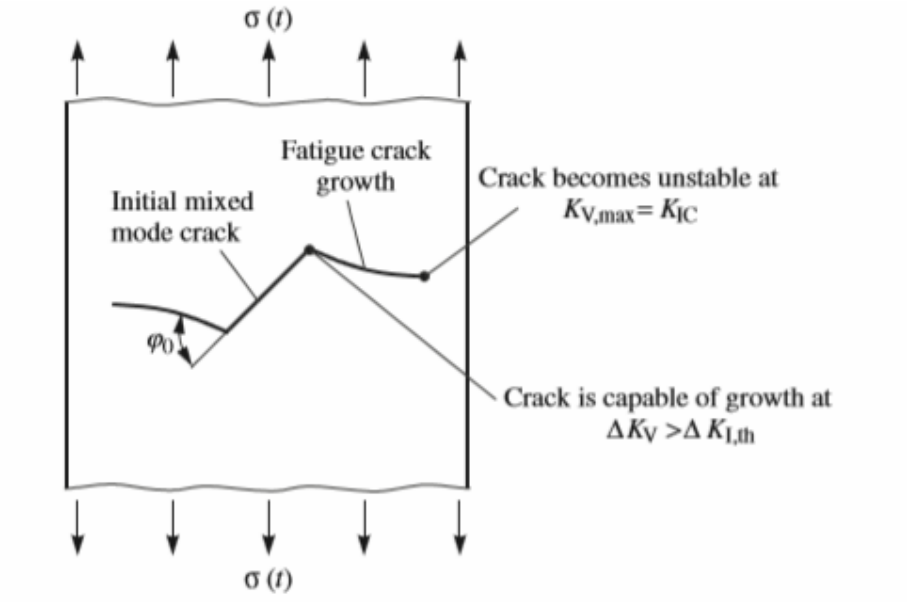


Figure 4.22: Plate under tensile load with inclined crack ($\Delta K_v = \Delta K_e$), [12].

In this section the goal is to obtain the crack growth direction and SIFs using the

MERR and MTS criteria, returned by ABAQUS, for the growth of a crack with length a to $a + \delta a$.

Initially the crack will have $2a = 2$ mm and will be tilted $\alpha = 60°$. After determining the propagation direction of the crack tip, it will be incresead to $2a = 2.5$ mm and $2a = 3$ mm. The plate is a square with $W = 10$ mm and is under a tensile strength of $\sigma = 200$ MPa. The material properties stay the same as in study case 1.

4.2.6 ABAQUS modeling

Using the same method as in the first part of this case study, the model was build for a tilted crack $\alpha = 60°$ with $2a = 2$ mm. With this model the SIFs and crack propagation direction were obtained, as presented in the first line of tables 4.10 and 4.11.

Afterwards a squared partition was created at the crack tips, as shown on figure 4.23, and each tip was extended 0.5 mm in the direction ψ_0 retrieved from each criteria, presented in tables 4.10 and 4.11.

Once again, the square partition allows better control over the mesh refinement. As seen in table 4.9, there are three different zones with unique seed sizes,

Table 4.9: Mesh partitions and respective seedsize

Zone	Seed Size
A	0.01
B	0.1
C	0.5

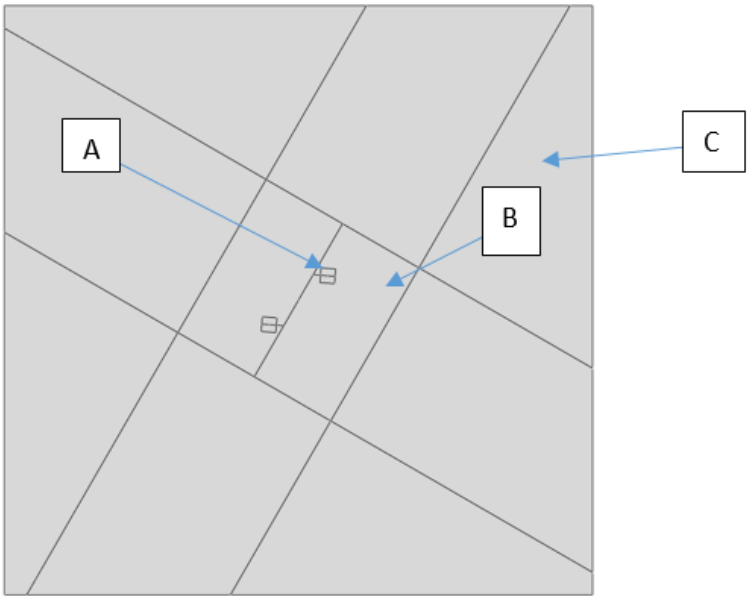


Figure 4.23: ABAQUS sketch for the first increment $\Delta a = 0.5$ mm

After the first simulation, the process described above was repeated, the crack tips were increased 0.5 mm in the direction ψ_0 retrieved from each criteria.

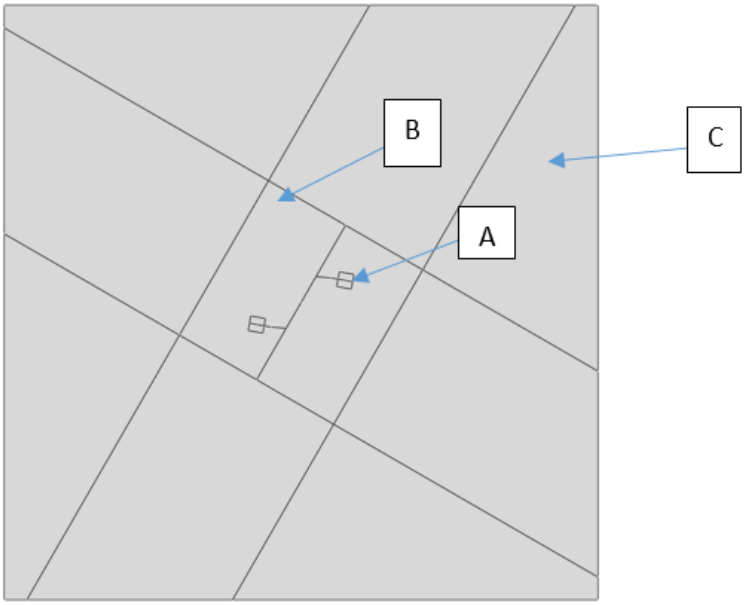


Figure 4.24: ABAQUS sketch for the second increment $\Delta a = 1$ mm

4.2.7 Results: SIFs and crack propagation direction for inclined crack in infinite plate

In tables 4.10 and 4.11 the SIFs and crack propagation directions are shown for each iteration. In order to compare the ABAQUS solution for the crack propagation angles, equations 1.30 and 1.31 will be used.

Table 4.10: SIFs for various Δa increments with $\alpha = 60°$

	MERR				
				ψ_0**(degrees)**	
	K_I	K_{II}	**MERR**	**Erdogan & Sih**	**Richard**
$\alpha = 60°$, $a = 1$, $\Delta a = 0$	89.57	154.80	-64.26	-59.98	-65.04
$\alpha = 60°$, $a = 1$, $\Delta a = 0.5$	382.40	16.83	-5.80	-5.02	-6.41
$\alpha = 60°$, $a = 1$, $\Delta a = 1$	466.20	-26.51	7.06	6.47	8.13

It can be seen that the crack propagation angle returned by ABAQUS does not differ much from the analytical equations used, as seen on tables 4.11 and 4.12.

As seen in tables 4.11 and 4.12 the crack deflection angle obtained by ABAQUS MTS criteria (ψ_0) is predicted very accuratly using Erdogan and Sih criteria, whereas the the crack deflection angle obtained by ABAQUS MERR criteria is predicted more accuratly using Richard's.

Remembering equation 1.29 and combining it with equations 1.33 and 1.34 results in,

$$\cot(\beta) = \frac{-\sin(\psi_0)}{3\cos(\psi_0) - 1} \tag{4.12}$$

This equation is represented in figure 4.25 along with the crack path directions obtained

Table 4.11: SIFs for various Δa increments with $\alpha = 60°$

	MTS				
			$\psi_0(degrees)$		
	K_I	K_{II}	**MTS**	**Erdogan & Sih**	**Richard**
$\alpha = 60°$, $a = 1$, $\Delta a = 0$	89.57	154.80	-59.98	-59.98	-65.04
$\alpha = 60°$, $a = 1$, $\Delta a = 0.5$	380.20	38.49	-11.33	-11.34	-13.59
$\alpha = 60°$, $a = 1$, $\Delta a = 1$	466.20	-32.26	7.84	7.84	9.71

Table 4.12: Differences between MTS and MERR criteria with analytical solutions

	MERR		**MTS**	
	Difference[%]			
	Erdogan & Sih	**Richard**	**Erdogan & Sih**	**Richard**
$\alpha = 60°$, $a = 1$, $\Delta a = 0$	6.66	-1.21	0.00	-8.43
$\alpha = 60°$, $a = 1$, $\Delta a = 0.5$	13.38	-10.54	-0.05	-19.95
$\alpha = 60°$, $a = 1$, $\Delta a = 1$	8.34	-15.15	0.02	-23.85

for $2a = 2$ and $\Delta a = 0$.

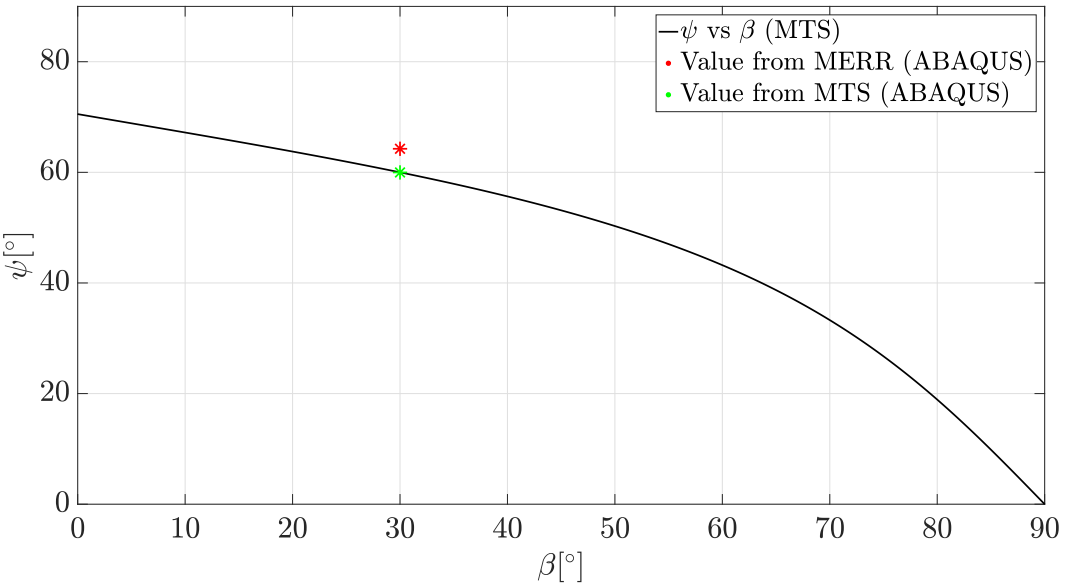


Figure 4.25: ψ_0 *vs* β relation

The value obtained by the MTS criteria has the highest accuracy as expected, due to the fact that equation 1.29 is obtained from the MTS criteria.

In figures 4.26 and 4.27 the crack paths according to each criteria were ploted,

It woulde be expected that the crack path would form a more distinct shape (kink) like in figure 4.22. Perhaps if more crack growth increments with smaller lengths were to be used the crack path would be more similar to that of figure 4.22.

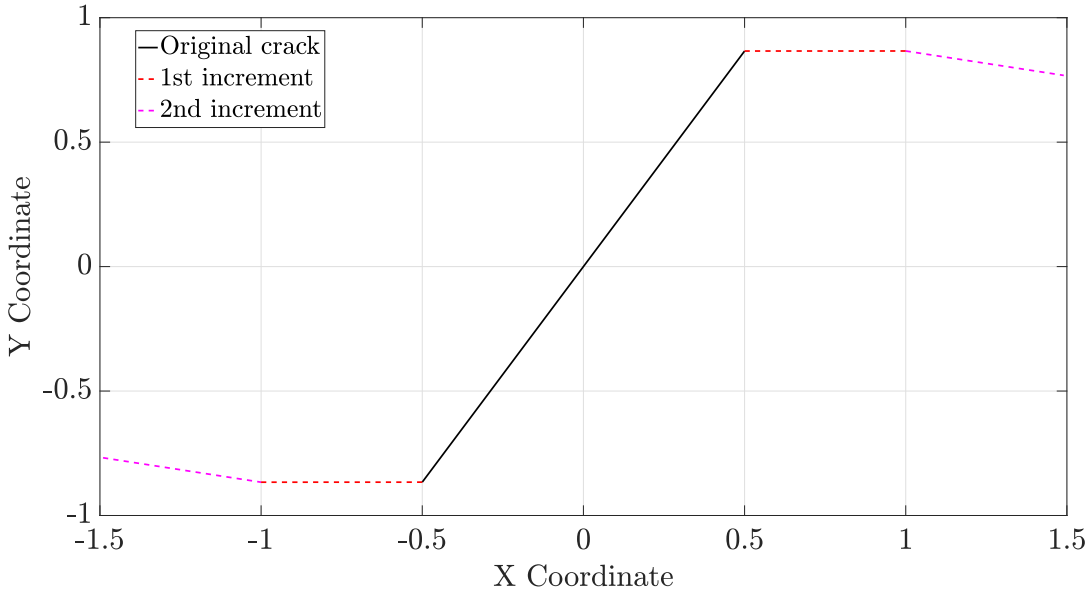


Figure 4.26: Crack propagation direction obtained by ABAQUS (MTS criteria)

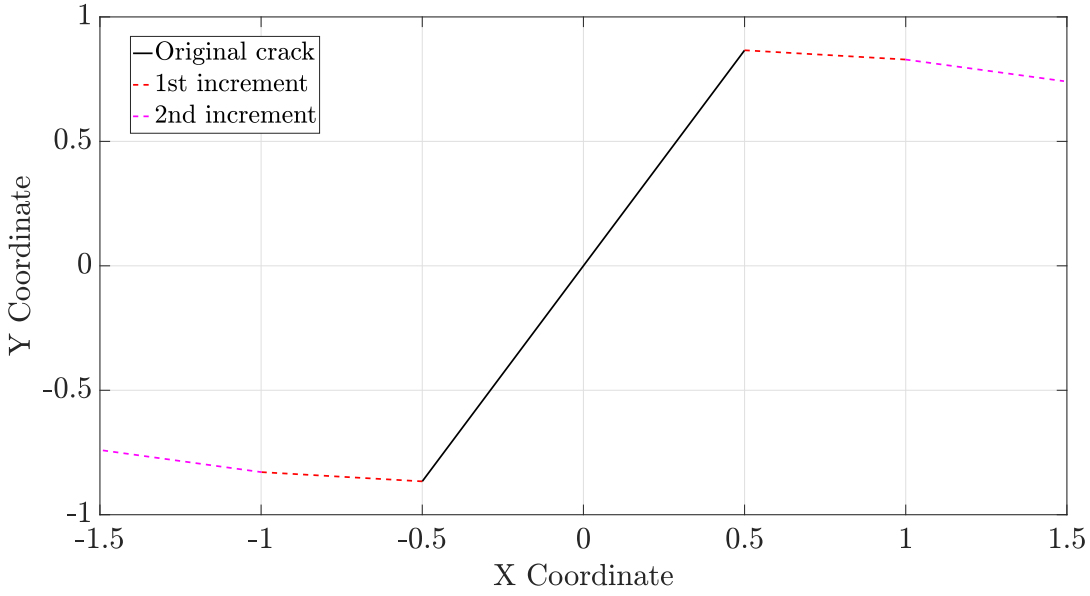


Figure 4.27: Crack propagation direction obtained by ABAQUS (MERR criteria)

Nevertheless in figure 4.27 it is possible to see that at the initial stage of crack propagation there is a small kink, showing the existence of a stress field with a maximum stress different from the tensile stress applied to the plate.

According to the MTS criteria the crack growth propagation will happen perpendicularly to the maximum stress, which as we distance ourselfs from the crack is equal to the tensile stress on the plate. If the crack tips add been increased consecutively that would be the crack path obtained.

Chapter 5

Experimental procedure: pre-crack

In order to prepare the specimens to determinate the crack path under mode II and mixed mode I-II conditions, a fatigue pre-crack had to be created using a three-point bending set up (mode I loading). It is key to ensure that the plastic region at the crack tip of the specimen (figure 5.1) is very small, so it is negligible, guaranteeing it doesn't influence the mechanical properties of the material when the crack propagation starts. To fuffil that requirement the recommendations of the document BS DD 19:1972 and the standards ASTM E399, ISO 12108-2002 were followed.

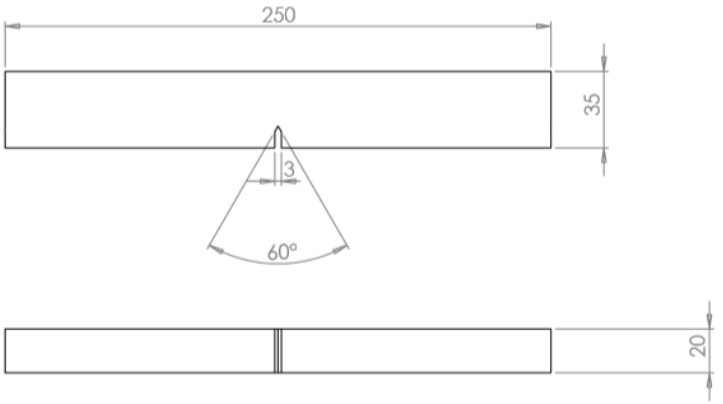


Figure 5.1: Single edge notch specimen.

5.1 Pre-crack load according to BS DD 19:1972

According to BS DD 19:1972 [36] the maximum value for the stress intensity factor, K_{max}, should satisfy the follwing condition,

$$K_f < 0.63\sigma_y B^{\frac{1}{2}} \tag{5.1}$$

from which one can obtain the value of the maximum fatigue load (P_f) using, being σ_y the yield stress,

$$K_f = \frac{YP_f}{BW^{\frac{1}{2}}} \tag{5.2}$$

The length of the fatigue pre-crack according to BS DD 19:1972 [36] for the single edge notch specimen has to satisfy the following conditions,

$$a > J + 2.5mm \qquad \text{for B} \geq 13 \text{ mm} \tag{5.3}$$

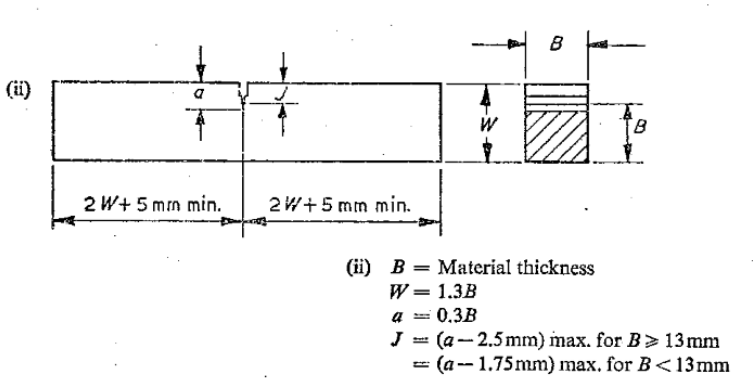


Figure 5.2: Test pieces dimensitions according to BS DD 19:1972, [36].

Where J is the size of the machined notch which is 10 mm.

The stress intensity coefficient, Y, can be extracted from table 1 of [36]. So for a total crack length of 14 mm (notch plus pre-crack) $Y = 7.89$ we have,

$$K_f < 23.1648 \qquad \text{MPa}\sqrt{\text{m}} \tag{5.4}$$

Resulting in,

$$P_f = 10985 \qquad \text{N} \tag{5.5}$$

Since the load obtained on equation 5.5 was a bit high, for safety purposes the load used in pre-cracking was 85% of P_f resulting in $P_f = 9337.25$ N. Two of the seven specimens were pre-cracked using the BS DD 19:1972.

5.2 Pre-crack load according to ASTM:E399

According to ASTM E399 [37] the stress intensity factor for the single edge notch bending specimen is obtained by,

$$K_Q = \frac{P_Q S}{BW^{\frac{3}{2}}} f\Big(\frac{a}{W}\Big) \tag{5.6}$$

where S is the distance between supports during the three point bending procedure, which takes the value of 140 mm, and the non-dimensional stress intensity factor is given by,

$$f\Big(\frac{a}{W}\Big) = 3\sqrt{\frac{a}{W}}\frac{1.99 - \Big(\frac{a}{W}\Big)\Big(1 - \frac{a}{W}\Big)\Big[2.15 - 3.93\frac{a}{W} + 2.7\Big(\frac{a}{W}\Big)^2\Big]}{2\Big(1 + 2\frac{a}{W}\Big)\Big(1 - \frac{a}{W}\Big)^{\frac{3}{2}}} \tag{5.7}$$

The length of the fatigue pre-crack (a_i) according to ASTM E647 [38] for this specimen has to satisfy the following conditions,

- $a_i \geq 0.1B$

- $a_i \geq h$
- $a_i \geq 1mm$

where h is the width of the machined notch which is 3 mm (figure 5.3).

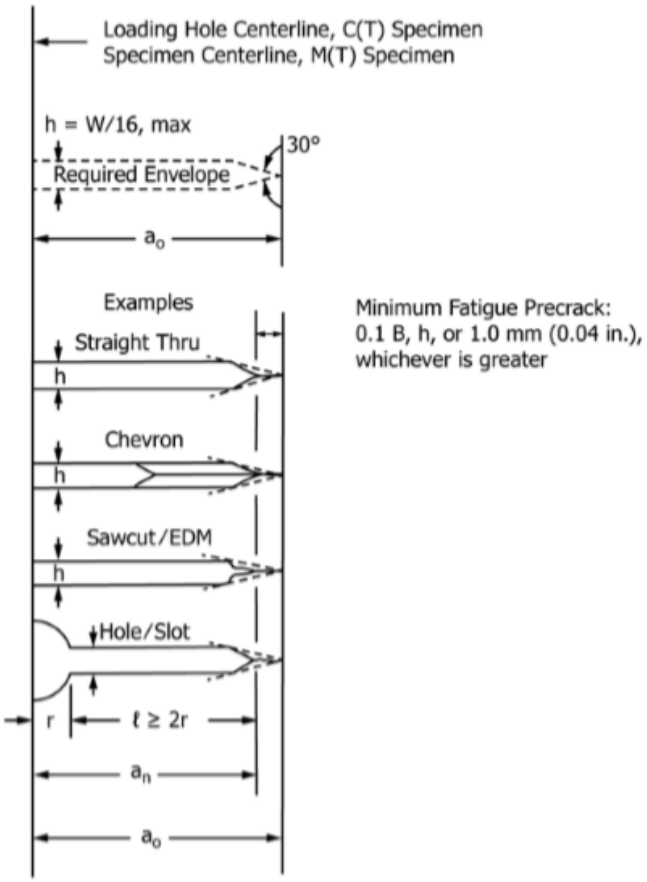


Figure 5.3: Notch details and minimum fatigue pre-cracking requirements, [38].

So the pre-crack size takes the greater value of the three conditions, and the chosen a_i was 4 mm, leading to a total crack length of 14 mm. For this crack length the value of the non-dimensional stress intensity factor $f\left(\frac{a}{W}\right)$ is,

$$f\left(\frac{a}{W}\right) = 1.9818 \tag{5.8}$$

For the used material K_Q will be equal to the value of K_c, presented in equation 3.5. By multiplying K_Q by 0.8 K_{max} can be obtained.

$$K_{max} = 0.8K_Q = 32.8 \qquad \text{MPa}\sqrt{\text{m}} \tag{5.9}$$

Using equation 5.6 the maximum fatigue load is P_Q=15482 N. The maximum fatigue load was multiplied by 0.5 due to the high load, in order to ensure there is no plastic deformation at the crack tip, resulting in,

$$P_Q = 7741 \qquad \text{N} \tag{5.10}$$

The remaining 5 specimens were pre-cracked using the ASTM E399 standard.

5.3 Pre-crack load according to ISO 12135-2016

Even though this norm was not used in this work it is still presented.

According to ISO 12135-2016 [39], the value of K_Q calculed for three-point bend specimens is,

$$K_Q = \frac{S}{W}\frac{F_Q}{\Big(B^2W\Big)^{0.5}}g_1\Big(\frac{a}{W}\Big) \tag{5.11}$$

where,

$$g_1\Big(\frac{a}{W}\Big) = \frac{3\Big(\frac{a}{W}\Big)^{0.5}\Big[1.99 - \Big(\frac{a}{W}\Big)\Big(1 - \Big(\frac{a}{W}\Big)\Big)\Big(2.15 - 3.39\Big(\frac{a}{W}\Big) + 2.7\Big(\frac{a}{W}\Big)^2\Big]}{2\Big(1 + \Big(\frac{2a}{W}\Big)\Big)\Big(1 - \Big(\frac{a}{W}\Big)\Big)^{1.5}} \tag{5.12}$$

The length of the fatigue pre-crack (a_i) according to ISO 12108-2002 [40] for this specimen has to satisfy the following conditions,

- $a_i \geq 0.1B$
- $a_i \geq h$
- $a_i \geq 1mm$

where h is the width of the machined notch which is 3 mm. So the pre-crack size takes the greater value of the three conditions, and the chosen a_i was 4 mm, leading to a total crack length of 14 mm. For this crack length the value of the non-dimensional stress intensity factor $f\Big(\frac{a}{W}\Big)$ is,

$$g_1\Big(\frac{a}{W}\Big) = 1.9818 \tag{5.13}$$

Using K_{max} as in equation 5.9 the maximum fatigue load is,

$$F_Q = 19352 \qquad \text{N} \tag{5.14}$$

To ensure no plastic deformation at the crack tip, 50% of the calculated load should be used resulting in,

$$F_Q = 9676 \qquad \text{N} \tag{5.15}$$

5.4 Pre-crack results after three-point bending

Table 5.1 presents the pre-crack dimensions (mean value) obtained in all the specimens.

It is worth noting that the fatigue crack did not grow equally on each face of the specimen, probably due to small misalignments of the specimen during the test or due to small inner impurities in the material. The differences are however small so the material is still considered isotropic. The fatigue cracks along the specimens presented a small tilt from the plane of symmetry which is also presented in the table. According to [38] the results are still valid if $\phi < 10°$, as shown on figure 5.4.

Table 5.1: Pre-crack dimensions

Specimen	**Pre-crack [mm]**	**Crack deviation [°]**
1	3.965	-8.5
2	3.115	-5
3	3.805	-3.5
4	4.175	-6
5	4	-6.5
6	3.905	3.5
7	3.85	2

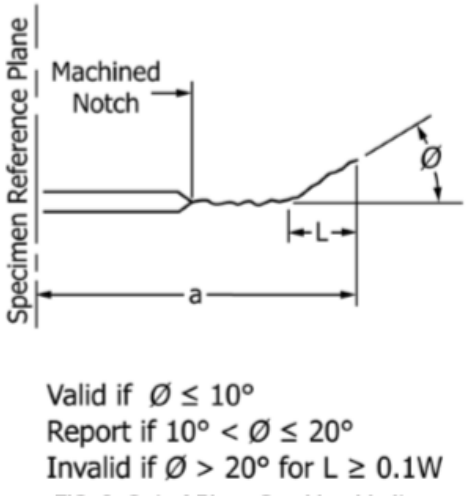


Figure 5.4: Cracking deviation limits, [38].

5.4.1 Surface polish

After concluding the three-point bend test all the specimens were polished using abrasive paper and alumina. Only the surrounding zone where the pre-crack was located was submited to this process, being that is the region of interest for the current work.

Sequency wise the specimens were first polished by hand using a 1200P SiC abrasive paper, followed by a 800P SiC paper and finallized with an alumina abrasive (1.0 μm). It should be noted that the abrasive paper polishing movement was made at $\pm 45°$ relative to the tip of the notch.

Surface polishing was made in an attempt to facilitate the visualization of the pre-crack and crack tip, making it easier to measure and track crack growth using a camera in the future four-point bend tests.

Chapter 6

Experimental procedures, results and discussion

As mensioned in chapter 3, the asymmetrical four-point bend test is used to determine the SIF's and crack paths for mode II and mixed mode I-II. All the models used for this section can be found in annex C.

6.1 Pure Mode II loading: Experimental set up and fatigue load calculation

As discussed in previous chapters the set up chosen for mode II loading is shown in figures 6.1 and 6.2.

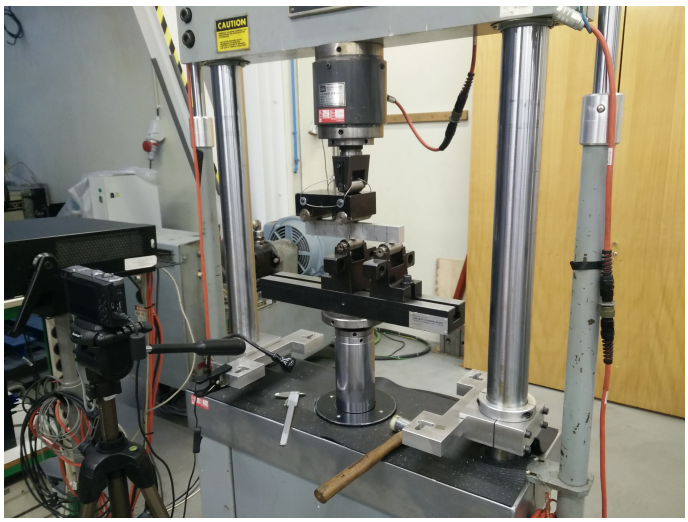


Figure 6.1: Experimental set up for four-point bend specimen under asymmetric loading (mode II loading).

In chapter 4 several thresholds of stress intensity factor range were presented. Previously an intern, Lucas Gicquel, under an internship at FEUP performed an asymmetrical four-point bending test on a specimen composed of the same aluminium alloy [41] with W=40 mm, t=20 mm, total length of 250 mm and a pre-crack of a=13 mm in order to determine the $\Delta K_{II,threshold}$ value. The distances s_1 and s_2 used according to [41] were 10 mm and 90 mm respectivly.

In Lucas Gicquel's work [41], initially no crack propagation was observed so the specimens width was reduced from 40 mm to 25 mm and a load P=35000 N was applied, which

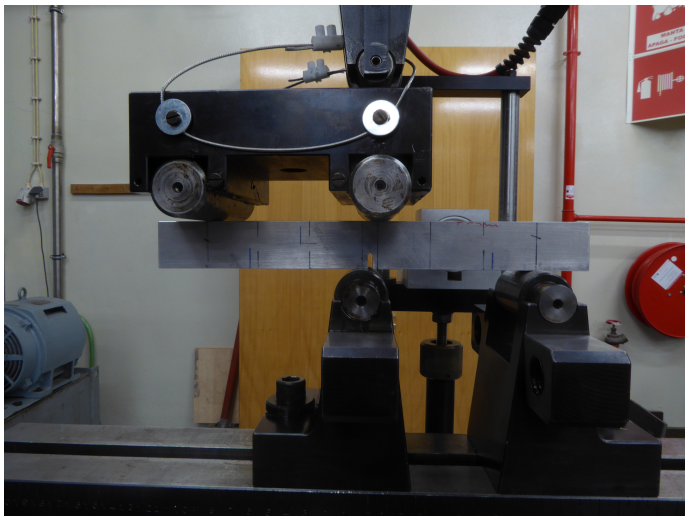


Figure 6.2: Experimental set up for four-point bend specimen under asymmetric loading (mode II loading).

led to the specimen failure, with some signs of plastic deformation (shear lips). Using equations 2.3 ($s_0 = 0$) and 2.4 with 1.20 one obtains a equivalent SIF of $K_{eq,Irwin} = 15.9$ MPa$\sqrt{\text{m}}$.

Knowing the loading ratio R is given by,

$$R = \frac{K_{min}}{K_{max}} \tag{6.1}$$

Meaning, for $R = 0.1$,

$$K_{min} = 0.1K_{max} \tag{6.2}$$

So,

$$\Delta K = K_{max} - K_{min} = K_{max} - 0.1K_{max} \tag{6.3}$$

obtaining a $\Delta K_{eq,Irwin} = 14.3$ MPa$\sqrt{\text{m}}$.

As it was stated before, the threshold values for the mode II SIF are generally unknown, so the way all experiments were carried out is going to be described. Initially, bearing in mind the mode II SIF threshold value obtained by Gicquel, the force necessary to obtain a $K_{eq,Irwin} = 12.7$ MPa$\sqrt{\text{m}}$ was calculated. The reasoning behind starting at this threshold value and not at $K_{eq,Irwin} = 15.9$ MPa$\sqrt{\text{m}}$ was to ensure that in case of failure, the specimen wouldn't suffer a high plastic deformation. This aluminum alloy is very ductile and exhibits shear lips with intensive plastic deformation, making it harder to observe the crack path after fracture. The specimen would be under the calculated load until it showed signs of crack propagation, if at the end of a considerable number of cycles no changes were verified the load P would be increased by roughly 10% and the whole process would be repeated until crack growth occured. In order to verify if there was any noticible crack growth, during the fatigue test, at the end of a certain number of cycles, the crack would be examined under a microscope that was set up on one face of the specimen, as seen in figure 6.3.

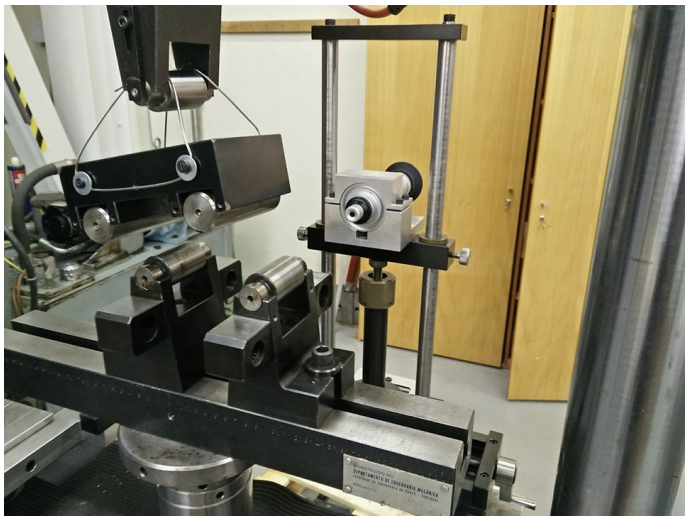


Figure 6.3: Experimental set up for four-point bend specimen under asymmetric loading (mode II loading).

Initially it was assumed, using Gicquel's work as frame of reference, that the threshold value for crack propagation would be $K_{II,threshold} = 12.7$ MPa$\sqrt{\text{m}}$.

In the present study, according to figure 2.1, the chosen position of the supports was $s_1 = 95$ mm and $s_2 = 5$ mm (figure 6.4). Bearing this in mind, using equations 2.3 ($c_0 = s_0$), 2.4, 6.1, 6.2 and 6.3 the load that had to be applied to achieve a $K_{eq,Irwin} = 12.7$ MPa$\sqrt{\text{m}}$ was calculated for specimen number 1 (pre-crack length = 13.965 mm as median value). A detailed figure of the original specimen can be seen in figure 6.5.

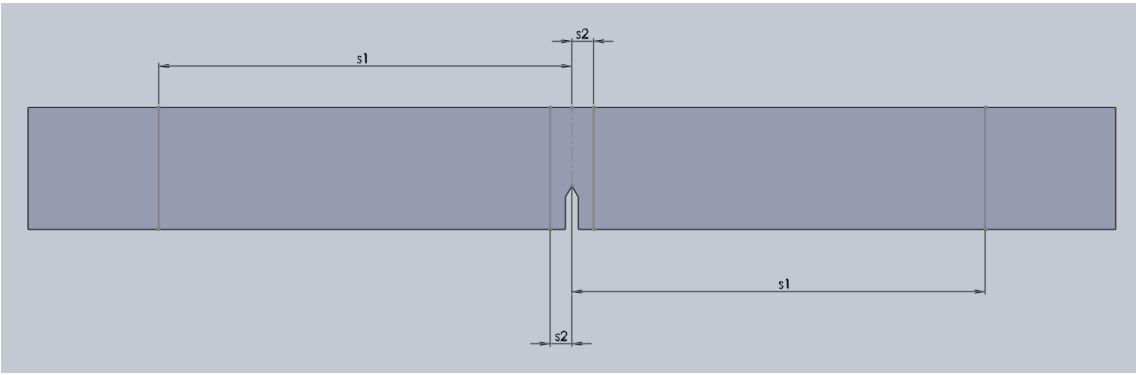


Figure 6.4: Single edge notch bending specimen 1 set up sketch.

For this specimen the geometric factors, F_I and F_{II}, presented in 2.6 and 2.7 were also calculated, being,

$$F_I = 1.2614 \tag{6.4}$$

$$F_{II} = 4.0540 \tag{6.5}$$

Resulting in a applied force of $P = 40060.1$ N in order to achieve $K_{eq,Irwin} = 12.7$ MPa$\sqrt{\text{m}}$.

The specimen was under asymmetrical four-point bending fatigue loading for 90000 cycles with a load ratio of $R = 0.1$ and no crack growth was observed, meaning that the

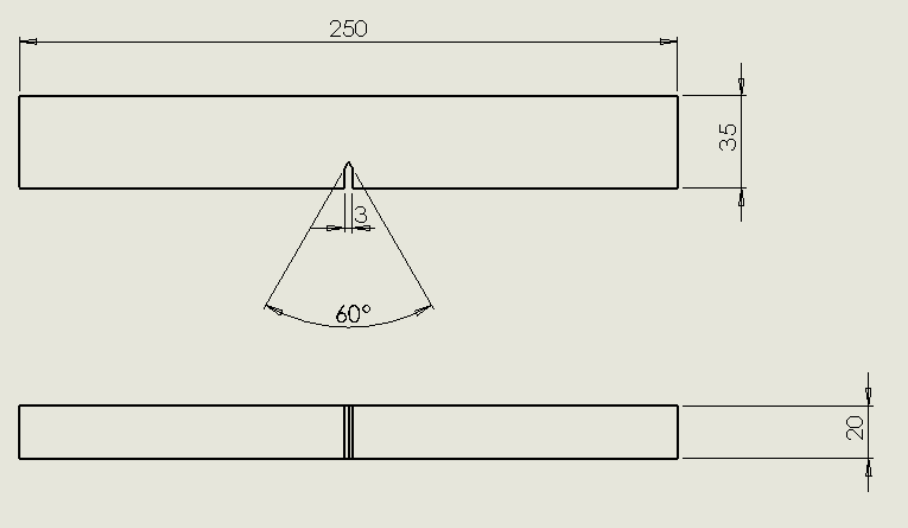


Figure 6.5: Single edge notch bending specimen (W=35).

value of $K_{II,threshold} = 12.7$ MPa$\sqrt{\text{m}}$ at the crack tip was not high enougth to enable crack growth.

The solution that was brougth up consisted in machining the specimen, removing 10 mm of width, ending up with a total of 25 mm of width. However only 7 mm were removed (figure 6.6).

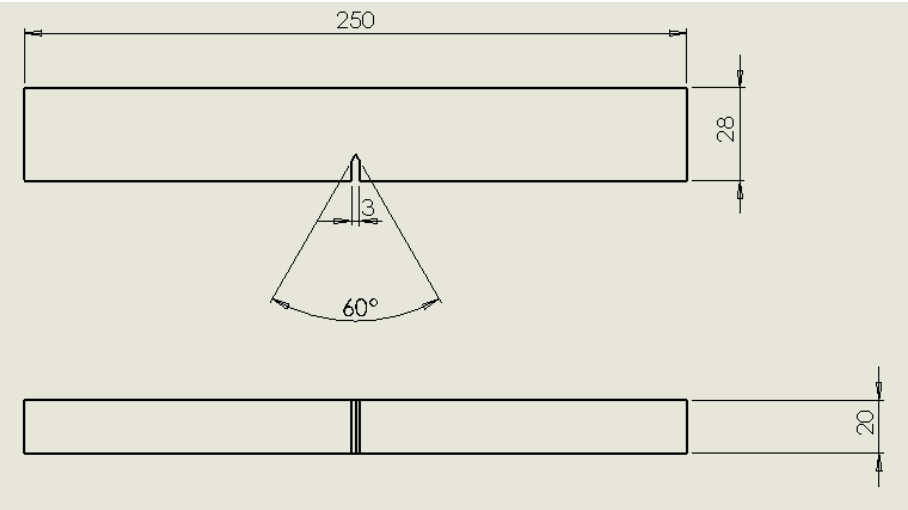


Figure 6.6: Single edge notch bending specimen with reduced width (W=28).

Where the new geometric factors F_I and F_{II} are,

$$F_I = 1.4909 \tag{6.6}$$

$$F_{II} = 3.4399 \tag{6.7}$$

The threshold value was uped from 12.7 MPa$\sqrt{\text{m}}$ to 16.6 MPa$\sqrt{\text{m}}$, which equals to approximately $\Delta K_{eq,Irwin} = 15$ MPa$\sqrt{\text{m}}$. The new load value was obtained, being $P = 36000$ N. The specimen was under stress for 85000 cycles and again no visible crack growth was noted.

With no visible crack growth the load was increased 10% (rounding up) to $P = 40000$ N equating to $\Delta K_{eq,Irwin} = 16.6$ MPa$\sqrt{\text{m}}$.

After 52500 cycles at $P = 40000$ N the load was again raised 10% since no visible crack growth was verified. So for $P = 44000$ N the range of the equivalent SIF equates to $\Delta K_{eq,Irwin} = 18.2$ MPa$\sqrt{\text{m}}$. For this last iteration it was possible to propagate the crack and the test was stoped after 56475 cycles. The frequency used for this case was 2 Hz. In order to sum up the procedure, table 6.1 is presented,

Table 6.1: Data for the fatigue tests for specimen 1 under pure Mode II loading

Width [mm]	P **[N]**	K_{eq} **MPa$\sqrt{\text{m}}$[1.20]**	ΔK_{eq} **MPa$\sqrt{\text{m}}$**	**No. of cycles**	**Obs.**
35	40060.1	12.7	11.4	90000	No growth
28	36000.0	16.6	14.9	85000	No growth
28	40000.0	18.4	16.6	52500	No growth
28	44000.0	20.3	18.2	56475	Growth

6.1.1 Shear force and bending moment diagrams

Using solid mechanics one can define the shear force and bending moment at any section of the bar. Considering the part that holds both top supports as a beam, the force transmited to the top supports (rolls), according to figure 6.7 can be given by,

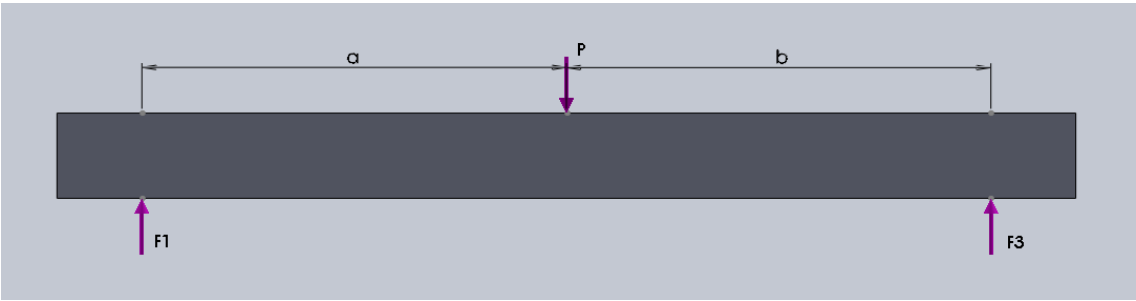


Figure 6.7: Simplified representation of the forces acting on top beam.

$$F_1 = \frac{b \times P}{a + b} \tag{6.8}$$

$$F_3 = \frac{a \times P}{a + b} \tag{6.9}$$

so for an asymmetric four-point bending test considering figures 6.4 and 6.8,

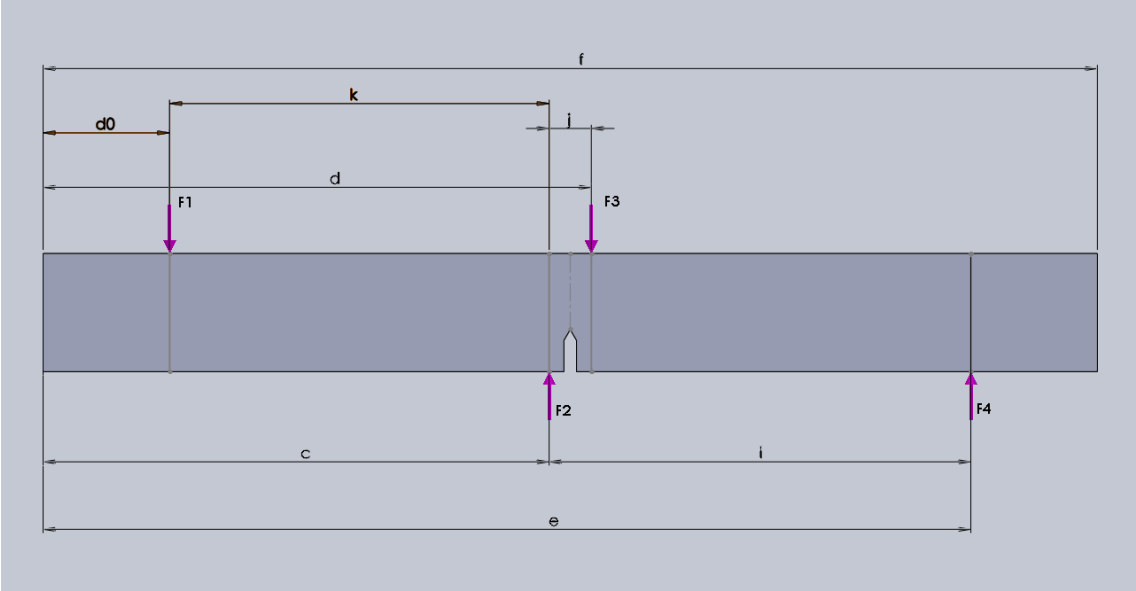


Figure 6.8: Simplified representation of the forces acting on the specimen.

$$F_4 = \frac{F3 \times j - F1 \times k}{i} \tag{6.10}$$

$$F_2 = F1 + F3 - F4 \tag{6.11}$$

Where F_1 and F_3 are the forces transmited from the top supports to the specimen, and F_2 and F_4 are the forces from the bottom supports.

So for $0 \leq x_1 \leq d_0$, being d_0 the distance from the beginning of the bar ($x = 0$) to the first top support,

$$Q_1 = 0 \tag{6.12}$$

$$M_1 = x_1 \times Q_1 \tag{6.13}$$

For $d_0 \leq x_2 \leq c$ being c the distance from the beginning of the bar ($x = 0$) to the first bottom support,

$$Q_2 = F_1 \tag{6.14}$$

$$M_2 = -F_1 \times (x_2 - d_0) \tag{6.15}$$

For $c \leq x_3 \leq d$ being d the distance from the beginning of the bar ($x = 0$) to the second top support,

$$Q_3 = F_1 - F_2 \tag{6.16}$$

$$M_3 = -F_1 \times (x_3 - d_0) + F_2 \times (x_3 - c) \tag{6.17}$$

For $d \leq x_4 \leq e$ being e the distance the beginning of the bar ($x = 0$) until the second bottom support,

$$Q_4 = F_1 + F_3 - F_2 \tag{6.18}$$

$$M_4 = -F_1 \times (x_4 - d_0) + F_2 \times (x_4 - c) - F_3 \times (x_4 - d) \tag{6.19}$$

Finally for the last section of the specimen, for $e \leq x_5 \leq f$ being f the distance the beginning of the bar ($x = 0$) until the end of the specimen ($x = 250$),

$$Q_5 = F_1 + F_3 - F_2 - F_4 \tag{6.20}$$

$$M_5 = -F_1 \times (x_5 - d_0) + F_2 \times (x_5 - c) - F_3 \times (x_5 - d) + F_4 \times (x_5 - e) \tag{6.21}$$

Using the equations presented above, for a load of $P = 44000$ N using $s_1 = 95$ mm and $s_2 = 5$ mm, the shear force and bending moment diagrams are presented,

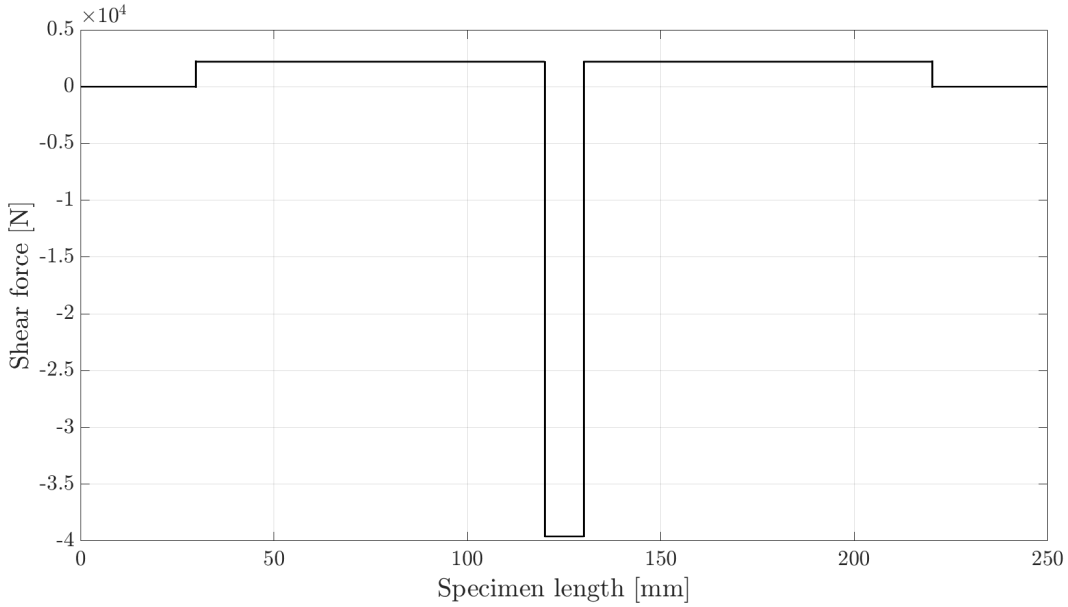


Figure 6.9: Shear force diagram for the experimental pure mode II loading.

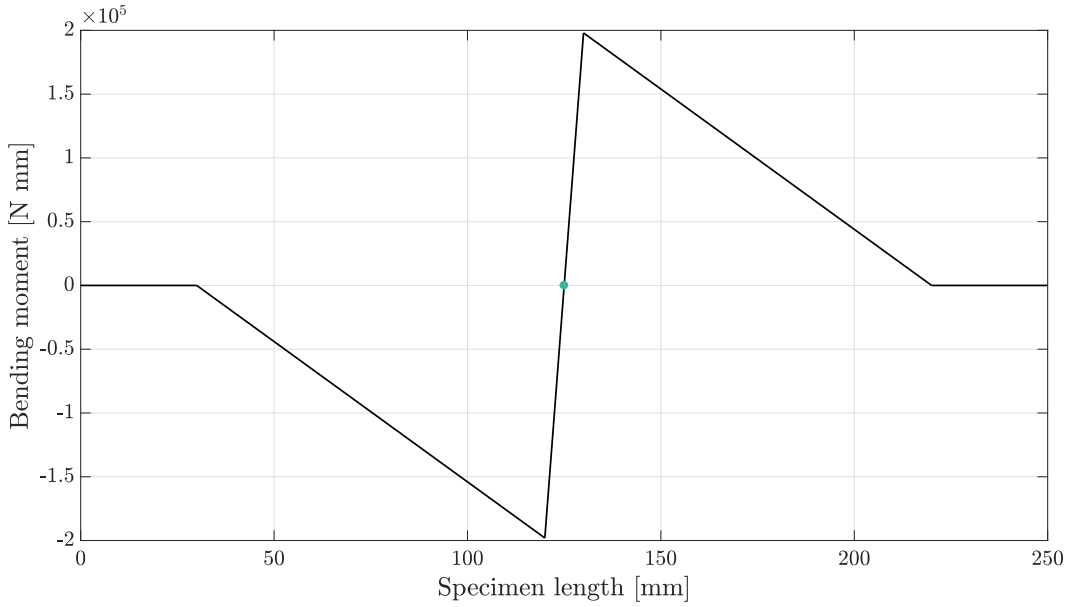


Figure 6.10: Bending moment diagram for the experimental pure mode II loading.

As it can be seen, at the crack plane ($x = 125$ mm) the bending moment is theoretically null, leaving the crack under pure shear stresses.

6.1.2 Numerical model: Crack propagation path

In order to determine the crack path the extended finite element method (xFEM), available on ABAQUS, was used. This method allows the modelling of crack and crack growth without remeshing, since it is a fully mesh independent technique. Otherwise to study the evolution of the crack and crack path propagation one would have to redo and remesh the crack increment by increment, similarly to what was done in section 5.2.6. Throughout the experimental procedure, several pictures were taken of each side of the specimen. Using an image digitizer (figure 6.11 e 6.12) it was possible to trace the crack path of each side, perform a median and compare it to path obtained using ABAQUS xFEM feature.

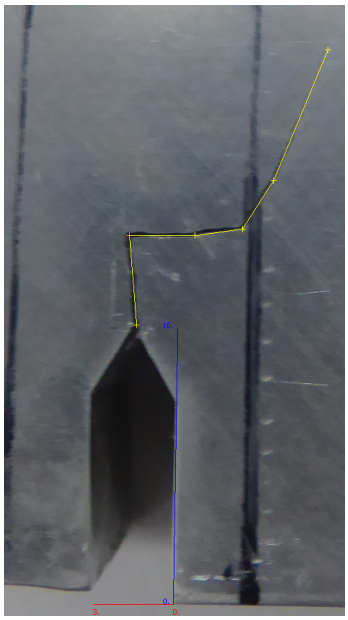


Figure 6.11: Crack path obtained with image digitizer for one face of specimen 1.

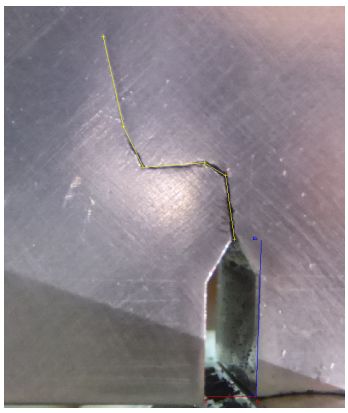


Figure 6.12: Crack path obtained with image digitizer for the other face of specimen 1.

The model represented in figure 6.13 used a coarse mesh on the crack domain with elements with 2 mm length (seed size 2), the rest of the mesh is structured and the elements have 3 mm length (seed size 3).

In order to compare the mesh influence in xFEM a finer mesh was used with elements with 1 mm length (seed size 1) in the crack region, obtaining,

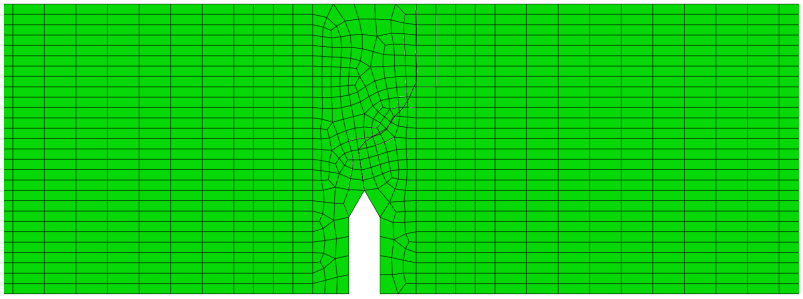


Figure 6.13: Crack path obtained with xFEM for coarse mesh - specimen 1.

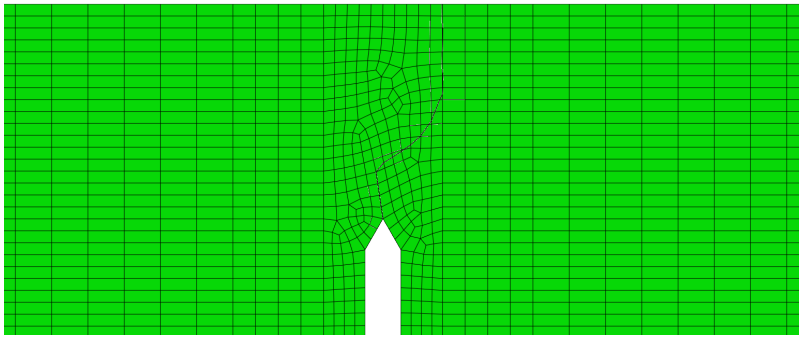


Figure 6.14: Crack path obtained with xFEM for fine mesh - specimen 1.

The numerical results obtained were then compared to the experimental crack path, presented in figure 6.15,

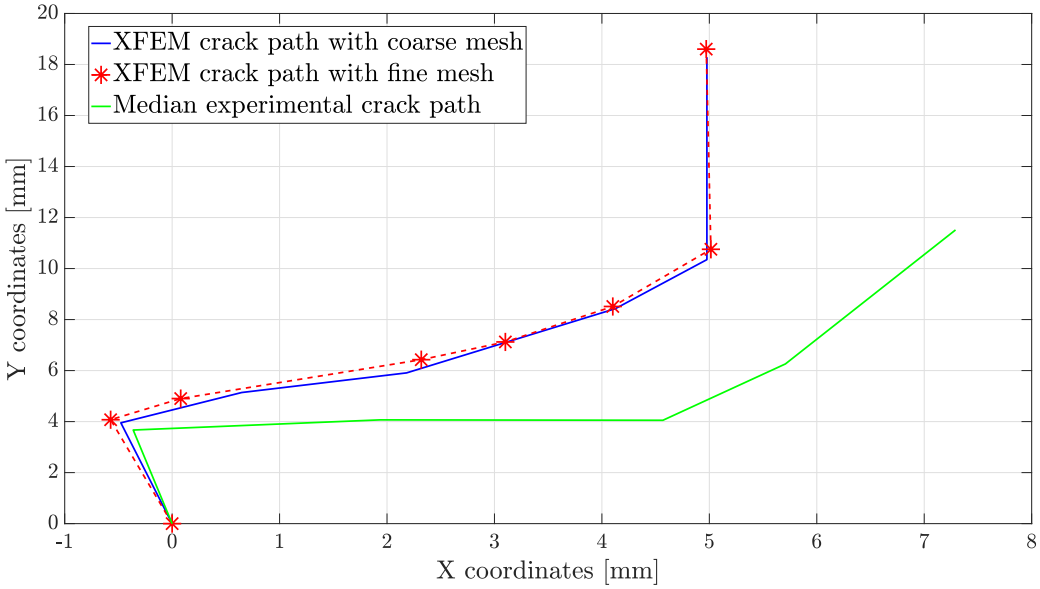


Figure 6.15: Comparison between crack path obtained with xFEM for fine mesh, coarse mesh and experimental crack path - specimen 1.

As it can be seen, there are no meaningfull differences in the crack path obtained from the model with coarse and fine mesh. However the crack paths obtained by finite element analysis either using a coarse or a fine mesh are different from the one obtained experimentally.

6.1.3 Discussion

According to [29], for a high R ratio, the presence of mode II loading increases the crack tip plasticity, thus accelerating crack growth. However, this experiment was done at a low R ratio ($R = 0.1$), which delays crack growth notably, producing rough crack surfaces [29]. This way one can say the existence of a mode II component, being this a case of pure mode II, introduces roughness induced crack closure, enhancing friction and the rubbing of the crack surfaces during cyclic loading, resulting in reduced crack tip opening displacement and crack arrest, delaying fatigue failure and leading to higher threshold results [29].

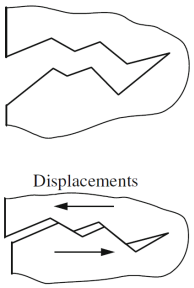


Figure 6.16: Roughness-induced crack closure, [12].

This may be a factor that can help explain why mode II SIF threshold is higher than the mode I SIF thresholds presented at chapter 4. In opening mode the friction between crack surfaces does not exist, lowering the value of the mode I SIF threshold. Since the goal of this test was to emulate pure Mode II loading, it was expected that the threshold could be higher than the known Mode I threshold SIF values.

6.2 Mixed mode I-II loading ($\beta = 13°$): Experimental set up and fatigue load calculation

After the experiment procedure for pure Mode II loading was concluded, the next situation chosen was one where mode II still had a bigger weight than mode I. Using specimen 4, which has the same dimensions as specimen 1, the cenario recreated was that of $\frac{K_I}{K_{II}} = 0.23$, which is equal to a $\beta = \tan \frac{K_I}{K_{II}} = 13°$.

Ideally one would examine the crack behaviour for a consistent number of increments of $\beta = 15°$, however that was not possible with the present resources since, as it can be seen in 2.4, the $\frac{K_I}{K_{II}}$ ratio is extremelly sensitive to the load distance for the crack plane (s_0). For a distance of 1 mm from the crack plane (s_0=1 mm), $s_1 = 95$ mm and $s_2 = 5$ mm, according to equations 2.3 and 2.4 the closest $\frac{K_I}{K_{II}}$ ratio to $\beta = 15°$ was $\frac{K_I}{K_{II}} = 0.23 = \beta = 13.22°$.

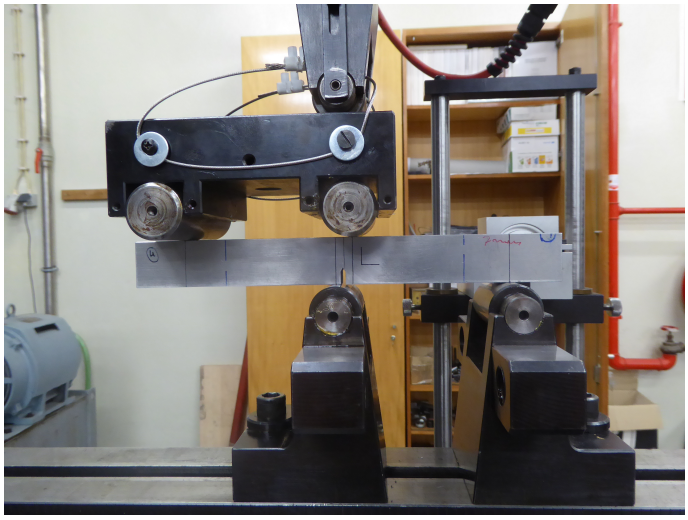


Figure 6.17: Experimental set up for four-point bend specimen number 4 under asymmetric loading (mixed mode I-II $\beta = 13°$)

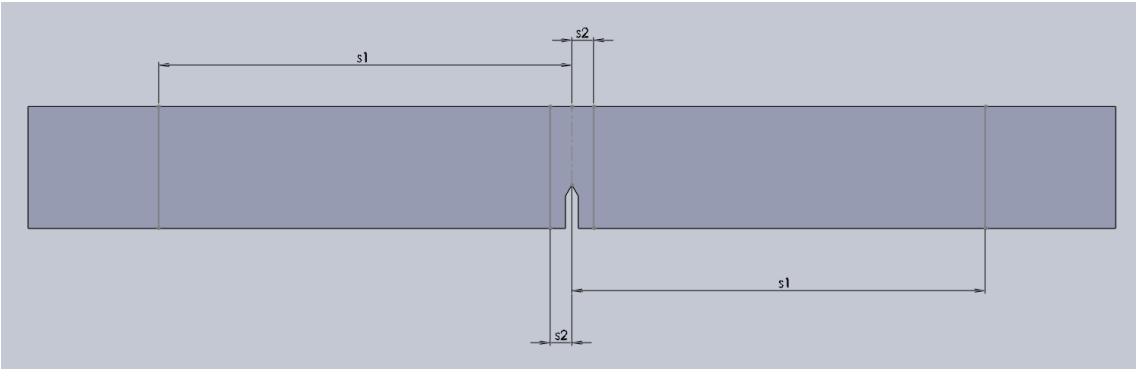


Figure 6.18: Single edge notch bending specimen 4 set up sketch.

In theory, the SIF threshold value K_{eq} for this case should be lower than the one in pure Mode II loading since the mode I SIF now has a bigger weigth. Bearing this in mind the chosen starting value for the load P was 37000 N, which equates to a $K_{eq,Irwin} = 17.8$

MPa$\sqrt{\text{m}}$ or $\Delta K_{eq,Irwin} = 16$ MPa$\sqrt{\text{m}}$. After 68697 cycles at a frequency of 2 Hz, which remained unchanged throughout this procedure, no crack growth was observed. This led to a increase of the load to $P = 41000$ N resulting in a $K_{eq,Irwin} = 19.7$ MPa$\sqrt{\text{m}}$ or $\Delta K_{eq,Irwin} = 17.75$ MPa$\sqrt{\text{m}}$ and after 59613 cycles no crack growth was visible. The load was raised to a value of $P = 43000$ N ($K_{eq,Irwin} = 20.69$ MPa$\sqrt{\text{m}}$ or $\Delta K_{eq,Irwin} = 18.62$ MPa$\sqrt{\text{m}}$). Once again, after 191001 cylces no changes were observed and the load was further increased to 44000 N, equating to $K_{eq,Irwin} = 21.2$ MPa$\sqrt{\text{m}}$ or $\Delta K_{eq,Irwin} = 19.1$ MPa$\sqrt{\text{m}}$. The specimen was under these conditions for an aditional 21825 cycles, with no change, leading to an load increase to $P = 46000$ N, equating to $K_{eq,Irwin} = 22.13$ MPa$\sqrt{\text{m}}$ or $\Delta K_{eq,Irwin} = 19.92$ MPa$\sqrt{\text{m}}$. For this load the specimen started to show signs of crack growth, failling after 24256 cycles. Table 6.2 presents the information in an organized fashion,

Table 6.2: Data for the fatigue test for specimen 4 under mixed mode I-II loading ($\beta = 13°$)

Width [mm]	P **[N]**	K_{eq} **MPa$\sqrt{\text{m}}$[1.20]**	ΔK_{eq} **MPa$\sqrt{\text{m}}$**	**No. of cycles**	**Obs.**
28	37000.0	17.8	16.0	68697	No growth
28	41000.0	19.7	17.8	59613	No growth
28	43000.0	20.7	18.6	191001	No growth
28	44000.0	21.2	19.1	21825	No growth
28	46000.0	22.1	19.9	24256	Growth

6.2.1 Shear force and bending moment diagrams

Using the same equations as the previous section the shear force and bending moment diagrams are presented bellow,

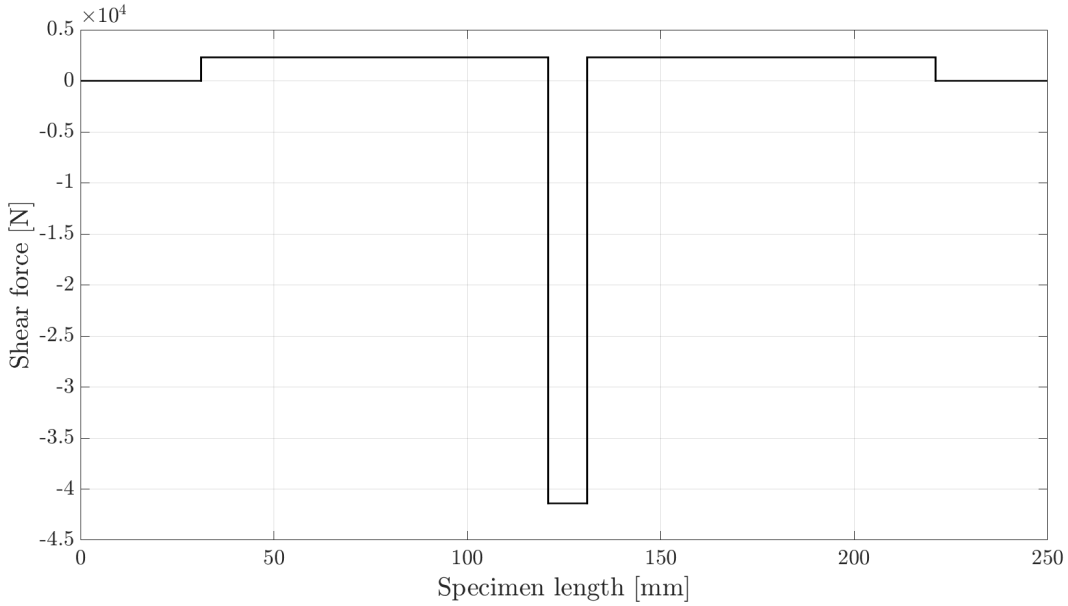


Figure 6.19: Shear force diagram for the experimental mixed mode loading I-II($\beta = 13.22°$, $P = 46000$ N

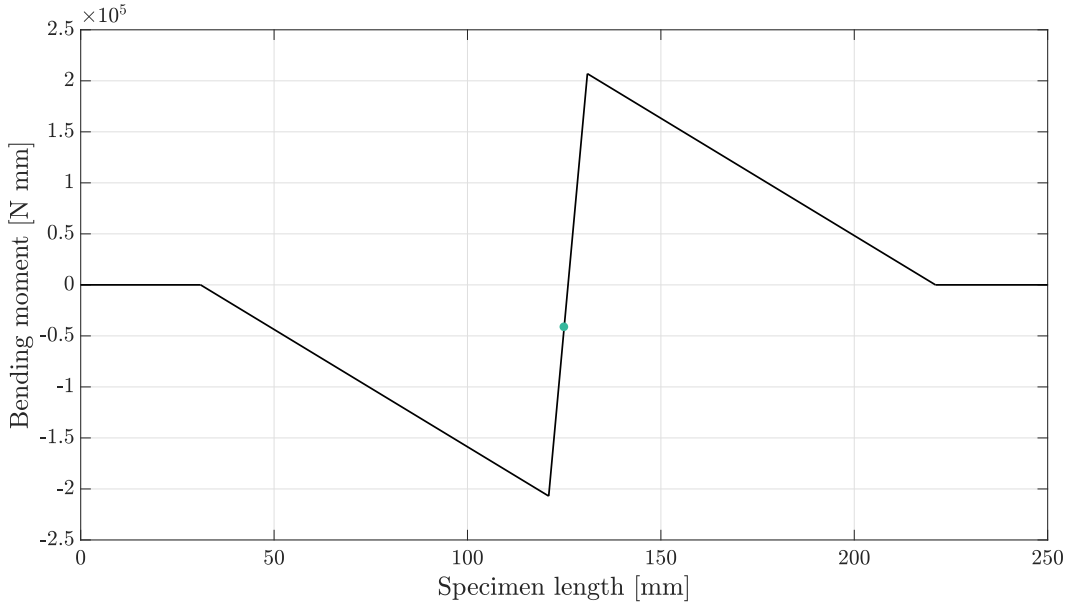


Figure 6.20: Bending moment diagram for the experimental mixed mode loading I-II($\beta = 13.22°$, $P = 46000$ N

As it can be seen, the crack plane is under the maximum shear force and a bending moment of -41400 N·mm.

6.2.2 Numerical model: Crack propagation path

As in the previous section, the crack paths using xFEM were created for this situation and compared with the experimental results. The crack path for the correct specimen position was also added to the comparision, this will be further explained at the discussion.

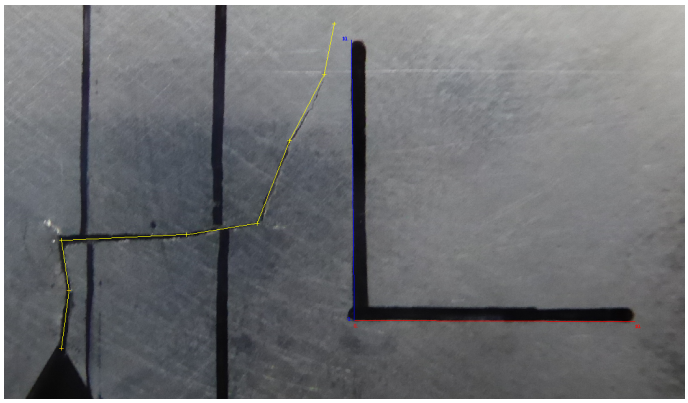


Figure 6.21: Crack path obtained with image digitizer for one face of specimen 4.

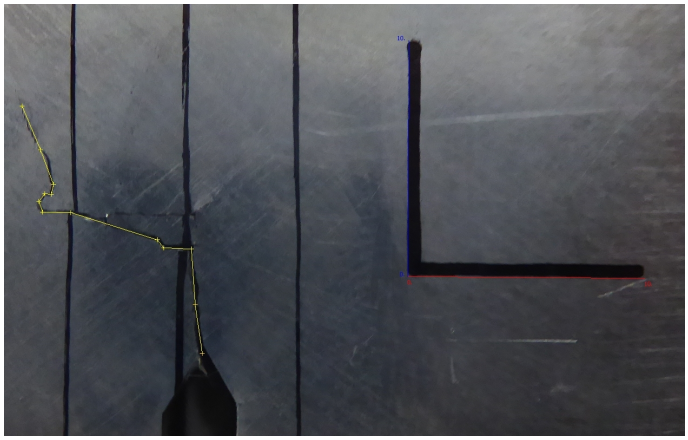


Figure 6.22: Crack path obtained with image digitizer for the other face of specimen 4.

The models represented in figures 6.23 and 6.24 used a fine mesh on the crack domain with elements with 1 mm length (seed size 1), the rest of the mesh is structured and the elements have 3 mm length (seed size 3). No median was made between the crack path obtained from figures 6.21 and 6.22 since they are quite different.

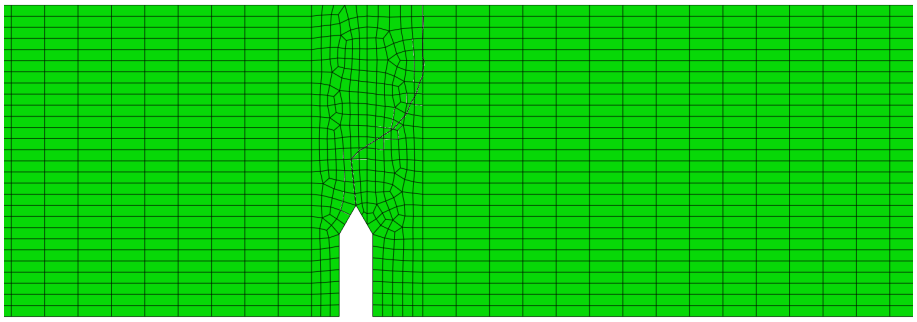


Figure 6.23: Crack path obtained with xFEM for specimen 4.

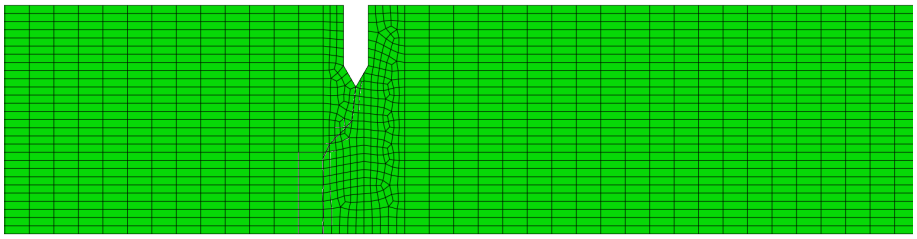


Figure 6.24: Crack path obtained with xFEM specimen 4 (corrected).

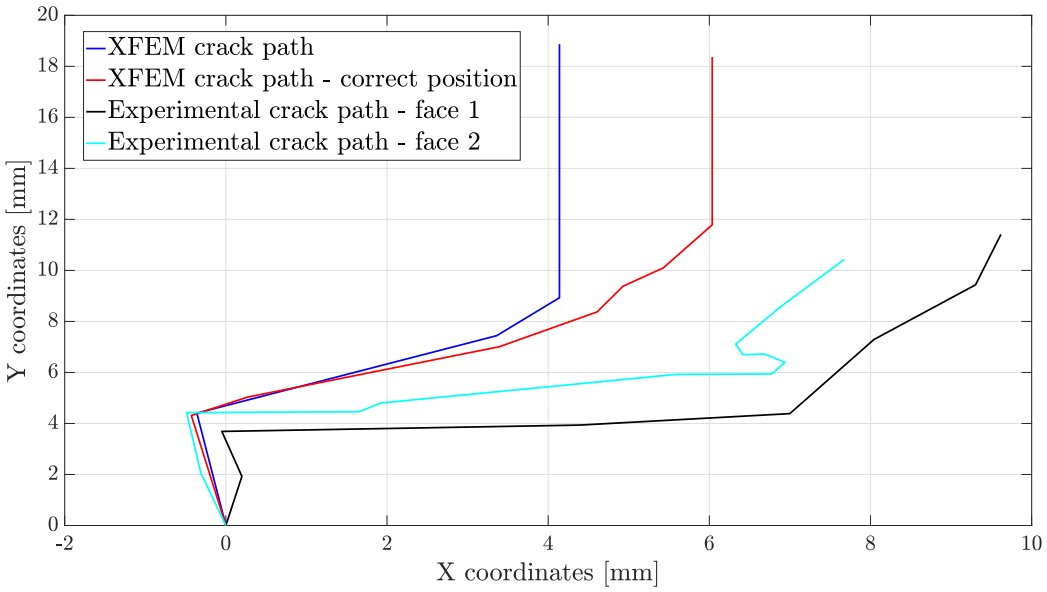


Figure 6.25: Comparison between crack path obtained with xFEM for specimen 4 and experimental crack path.

6.2.3 Discussion

Firstly, by looking at table 6.2 it can be said that the enabling of crack growth in this situation was slightly harder than in the pure Mode II loading condition, since the growth was verified for a bigger number of cylces and equivalent SIF value. This contradicts what was expected, the presence of opening mode (mode I) should make it easier to enable crack growth. It was only after specimen 5 was tested, which will be presented after the next section, that it was understood that the experimental procedure for this situation was wrongly done.

By observing the bending moment diagram presented in figure 6.20 it can be seen that the crack plane is located at a region where the bending moment is negative. So on the left hand side relative to center of the beam, the top surface of the specimen is under traction and bottom surface under compression (figure 6.26). This explains why it was harder to induce crack growth, even with the presence of mode I loading. The crack plane was at the bottom surface, so the crack surfaces were being compressed against each other, promoting the contact of the crack flanks durying the load cycles, increasing friction and delaying crack growth and fatigue failure.

As for the crack paths obtained, the ones obtained via ABAQUS are different from one another since each represents a different situation at the crack plane, being the blue crack path representitive of compression at the crack plane and the red representitive of tension. By observing the experimental crack paths they vary quite a lot from face to face and from the xFEM simulation. In figure 6.22 multiple can be seen, which was unnexpected.

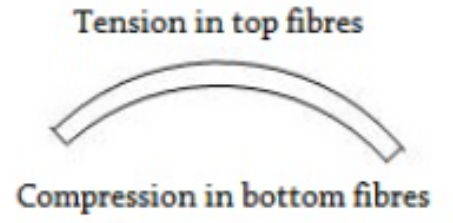


Figure 6.26: Left hand side of specimen

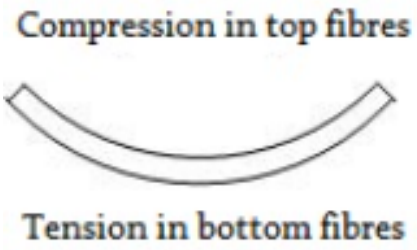


Figure 6.27: Right hand side of specimen

6.3 Mixed mode I-II loading ($\beta = 48°$): Experimental set up and fatigue load calculation

In the following experiment each mode had almost the same contribution $\frac{K_I}{K_{II}} = 1.10$ ($\beta = 48°$). The set up had an the distances $s_1 = 85$ mm, $s_2 = 15$ mm and $s_0 = 4$ mm. The specimen used was specimen number 3, which as a smaller width than the previous two ($W = 25$ mm), shown in figure 6.28. Since this specimen presents a smaller width

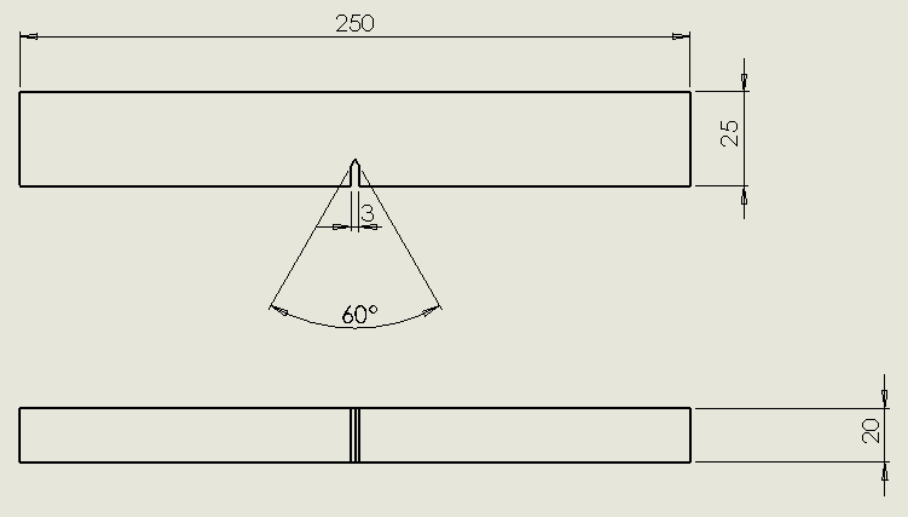


Figure 6.28: Single edge notch bending specimen with reduced width (W=25 mm).

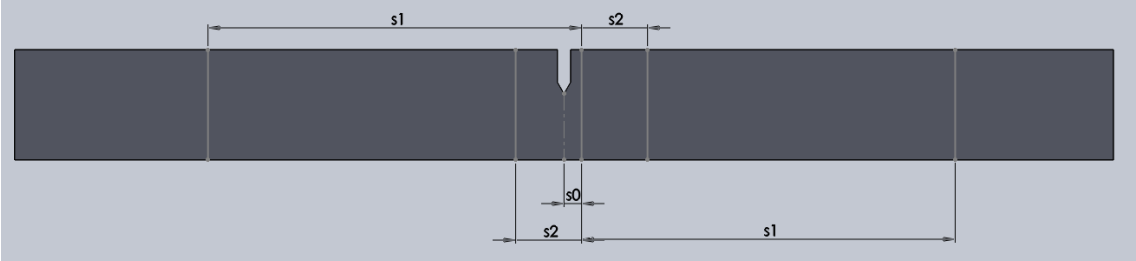


Figure 6.29: Single edge notch bending specimen 3 set up sketch.

than the previous ones and the presence of opening mode (mode I) is higher, the loads were calculated in order to obtain an approximate value of $K_{eq,Irwin} = 13.34$ MPa$\sqrt{\text{m}}$ ($\Delta K_{eq,Irwin} = 12$ MPa$\sqrt{\text{m}}$), which according to equations 2.3, 2.4 is achieved for a load of $P = 21000$ N. It should be noted that this test was carried out at a frequency of 8 Hz.

In this case, the load did not have to be increased, since crack growth was observed after approximatly 8000 cycles being that the test was stoped at 13968 cycles.

Table 6.3: Data for the fatigue test for specimen 3 under mixed mode I-II loading ($\beta = 48°$)

Width [mm]	P **[N]**	K_{eq} **MPa$\sqrt{\text{m}}$[1.20]**	ΔK_{eq} **MPa$\sqrt{\text{m}}$**	**No. of cycles**	**Obs.**
25.0	21000.0	13.3	12	13968.0	Growth

6.3.1 Shear force and bending moment diagrams

The shear force and bending moment are presented bellow,

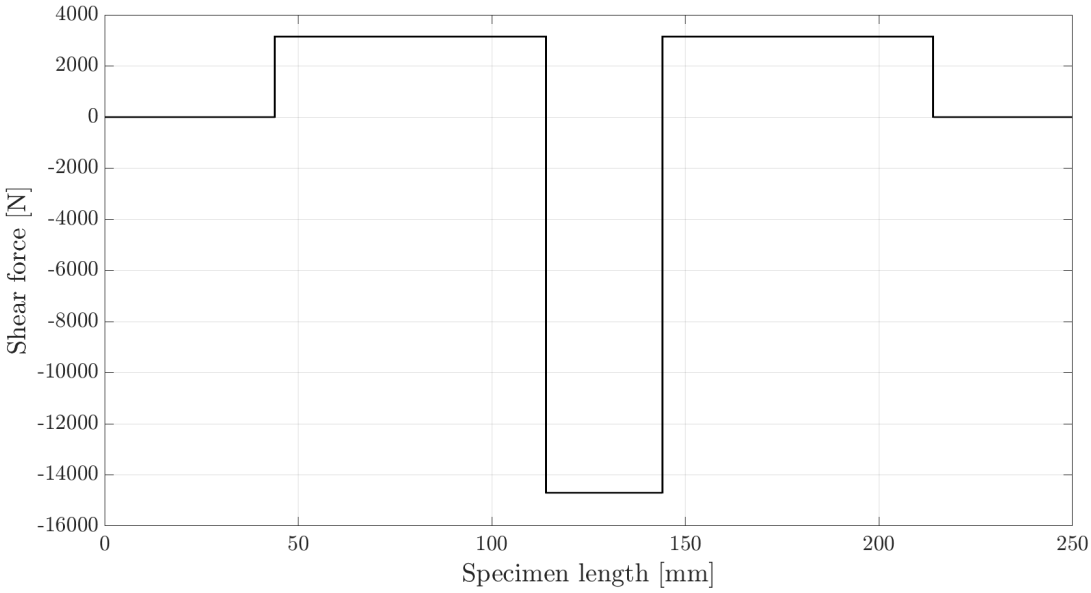


Figure 6.30: Shear force diagram for the experimental mixed mode loading I-II ($\beta = 47.8°$, $P = 21000$ N).

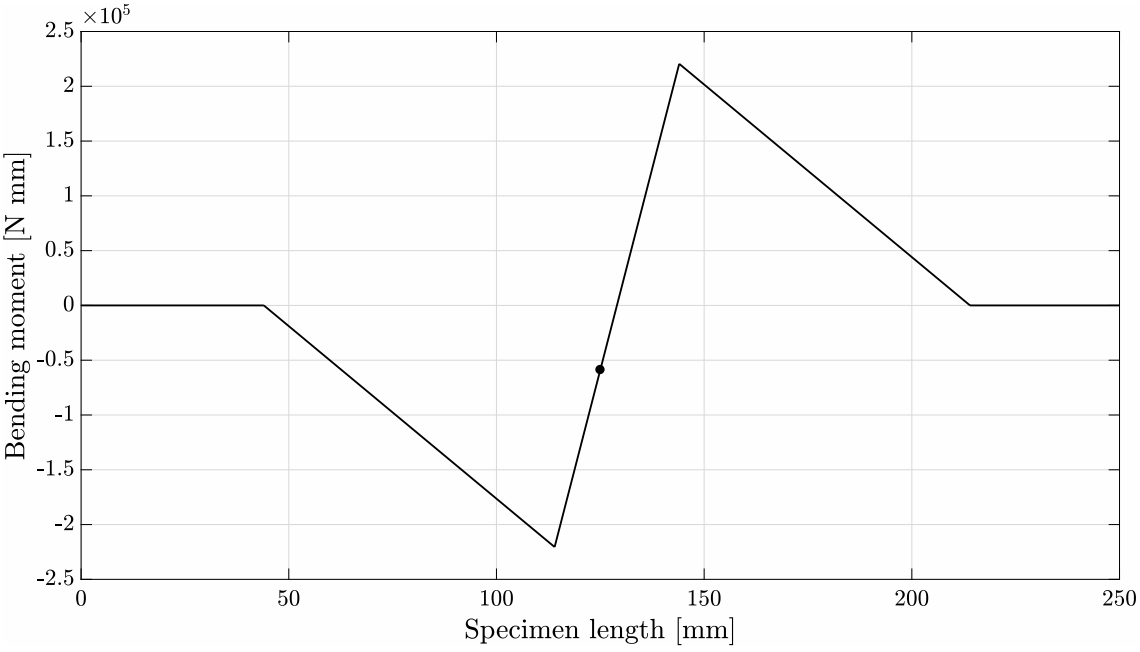


Figure 6.31: Bending moment diagram for the experimental mixed mode loading I-II ($\beta = 47.8°$, $P = 21000$ N).

Where the bending moment at crack plane is -58800 N·mm.

6.3.2 Numerical model: Crack propagation path

Using the same methology, the crack paths from the crack path of specimen 3 were ploted using a plot digitizer.

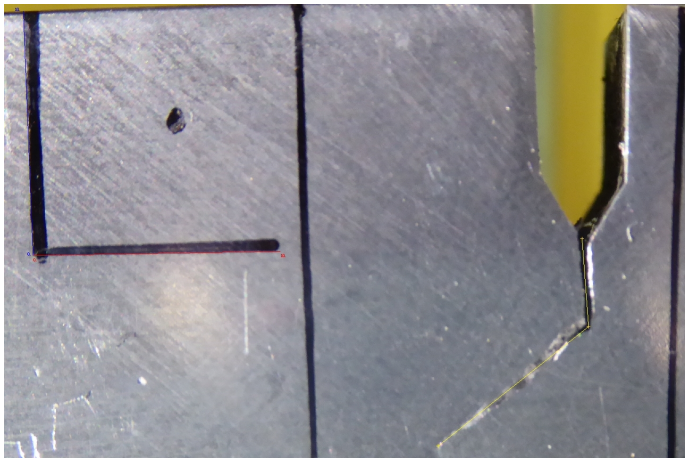


Figure 6.32: Crack path obtained with image digitizer for one face of specimen 3.

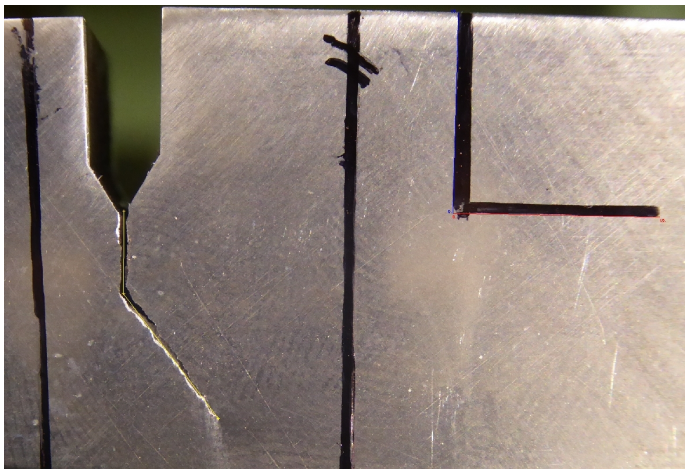


Figure 6.33: Crack path obtained with image digitizer for the other face of specimen 3.

Two models were created, one with a mesh with 1 mm element size at the crack domain and another with 0.5 mm element size presented in figures 6.34 and 6.35 respectivly (the rest of the mesh had 3 mm elements).

The numerical results obtained were then compared to the experimental median crack path, presented in figure 6.36,

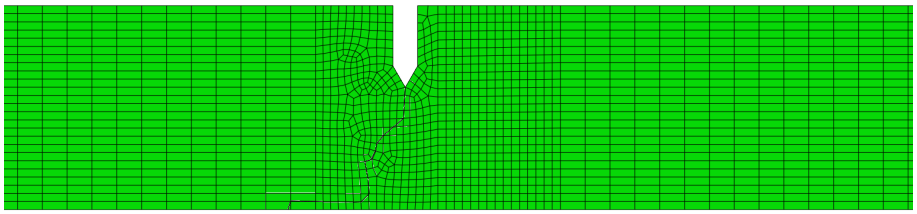


Figure 6.34: Crack path obtained with xFEM for coarse mesh - specimen 3.

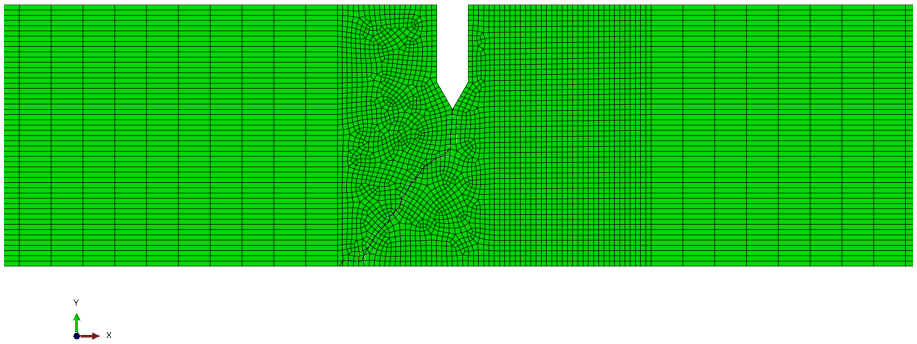


Figure 6.35: Crack path obtained with xFEM for fine mesh - specimen 3 .

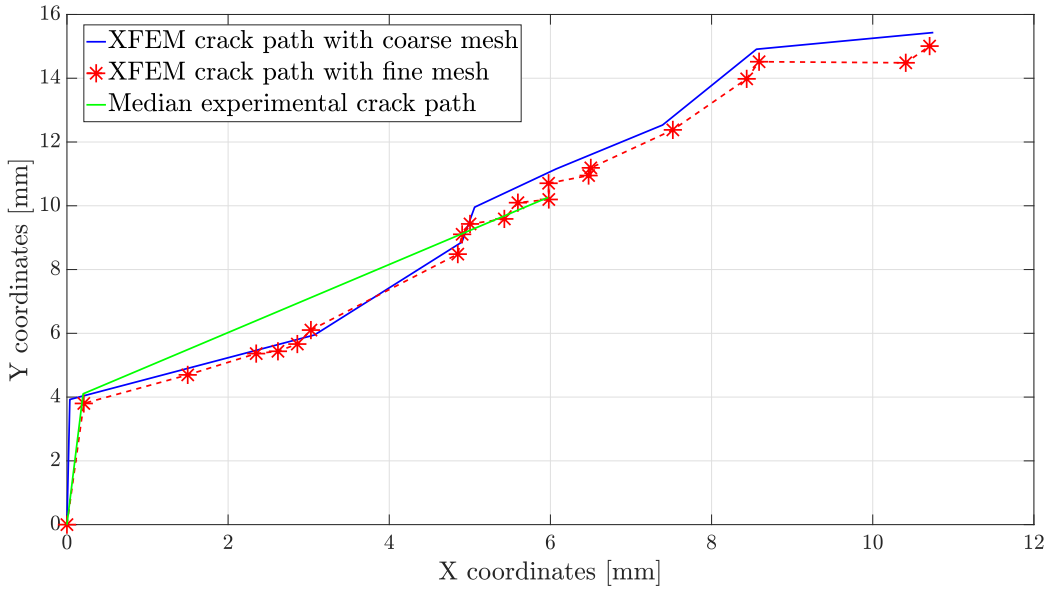


Figure 6.36: Comparison between crack path obtained with xFEM for fine mesh, coarse mesh and experimental crack path - specimen 3.

6.3.3 Discussion

As it can be seen, crack propagation was easier to enable in this situation when compared to the previous ones, as it was expected due to the higher mode I contribution and lower width.

The crack paths obtained by xFEM for a 1 mm mesh and a finer mesh are quite similar. The experimental crack path is a bit different from the xFEM ones, this could be due to reasons like not having an ideal photo quality or the error commited ploting the points using the plot digitizer.

6.4 Mixed mode I-II loading ($\beta = 70°$): Experimental set up and fatigue load calculation

Following the same reasoning, the set up chosen to enable $\beta = 70°$ ($\frac{K_I}{K_{II}}$=2.79) was $s_1 = 85$ mm, $s_2 = 15$ mm and $s_0 = 10$ mm (figure 6.37). Initially several attempts were made to

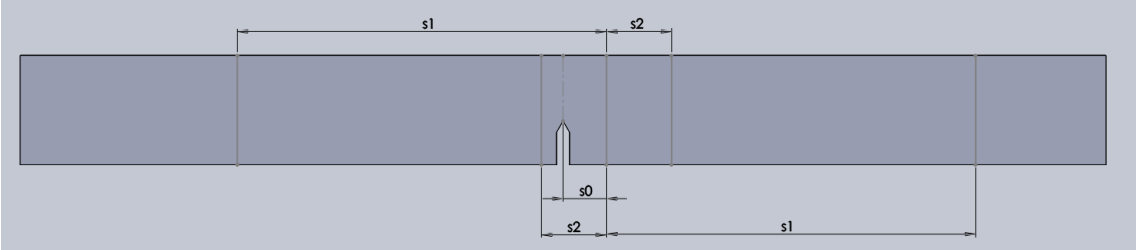


Figure 6.37: Single edge notch bending specimen 5 initial set up sketch.

enable crack growth, the values and respective equivalent SIF and used loads are presented in the table bellow,

Table 6.4: Data for the fatigue tests for specimen 5 under mixed mode I-II loading ($\beta = 70°$)

Width [mm]	P **[N]**	K_{eq} **MPa$\sqrt{\text{m}}$[1.20]**	ΔK_{eq} **MPa$\sqrt{\text{m}}$**	**No. of cycles**	**Obs.**
25	15600.0	20.0	18.0	36596	No growth
25	18200.0	23.4	21.0	36199	No growth
25	20800.0	26.7	24.1	357999	No growth
25	23000.0	29.5	26.6	241287	No growth

In section 7.2.4 it was stated that the set up used for mixed mode loading when $\beta = 13°$ (specimen 4) was wrong. It was also explained that the solution was simply turn the specimen upside down so that the side that contained the crack was under a tensile stress and not a compressive stress. This realization only came during this test ($\beta = 70°$). At the time of the specimen 4 test, the mistake went unnoticed for several reasons,

- The difference between total number of cycles for pure Mode II loading and mainly mode II loading ($\beta = 13°$) was not extremelly high (81417 cycles), and could be justifiable by experimental errors since guaranteeing that all the distances between the supports and loading points was difficult with the resources avaiable at the laboratory;
- The loads between theese first two tests also weren't very disporpotional;
- Crack growth was possible and this kind of test using asymmetric four-point bending is somewhat of a novelty;

For this test, by looking at 6.4 the total number off cycles adds up to 672081, reaching $\Delta K_{eq,Irwin} = 26.6$ MPa$\sqrt{\text{m}}$ that is the highest value in all the specimens that were tested beforehand (specimen 1 and 4), which didn't really make sense since this situation, theoretically, should be the easiest one to induce crack growth. By the reasons explained in section 7.2.4, crack growth and fatigue failure were being delayed due to crack closure. Nevertheless it is interesting to observe that crack closure was even greater in the situation

where the loading is primarily mode I loading ($\frac{K_I}{K_{II}} = 2.79$). This is probably explained by the fact that the bending moment at the crack plane is far superior in this situation than in the situation where $\frac{K_I}{K_{II}} = 0.23$ ($\beta = 13°$). For a situation where $P = 46000$ N, which corresponds to the load where crack growth was observed in specimen 4, using the simplified model created in subsection 7.1.1, the bending moment at the crack plain is -41400 N·mm, and for this situation where $P = 15000$ the bending moment is -105000 N·mm mm (254% bigger).

After this realization specimen 5 was turned upside down with the crack placed on the top side (6.38) and the test was restarted for a load of $P = 11500$ N equating to $\Delta K_{eq,Irwin} = 13.3$ MPa$\sqrt{\text{m}}$ and after only 9407 cycles fatigue failure occured.

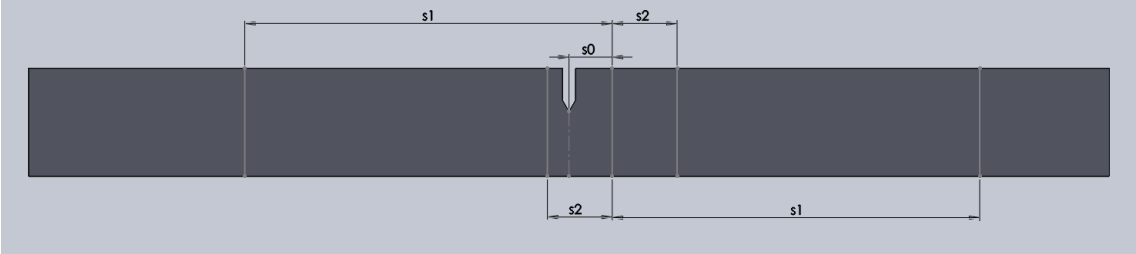


Figure 6.38: Single edge notch bending specimen 5 corrected set up sketch.

Table 6.5: Data for the fatigue test for specimen 5 under mixed mode I-II loading ($\beta = 70°$)

Width [mm]	P **[N]**	K_{eq} **MPa$\sqrt{\text{m}}$[1.20]**	ΔK_{eq} **MPa$\sqrt{\text{m}}$**	**No. of cycles**	**Obs.**
25	11500	14.8	13.3	9407	Growth

6.4.1 Shear force and bending moment diagrams

The shear force and bending moment are presented bellow for a load of $P = 11500$ N,

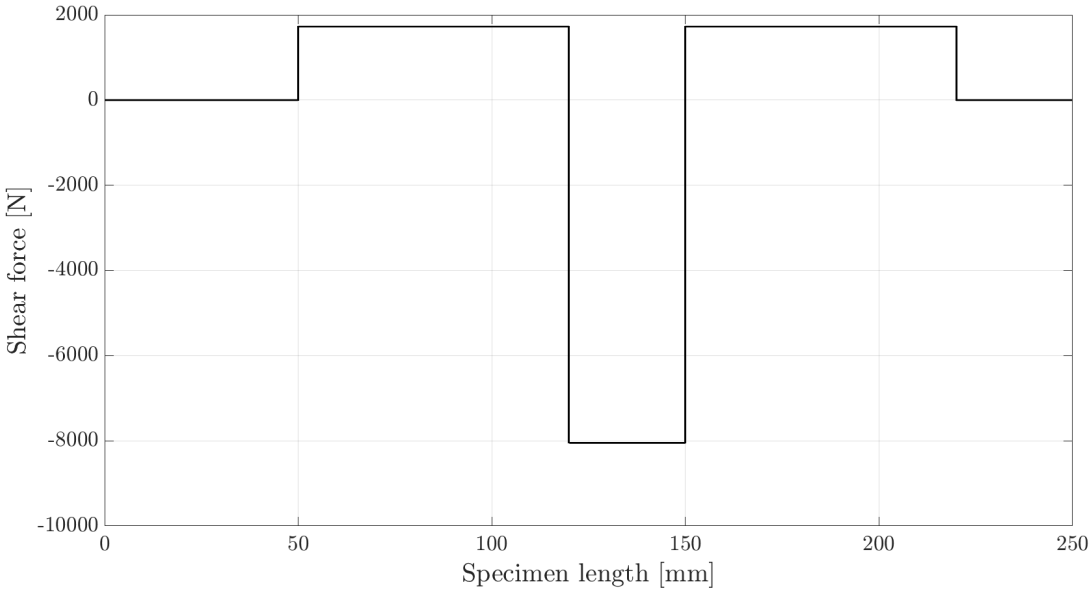


Figure 6.39: Shear force diagram for the experimental mixed mode loading I-II($\beta = 70°$, $P = 11500$ N

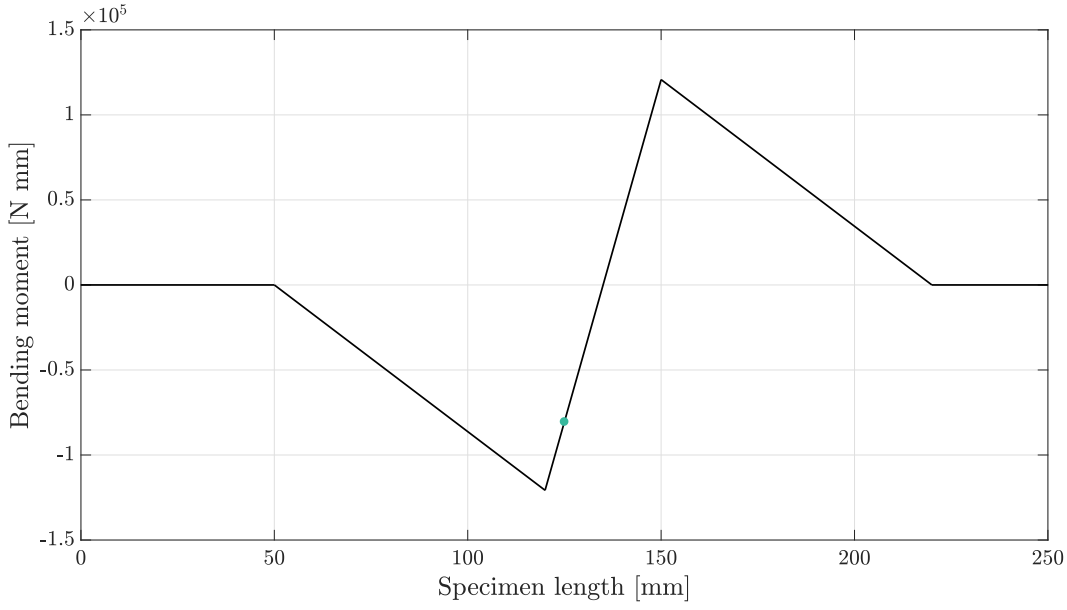


Figure 6.40: Bending moment diagram for the experimental mixed mode loading I-II($\beta = 70°$, $P = 11500$ N

Where the bending moment at the crack plane is -80500 N·mm.

6.4.2 Numerical model: Crack propagation path

The same methodology as in the previous subsections was used. Figure 6.41 used a mesh with 1 mm length elements (seed size 1) and figure 6.42 was built with a fine mesh using elements with 0.5 mm length (seed size 0.5).

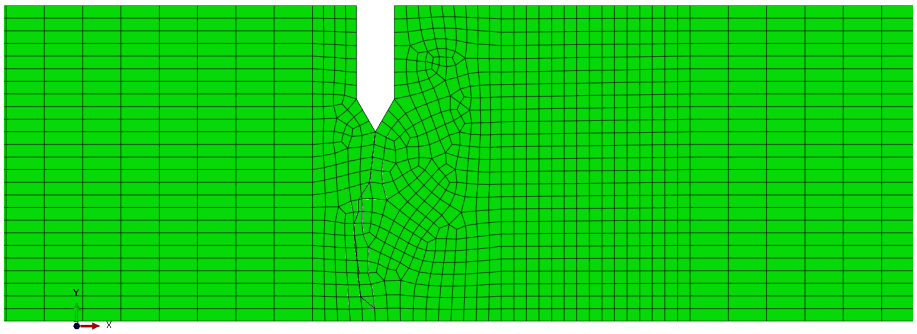


Figure 6.41: Crack path obtained with xFEM for coarse mesh - specimen 5 .

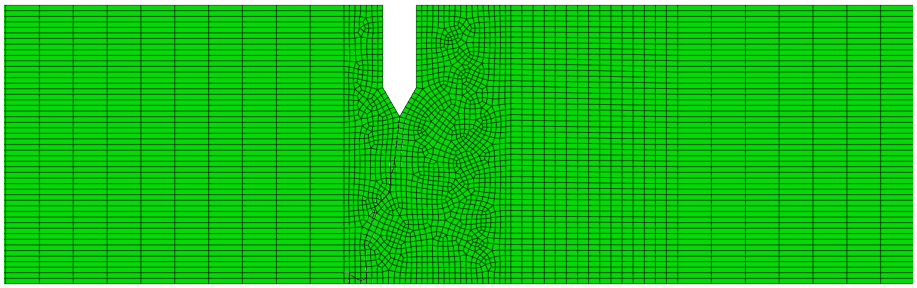


Figure 6.42: Crack path obtained with xFEM for fine mesh - specimen 5 .

The numerical results obtained were then compared with the experimental crack path,

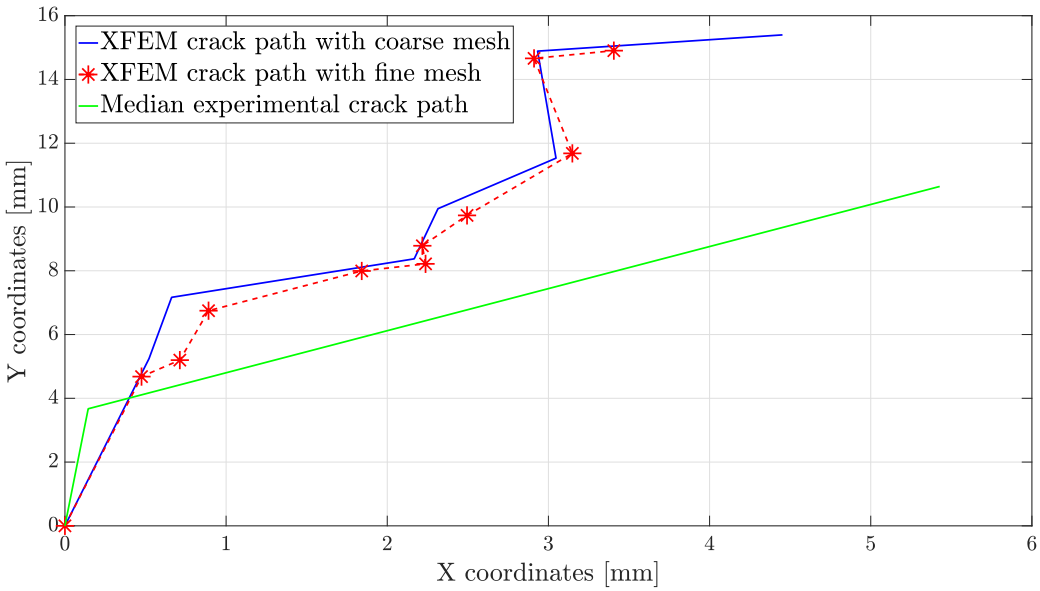


Figure 6.43: Crack path obtained with xFEM for fine mesh - specimen 5 .

6.4.3 Discussion

Once again, no big differences between the two xFEM models are noted. However the experimental crack path is different from ones obtained via ABAQUS.

6.5 Equivalent stress intensity factor determination

Most of the data avaiable for materials, including the one used in this work, is obtained for pure mode I loading which can lead to imprecise results of life prediction for an component.

In the present section using the data obtained in the experimental results, that being the number of cycles (N) and photographs taken along the tests, together with numerical results provided by finite element models, a comparison between the NASGRO material curve and Paris law equation was made.

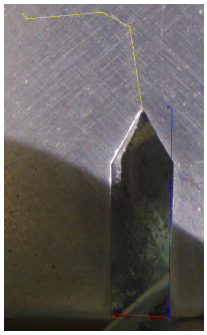
By post processing of the images aquired the crack path geometry can be recreated in a finite element model and through that model the stress intensity factors can be determined for each crack tip. Given that for each photograph the number of cycles was registered, it is possible to determine the crack growth between a range of cycles (da/dN).

That being said from all the photographs taken a few were selected based on quality and crack growth. The situations for mixed mode loading for $\frac{K_I}{K_{II}} = 0.23$ ($\beta = 13°$) and $\frac{K_I}{K_{II}} = 2.79$ ($\beta = 70°$) using speciments 4 and 5 respectivly were not modeled. The crack in specimen 4, as it was stated before, was under compression which was not the goal this work pursued. Specimen 5 broke without the possibility of making a photographic log.

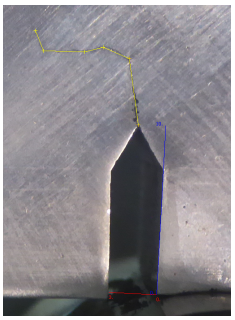
The cases modeled were for pure mode II and mixed mode loading with $\frac{K_I}{K_{II}} = 1.10$.

Starting with specimen 1 that was under pure mode II loading, the higher quality pictures are presented in figures 6.44a, 6.44b, 6.44c and 6.44d. The tool used to process the images was a plot digitizer in which, by hand, the crack path was traced allowing the acquisition of its coordinates x and y. The graph of the coordinates aquired for this specimen is presented in figure 6.45.

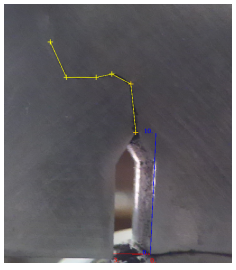
An approximation of the crack geometry was created on a bidimensional finite element model using ABAQUS and based on that information for each crack tip three values of the SIFs were obtained using the J integral and VCCT techniques. Crack length for each increment is obtained by using the norm of the x and y coordinates ($\sqrt{x^2 + y^2}$) between



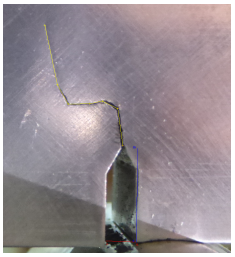
(a) Photo 1 - specimen 1



(b) Photo 2 - specimen 1



(c) Photo 3 - specimen 1



(d) Photo 4 - specimen 1

Figure 6.44: Set of chosen pictures for specimen 1

each crack tip. Figures 6.46, 6.47, 6.48 presented bellow show the model at the instance photograph 4 was taken, the rest can be found in the annex. The crack was modeled from the end until the beggining (starting in the last photo and finishing on the first).

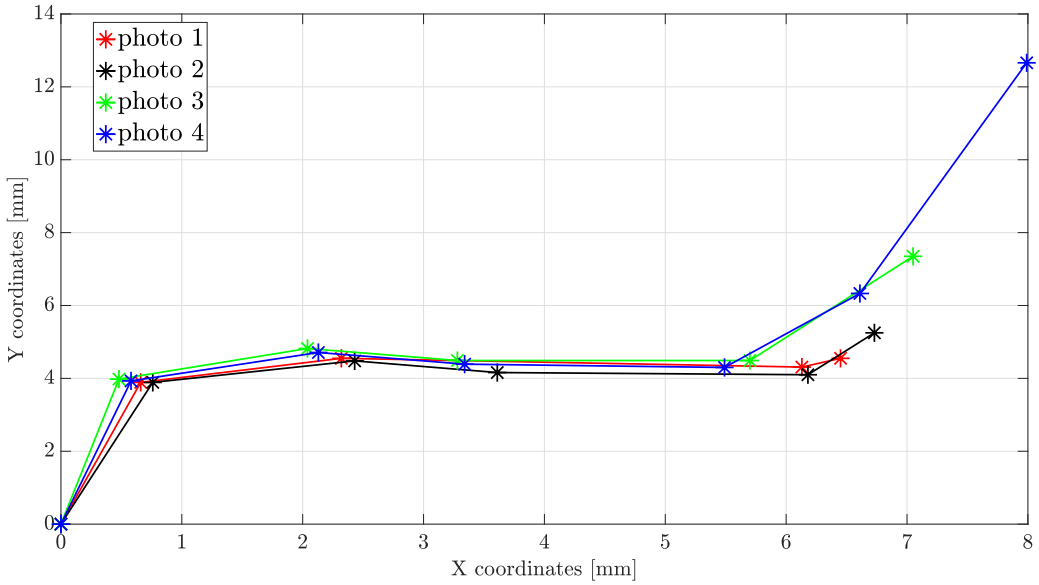


Figure 6.45: Plot of the coordinates obtained from image post processing - specimen 1

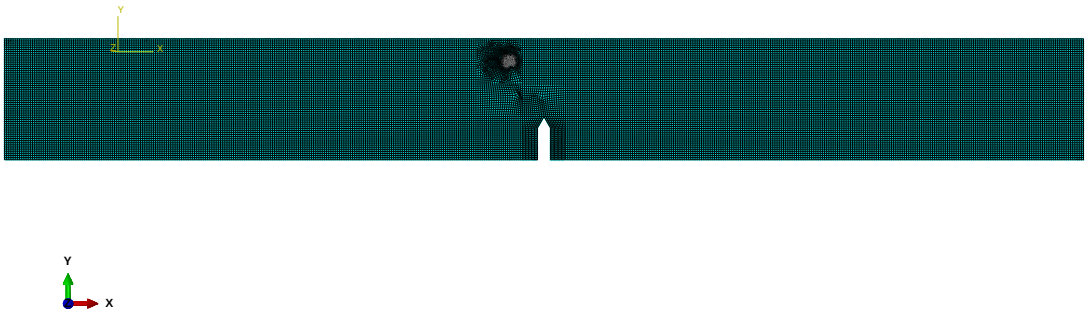


Figure 6.46: Mesh with 32227 linear quadrilateral elements of type CPS4 for specimen 1 - Photo 4

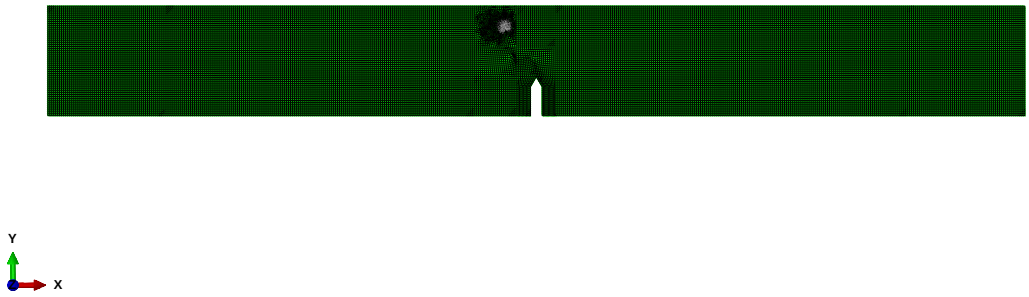


Figure 6.47: Undeformed shape for specimen 1 - Photo 4

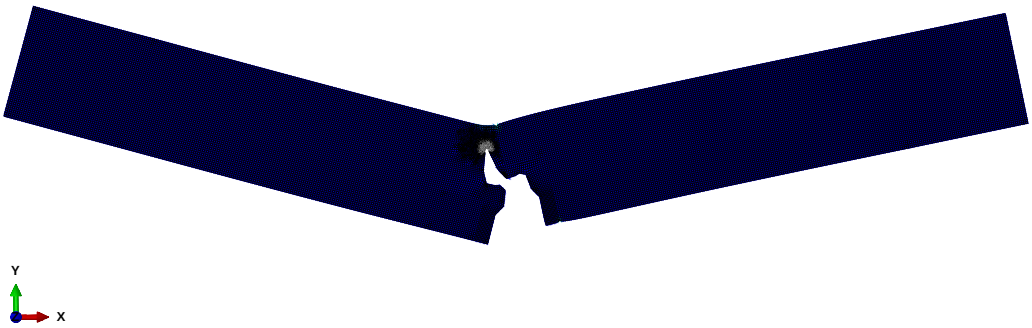


Figure 6.48: Deformed shape for specimen 1 - Photo 4

In order to calculate the SIFs using the two techniques a square partition was created at the crack tip (figure 6.49).

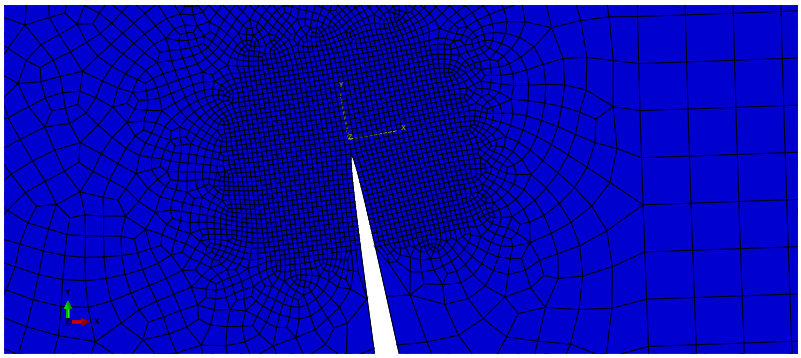


Figure 6.49: Partition at crack tip specimen 1 - Photo 4

Pictures 6.50 and 6.51 show the square partition with the J integral contours used (10) and the free body cut and coordinate system used in the VCCT, respectively.

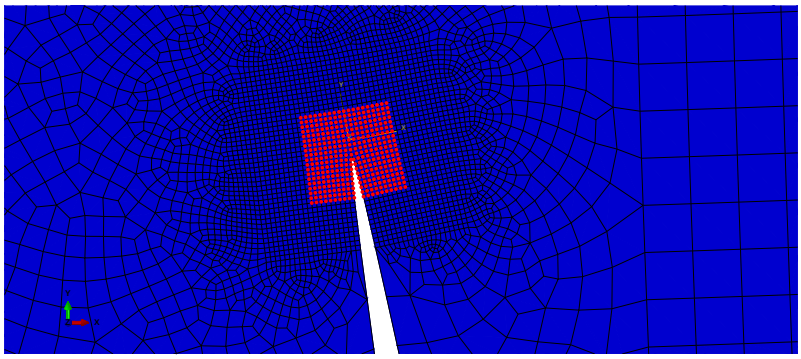


Figure 6.50: Mesh contours used for the J integral

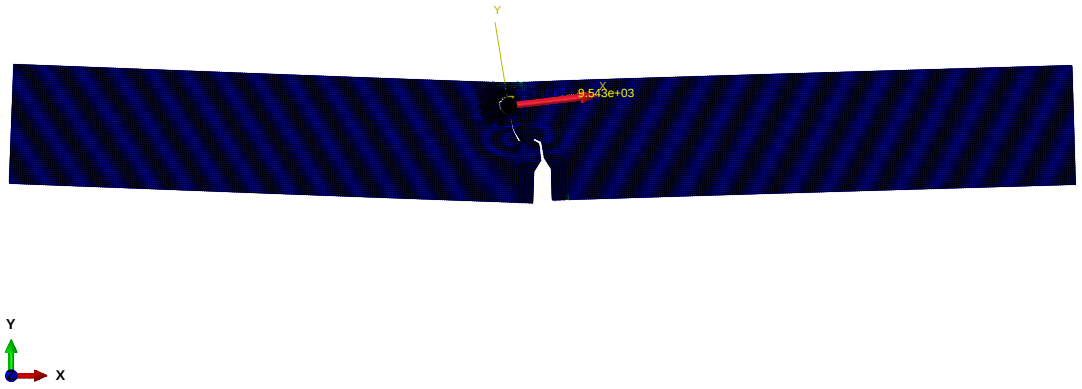


Figure 6.51: Free body cut and coordinate system used for the VCCT

For the J integral technique the mode I and mode II SIFs were obtained for three points: a point before the crack, at the crack and after the crack being that the median

value of all three was used to describe the respective stress intensity factors.

The stress intensity factors obtained by the J integral and VCCT are shown in tables 6.6, 6.7 and 6.8.

Table 6.6: Mode I SIFs for specimen 1 - J integral

	J integral			
	K_I **before crack**	K_I **crack**	K_I **after crack**	K_I **mean**
		MPa$\sqrt{\text{mm}}$		
Pre-crack	-	172.7	-	172.7
Photo 1	709.6	738.2	763.9	737.2
Photo 2	775.6	825.1	876.2	825.6
Photo 3	972.3	1053.0	1139.0	1054.8
Photo 4	2733.0	3084.0	3583.0	3133.3

Table 6.7: Mode II SIFs for specimen 1 - J integral

	J integral			
	K_{II} **before crack**	K_{II} **crack**	K_{II} **after crack**	K_{II} **mean**
		MPa$\sqrt{\text{mm}}$		
Pre-crack	-	504.3	-	504.3
Photo 1	5.2	9.9	22.1	12.4
Photo 2	28.1	47.2	64.9	46.7
Photo 3	51.3	83.3	60.1	64.9
Photo 4	122.2	168.1	228.2	172.8

Table 6.8: Mode I and Mode II equivalent SIFs for specimen 1

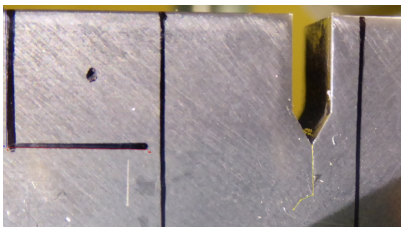
	VCCT				**J integral**	
	K_I	K_{II}	$K_{eq,Irwin}$		$K_{eq,Irwin}$	
		MPa$\sqrt{\text{mm}}$		MPa$\sqrt{\text{m}}$	MPa$\sqrt{\text{mm}}$	MPa$\sqrt{\text{m}}$
Pre-crack	172.3	512.9	541.1	17.1	533.1	16.9
Photo1	738.6	9.6	738.7	23.4	737.3	23.3
Photo2	834.6	51.0	836.1	26.4	827.0	26.2
Photo3	1076.0	83.7	1079.2	34.1	1056.8	33.4
Photo4	3091.5	176.2	3096.5	97.9	3138.1	99.2

Since the values from each method are very similiar the following calculations will be done using the VCCT values. Through the created finite element model, crack growth between pictures (da) was measured and presented in table 6.9 alongside with the corresponding equivalent SIFs ($K_{eq,Irwin}$) and number of cycles dN.

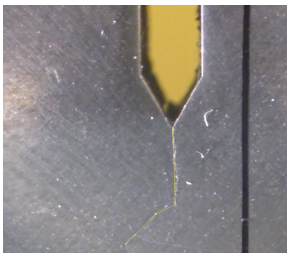
The exact same methodology was used for specimen 3. The chosen pictures for this specimen are presented bellow (figure 6.52), along with the plot obtained by image post processing (figure 6.53).

Table 6.9: Values of the equivalent SIFs and the correspondent $\frac{da}{dN}$ for specimen 1

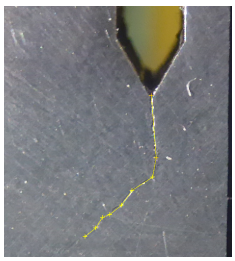
	da mm	dN cycle	$\frac{da}{dN}$ mm · cycle $^{-1}$	$\Delta K_{eq,Irwin}$ MPa$\sqrt{\text{mm}}$	MPa$\sqrt{\text{m}}$
Pre-crack to photo 1	5.9	39689	1.5E-04	487	15.4
Photo 1 to photo 2	0.9	14400	5.9E-05	664.8	21.0
Photo 2 to photo 3	1.9	1858	1.0E-03	752.5	23.8
Photo 3 to photo 4	5.4	528	1.0E-02	971.3	30.7



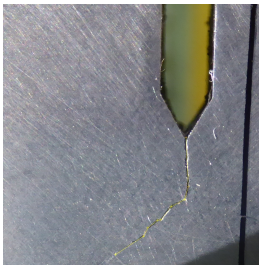
(a) Photo 1 - specimen 3



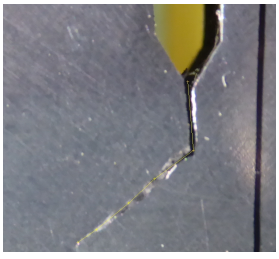
(b) Photo 2 - specimen 3



(c) Photo 3 - specimen 3



(d) Photo 4 - specimen 3



(e) Photo 5 - specimen 3

Figure 6.52: Set of chosen pictures for specimen 3

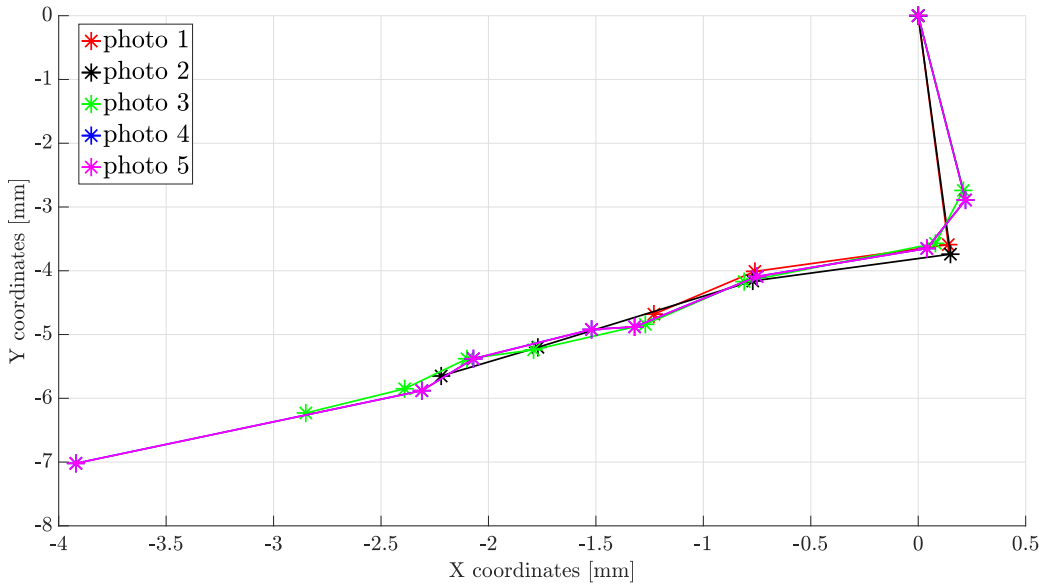


Figure 6.53: Plot of the coordinates obtained from image post processing - specimen 3

Figures 6.54, 6.55, 6.56 show the model at the instance photograph 5 was taken, the rest can be found in the annex. Like the previous model, the crack was modeled from the end until the beggining (last photo to the first).

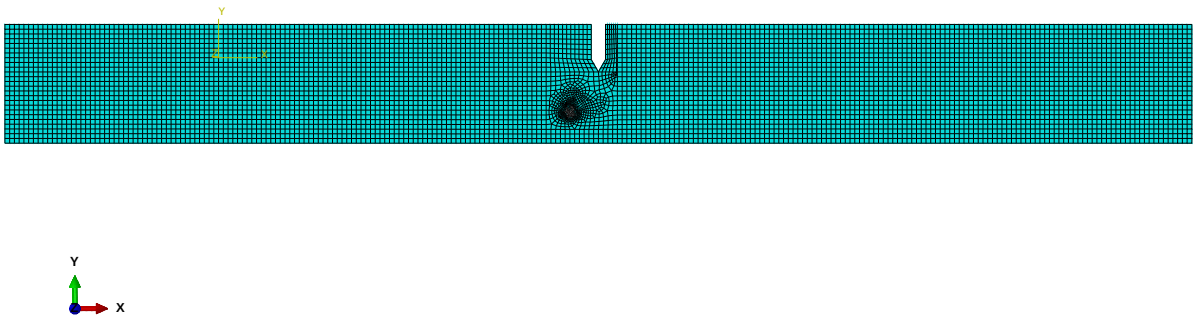


Figure 6.54: Mesh with 7215 linear quadrilateral elements of type CPS4 for specimen 3 - Photo 5

The stress intensity factors obtained by the J integral and VCCT are shown in tables 6.10, 6.11 and 6.12.

Table 6.10: Mode I SIFs specimen 3 - J integral

	J integral			
	K_I **before crack**	K_I **crack**	K_I **after crack**	K_I **mean**
		MPa$\sqrt{\text{mm}}$		
Pre-crack	-	343.3	-	343.3
Photo1	555.4	572.8	590.9	573.0
Photo2	807.6	839.9	841.6	829.7
Photo3	875.7	915.6	1021.0	937.4
Photo4	1075.0	1164.0	1262.0	1167.0
Photo5	1564.0	1696.0	1843.0	1701.0

Table 6.11: Mode II SIFs for specimen 3 - J integral

	J integral			
	K_{II} **before crack**	K_{II} **crack**	K_{II} **after crack**	K_{II} **mean**
		MPa$\sqrt{\text{mm}}$		
Pre-crack	-	260.6	-	260.6
Photo 1	99.1	108.8	120.3	109.4
Photo 2	42.0	38.0	33.4	37.8
Photo 3	110.8	181.5	98.2	130.2
Photo 4	129.1	156.8	188.4	158.1
Photo5	362.8	414.3	473.9	417

Table 6.12: Mode I and Mode II equivalent SIFs for specimen 3

	VCCT				**J integral**	
	K_I	K_{II}	$K_{eq,Irwin}$		$K_{eq,Irwin}$	
		MPa$\sqrt{\text{mm}}$		MPa$\sqrt{\text{m}}$	MPa$\sqrt{\text{mm}}$	MPa$\sqrt{\text{m}}$
Pre-crack	344.7	258.9	431.2	13.6	431	13.6
Photo 1	574.9	100.5	583.6	18.5	583.4	18.4
Photo 2	840.0	50.6	841.5	26.6	830.0	26.3
Photo 3	919.4	183.5	937.5	29.6	946.4	29.9
Photo 4	1169.8	132.3	1177.2	37.2	1177.7	37.2
Photo 5	1704.9	404.0	1752.1	55.4	1751.4	55.4

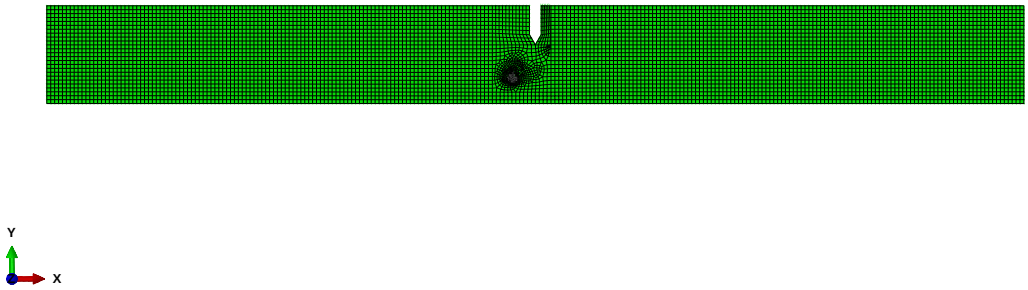


Figure 6.55: Undeformed shape for specimen 3 - Photo 5

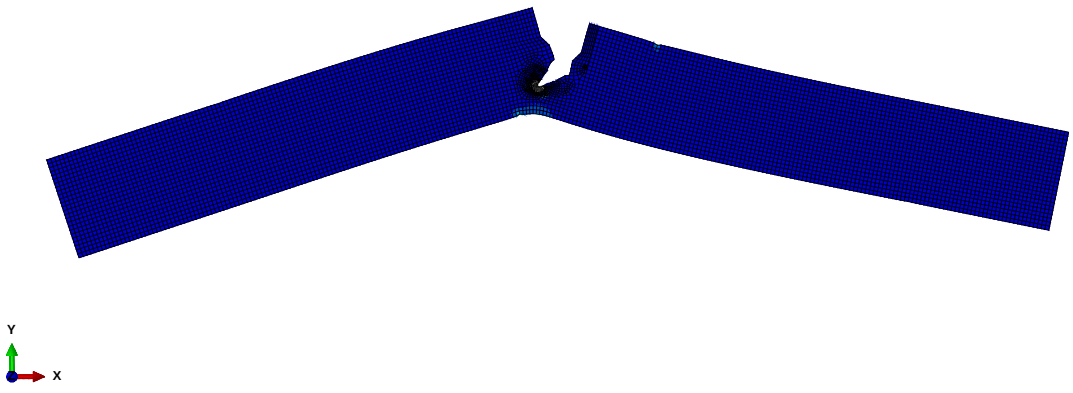


Figure 6.56: Deformed shape for specimen 3 - Photo 5

Since the values for the SIFs obtained through the J integral and VCCT are very similar, the following calculations will be done using the VCCT values. Like in the previous case, using the created finite element model, crack growth between pictures (da) was measured and presented in table 6.13 allongside the corresponding equivalent SIFs ($K_{eq,Irwin}$) and number of cycles dN.

Table 6.13: Values of the equivalent SIFs and the correspondent $\frac{da}{dN}$ for specimen 3

	da	dN	$\frac{da}{dN}$	$\Delta K_{eq,Irwin}$	
	mm	cycle	mm · cycle $^{-1}$	MPa$\sqrt{\text{mm}}$	MPa$\sqrt{\text{m}}$
Precrack to photo 1	0.97	10000	9.7E-05	388.0	12.3
Photo 1 to Photo 2	2.1	1500	1.4E-03	525.2	16.6
Photo 2 to Photo 3	0.9	2122	4.1E-04	757.4	24.0
Photo 3 to Photo 4	1.3	218	6.0E-03	843.8	26.7
Photo 4 to Photo 5	2.4	128	1.9E-02	1059.5	33.5

Using the information gathered in tables 6.9 and 6.13 the points of the values of da/dN as function of $\Delta K_{eq,Irwin}$ were ploted in the NASGRO material fitting curve ($R = 0.1$), along with the Paris law fitting curve which, according to [31] is as following,

$$\frac{da}{dN} = 85.409 \cdot 10^{-15} \Delta K^{3.7554} \tag{6.22}$$

A non-linear regression was also done using the obtained data, being that the second point from specimen 1 was not included in it due to being an outlyer relativilly to the rest of the data.

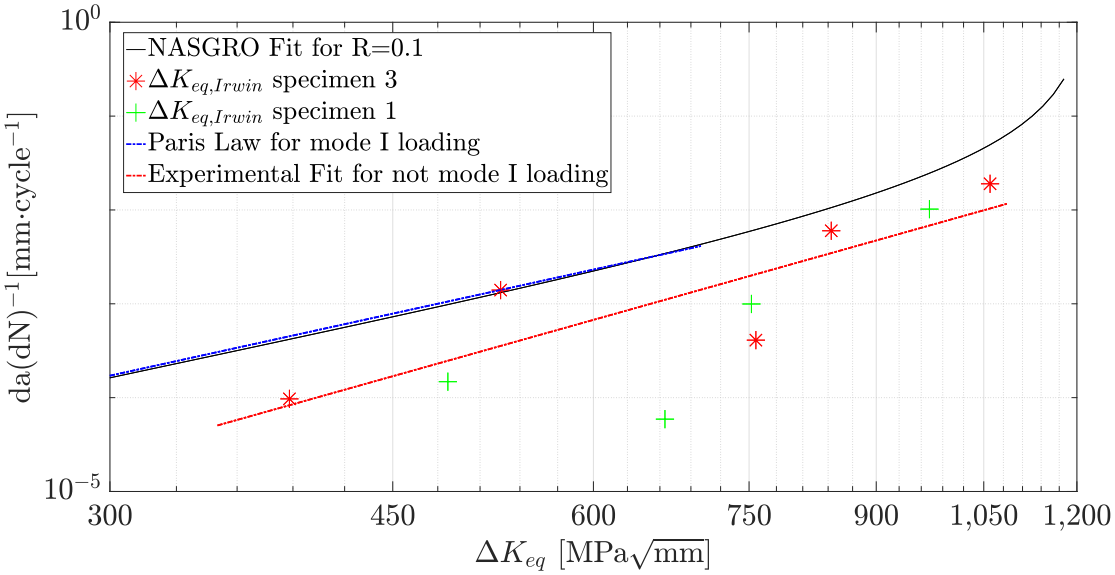


Figure 6.57: Comparison between NASGRO material fitting curve, Paris law and points obtained from the experimental procedures post processing

From the comparison made on figure 6.57, where the coefficient of determination (R^2) for the non-linear regression was 0.77, it can be said this experimental approach presented difficulties and had some limitations,

- Despite surface polishing after specimen pre-cracking, the crack was still hard to see and record.
- The procedure was done with a regular camera that was not on a fixed position throughout all the duration of the tests, making it harder to focus multiple points of the specimens at close range and causing variations in the photo angles.
- The usage of the image digitizer introduced measurement errors, since even in the higher quality photos it was difficult seeing, marking and tracking the crack tip and path with precision. In figure 6.57 the two points that are the farthest from the Paris law line are the ones with the smallest crack increment ($da = 0.9$ mm). It is reasonable to say that, since the image post processing software requires the points to be marked by hand, the smaller the measurement the more noticible the error commited is.
- Some cycle ranges dN were harder to pinpoint. At times a range was noted but no photograph was taken and vice-versa.

Nevertheless, it can be said that for specimen 3 the crack propagation in mixed mode loading had a similar behaviour to mode I crack propagation in 2 of the 5 ploted points, which are close to the NASGRO fitting curve, being that one is overlaped with it. As for specimen 1, under pure mode II loading, it is reasonable to say that crack propagation was delayed, probably due to crack closure.

The reference [42] states that crack closure level increases for mixed mode loading conditions in comparison to mode I loading. In this article the mixed mode loading experiments were done using a CTS specimen with an loading device like the one presented in figure 1.15b, and it is said that with the increase of mode mixicity (increase of α) there is an increase in the crack closure level. In figure 6.58 the authors da/dN *vs* ΔK is presented, and it can be seen that for higher mode mixicity the crack growth rates that were measured under mixed mode cannot be correlated further with crack growth obtained under mode I loading [42].

It should be noted that the equivalent SIF used by [42] is,

$$K_v = \frac{K_I}{2} + \frac{1}{2}\sqrt{K_I^2 + 6K_{II}^2} \tag{6.23}$$

similar to the equivalent SIF proposed by Richard in 1.23.

This, combined with all the experimental set up instrumentation limitations and user induced errors (image digitizer) can help explain the results obtained by this study. It is however noted that other authors also found some difference in the da/dN *vs* ΔK_{eq} or *vs* ΔK_I relationships. A small difference was found by Ferreira [31], but his work concerned mixed-mode situations where mode I was predominant. Larger differences were found e.g. by Kim and Kim [43] or by Peixoto and de Castro [44], albeit studying other alloys.

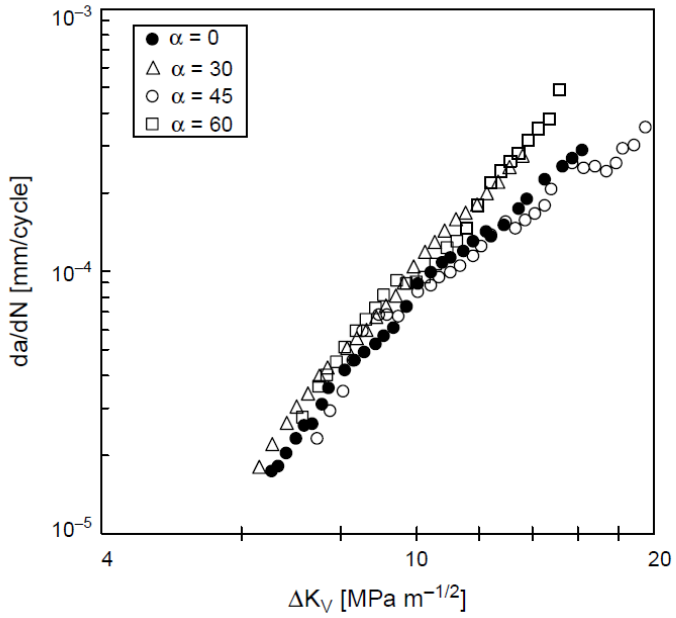


Figure 6.58: Crack growth rate *vs* ΔK_v, [42].

Chapter 7

Conclusions

The main conclusions that were taken from this work relatively to the experimental and numerical procedures are,

- Using the asymmetrical four-point bending set up, in order to estimate the SIFs at the crack tip through the analitical equations presented in chapter 4, one has to make sure the crack plane is located in the region where the shear force is maximum. Close attention to where the pre-cracked specimen is facing should be paid, because it is not evident if the pre-cracked plane is under compression or under tension during the fatigue tests, since it depends on the supports positioning.
- The asymmetrical four-point bending set up used is extremelly sensitive to the distances between the supports and loads, so precise and adequate instrumentation should be used while assembling the test in order to achieve accurate results.
- The observation and record of the experimental fatigue tests should be done thoroughly, using a high quality camera allowing good quality footage of crack growth and facilitating image post-processing.
- The results obtained from the finite element models created throughout this work showed good agreement with analytical predictions, when such were possible, demonstrating that the finite element method is an excellent tool to estimate the stress field at the crack tip.
- The crack paths obtained using the extended finite element method did not show good agreement with the paths obtained experimentally, which doesn't mean the numerical model results are wrong, it is more likely that the data input on the model was not the most accurate.
- The fatigue crack growth behaviour results, expressed as a function of ΔK_{eq}, for mixed mode I-II and mode II loading were different from the mode I data from the NASGRO database and Paris law equation for the studied material, probably due to the accumulation of experimental and/or post-processing errors (cycle and crack growth recording, manual image processing), roughness-induced crack closure and thus friction between crack surfaces. Nevertheless, several authors also found differences in the da/dN *vs* ΔK_{eq} for various mode mixicities when compared to the da/dN *vs* ΔK_I.
- The asymmetrical four-point bending set up seems to provide a simple way of testing material fatigue properties for mixed mode and mode II loading.

References

[1] H. Westergaard, "Bearing pressures and cracks," *Journal of Applied Mechanics*, vol. 18, pp. 49–53, June 1939.

[2] G. R. Irwin, "Analysis of stresses and strains near the end of a crack traversing a plate," *Journal of Applied Mechanics*, vol. 24, no. 3, pp. 361–364, 1957.

[3] I.N. Sneddon, "The distribution of stress in the neighbourhood of a crack in an elastic solid," in *Proceedings of the Royal Society of London A: Mathematical, Physical and Engineering Sciences*, vol. 187, pp. 229–260, 1946.

[4] M.L. Williams, "On the stress distribution at the base of a stationary crack," *Journal of Applied Mechanics*, vol. 24, pp. 109–114, March 1957.

[5] T.L. Anderson, *Fracture Mechanics*. Taylor & Francis Group, LLC, third ed., 2005.

[6] David Broek, *Elementary Engineering Fracture Mechanics*. Martinus Nijhoff Publishers, Fourth revised ed., 1986.

[7] Carlos A.G. de Moura Branco, *Mecânica dos Materiais*. Fundação Calouste Gulbenkian, fifth ed., 2011.

[8] C. Moura Branco, A. Augusto Fernandes, Paulo M.S. Tavares de Castro, *Fadiga de Estruturas Soldadas*. Fundação Calouste Gulbenkian, second ed., 1999.

[9] M. F. Kanninen and C. L. Popelar, *Advanced Fracture Mechanics*. Oxford University Press, 1985.

[10] G. Fajdiga and B. Zafošnik, "Determining a kink angle of a crack in mixed mode fracture using maximum energy release rate, SED and MTS criteria," *Journal of Multidisciplinary Engineering Science and Technology*, vol. 2, pp. 356–362, 2015.

[11] H. Richard, M. Fulland, and M. Sander, "Theoretical crack path prediction," *Fatigue & Fracture of Engineering Materials & Structures*, vol. 28, no. 1-2, pp. 3–12, 2005.

[12] H. A. Richard and M. Sander, *Fatigue Crack Growth: Detect-Assess-Avoid*. Springer, 2016.

[13] K. Tanaka, "Fatigue crack propagation from a crack inclined to the cyclic tensile axis," *Engineering Fracture Mechanics*, vol. 6, no. 3, pp. 493 – 507, 1974.

[14] L. Pook, ""Mixed-mode fatigue crack growth thresholds: A personal historical review of work at the National Engineering Laboratory, 1975–1989 https://doi.org/10.1016/j.engfracmech.2017.10.028"," *Engineering Fracture Mechanics*, 2017.

[15] C.H. Wang, *Introduction to Fracture Mechanics*. DSTO Aeronautical and Maritime Research Laboratory Melbourne, Australia, 1996.

[16] J.G. Williams, *Stress Analysis of Polymers*. Ellis Horwood, second ed., 1980.

[17] P. M. S. T. de Castro, "Notas sobre a análise linear elástica do estado de tensão e deformação de sólidos contendo fendas," 2017.

[18] H. Richard, "Specimens for investigating biaxial fracture and fatigue processes," in *Biaxial and Multiaxial Fatigue*, pp. 217–229, Mechanical Engineering Publications, 1989.

[19] J. Rice, "A path independent integral and the approximate analysis of strain concentration by notches and cracks," *Journal of Applied Mechanics*, pp. 379–386, 1968.

[20] R. Krueger, "Virtual crack closure technique: history, approach, and applications," *Applied Mechanics Reviews*, vol. 57, no. 2, pp. 109–143, 2004.

[21] H. L. C. Wang, Z.M. Zhu, "On the i-ii mixed mode fracture of granite using four-point bend specimen," *Fatigue & Fracture of Engineering Materials & Structures*, vol. 39, no. 1-2, pp. 1193–1203, 2006.

[22] M. He and J. Hutchinson, "Asymmetric four-point crack specimen," *Journal of Applied Mechanics*, vol. 67, no. 1, pp. 207–209, 2000.

[23] M. R. Ayatollahi and M. R. M. Aliha, "On the use of an anti-symmetric four-point bend specimen for mode ii fracture experiments," *Fatigue & Fracture of Engineering Materials & Structures*, vol. 361, no. 1, pp. 898–907, 2011.

[24] M. Razavi, M. Aliha, and F. Berto, "Application of an average strain energy density criterion to obtain the mixed mode fracture load of granite rock tested with the cracked asymmetric four-point bend specimens," *Theoretical and Applied Fracture Mechanics*, July 2017.

[25] P. Moreira, A. Jesus, A. Ribeiro, and P. Castro, "Fatigue Crack Growth Behaviour of the Friction Stir Welded 6082-T6 Aluminium Alloy," *Mecânica Experimental*, vol. 16, pp. 99–106, 2008.

[26] P. Moreira, T. Santos, S. Tavares, V. Richter-Trummer, P. Vilaça, and P. de Castro, "Mechanical and metallurgical characterization of friction stir welding joints of AA6061-T6 with AA6082-T6," *Materials & Design*, vol. 30, no. 1, pp. 180–187, 2009.

[27] D. Liu, H. Atkinson, P. Kapranos, W. Jirattiticharoean, and H. Jones, "Microstructural evolution and tensile mechanical properties of thixoformed high performance aluminium alloys," *Materials Science and Engineering-A*, vol. 361, no. 1, pp. 213–224, 2003.

[28] B. S. Institution, "Guide to methods for assessing the acceptability of flaws in metallic structures," *BS*, 7910, 2005.

[29] C.M. Wai, *Mode I and mixed-mode (I+II) fatigue crack growth threshold of aluminium alloy 6061 defined under four point bend loading conditions*. Universiti Teknikal Malaysia Melaka, 2011.

[30] J. A. Correia, A. M. D. Jesus, A. S. Alves, G. Lesiuk, P. J. Tavares, and P. M. Moreira, "Fatigue crack growth behaviour of the 6082-T6 aluminium using CT specimens with distinct notches," *Procedia Structural Integrity*, vol. 2, no. Supplement C, pp. 3272 – 3279, 2016. 21st European Conference on Fracture, ECF21, 20-24 June 2016, Catania, Italy.

[31] M. A. C. Ferreira, "Mixed mode crack propagation: Numerical and experimental study," master thesis, Faculade de Engenharia da Universidade do Porto, 2107.

[32] NASA, *Fracture Mechanics and Fatigue Crack Growth Analysis Software*, version 6.1 final ed., July 2010.

[33] Albertino J.C. Arteiro and Paulo M.S. Tavares de Castro, *Mecânica da Fratura e Fadiga: Exemplos de cálculo e aplicação*. FEUP edições, first ed., 2014.

[34] M. H. Aliabadi and M. H. López, *Database of stress intensity factors*. Computational Mechanics Publications, 1996.

[35] P. C. M. Azevedo, "A numerical and experimental analysis of fatigue and fracture mechanics problems," master thesis, Faculade de Engenharia da Universidade do Porto, 2008.

[36] B. S. Institution, "D 19:Draft for development," *Methods for crack opening displacement (COD) testing*, 1972.

[37] ASTM, "E399 Standard Method of Test for Plane Strain Fracture Toughness of Metallic Materials," *ASTM International*, 2013.

[38] ASTM, "E647 Standard test method for measurement of fatigue crack growth rates," *Annual Book of ASTM Standards, Section Three: Metals Test Methods and Analytical Procedures*, vol. 3, pp. 628–670, 2002.

[39] ISO, "12135 Metallic materials–Unified method of test for the determination of quasistatic fracture toughness," *International Organization for Standardization, Geneva*, 2016.

[40] ISO, "12108 Metallic Material—Fatigue Testing—Fatigue Crack Growth Method," *International Organization for Standardization, Geneva*, 2002.

[41] L. Gicquel, "Cracked beam subjected to asymmetric four-point bending," tech. rep., Faculdade de Engenharia da Universidade do Porto, July 2017.

[42] L. Borrego, F. Antunes, J. Costa, and J. Ferreira, "Mixed-mode fatigue crack growth behaviour in aluminium alloy," *International Journal of Fatigue*, vol. 28, no. 5-6, pp. 618–626, 2006.

[43] J.-K. Kim and C.-S. Kim, "Fatigue crack growth behavior of rail steel under mode I and mixed mode loadings," *Materials Science and Engineering: A*, vol. 338, no. 1-2, pp. 191–201, 2002.

[44] D. F. Peixoto and P. M. de Castro, "Fatigue crack growth of a railway wheel," *Engineering Failure Analysis*, vol. 82, pp. 420–434, 2017.

[45] M. Aliha, M. R. Ayatollahi, and B. Kharazi, "Numerical and experimental investigations of mixed mode fracture in granite using four-point-bend specimen," *Damage and Fracture Mechanics. Failure Analysis of Engineering Materials and Structures*, pp. 275–283, August 2009.

[46] P. Moreira, A. de Jesus, A. Ribeiro, and P. de Castro, "Fatigue crack growth in friction stir welds of 6082-T6 and 6061-T6 aluminium alloys: A comparison," *Theoretical and Applied Fracture Mechanics*, vol. 50, no. 2, pp. 81 – 91, 2008.

[47] A. A. Rubinstein, "Mechanics of the crack path formation," *International Journal of Fracture*, vol. 47, no. 4, pp. 291–305, 1991.

[48] E. Hedayati and M. Vahedi, "Using extended finite element method for computation of the stress intensity factor, crack growth simulation and predicting fatigue crack growth in a slant-cracked plate of 6061-T651 aluminum," *World Journal of Mechanics*, vol. 2014, 2014.

[49] Dassault Systèmes, "Abaqus documentation," *Dassault Systèmes Simulia Corporation*, 2017.

[50] P. C. Paris and F. Erdogan, "A critical analysis of crack propagation laws," *Journal of Basic Engineering*, vol. 85, no. 4, pp. 528–533, 1963.

[51] J. J. Newman, "A crack opening stress equation for fatigue crack growth," *International Journal of Fracture*, vol. 24, no. 4, pp. R131–R135, 1984.

[52] H. A. Richard and M. Sander, *Fatigue Crack Growth*. Springer, 2016.

[53] H. Richard, W. Linnig, and K. Henn, "Fatigue crack propagation under combined loading," *Forensic Engineering*, vol. 3, no. 2-3, pp. 99–109, 1991.

Annex A

Pre study case 1 ABAQUS models

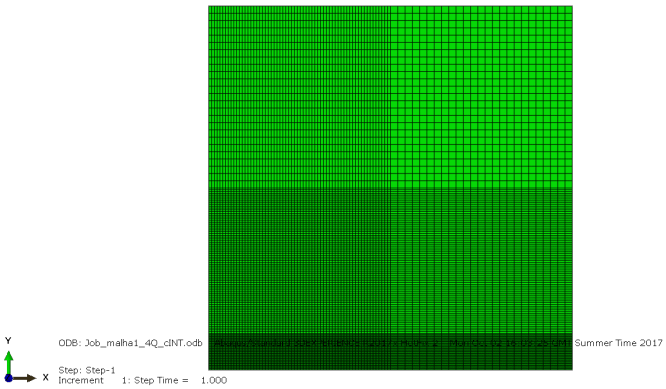


Figure A.1: Mesh 1 for 1/4 plate - CPS4R

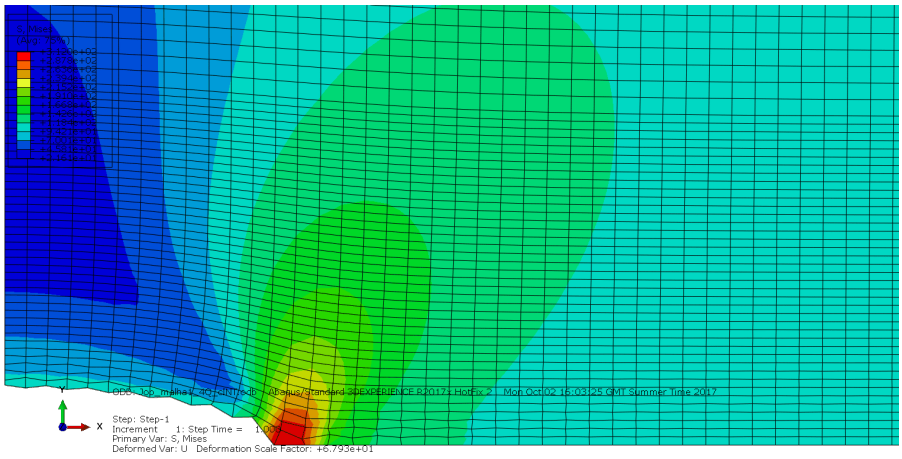


Figure A.2: Mesh 1 for 1/4 plate (CPS4R) - von Mises stress

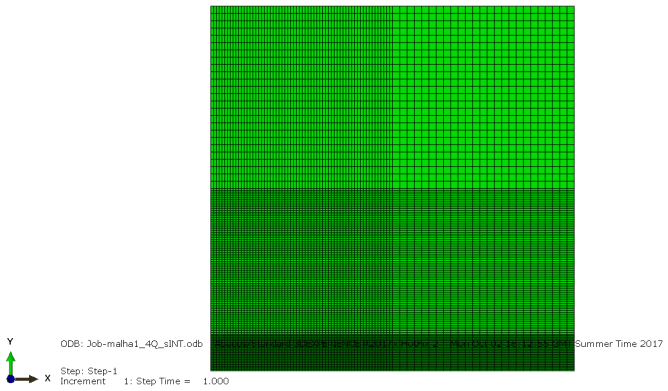


Figure A.3: Mesh 1 for 1/4 plate - CPS4

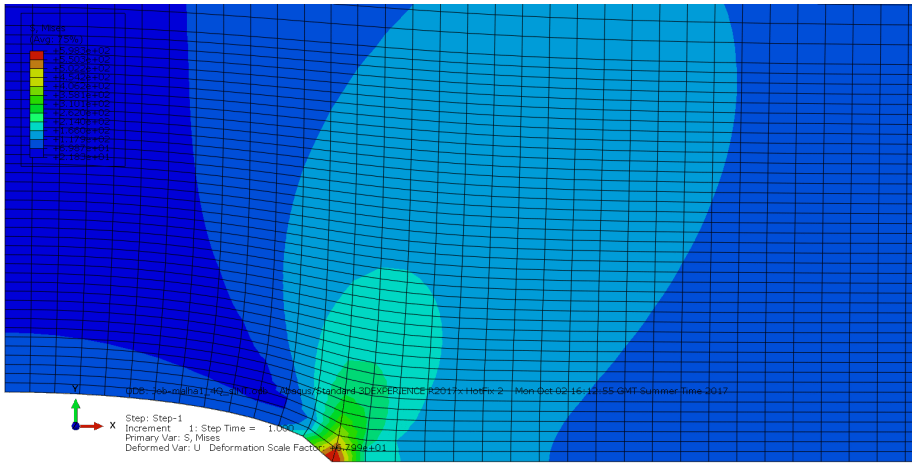


Figure A.4: Mesh 1 for 1/4 plate (CPS4) - von Mises stress

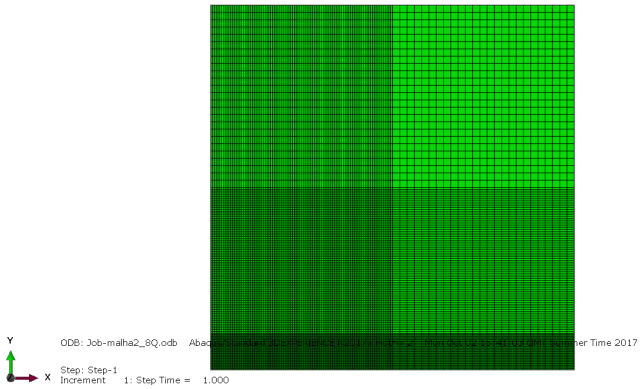


Figure A.5: Mesh 1 for 1/4 plate - CPS8R

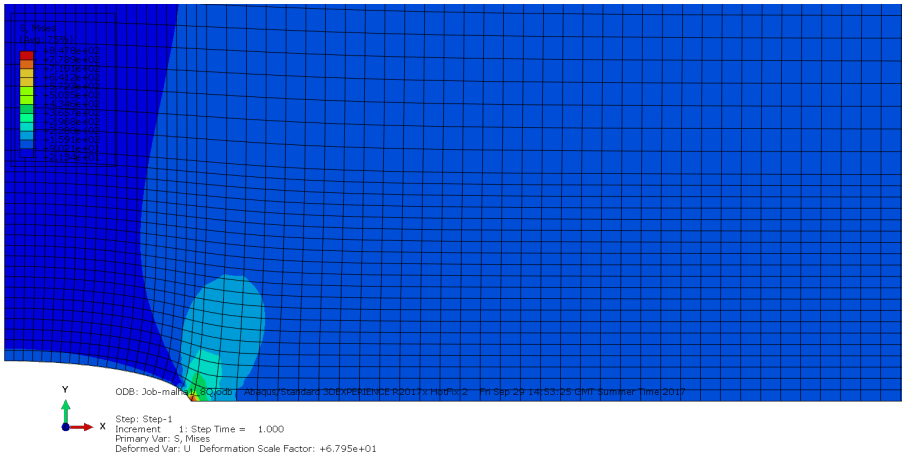


Figure A.6: Mesh 1 for 1/4 plate (CPS8R) - von Mises stress

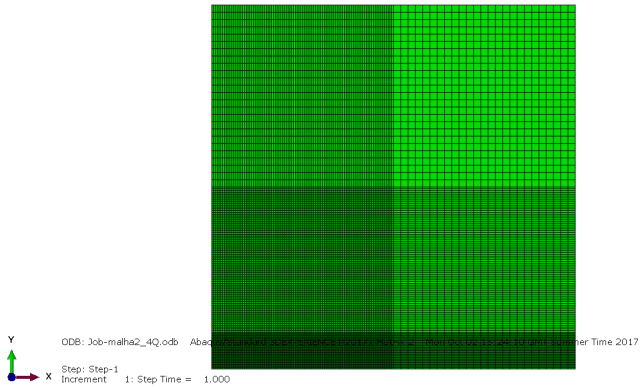


Figure A.7: Mesh 2 for 1/4 plate - CPS4R

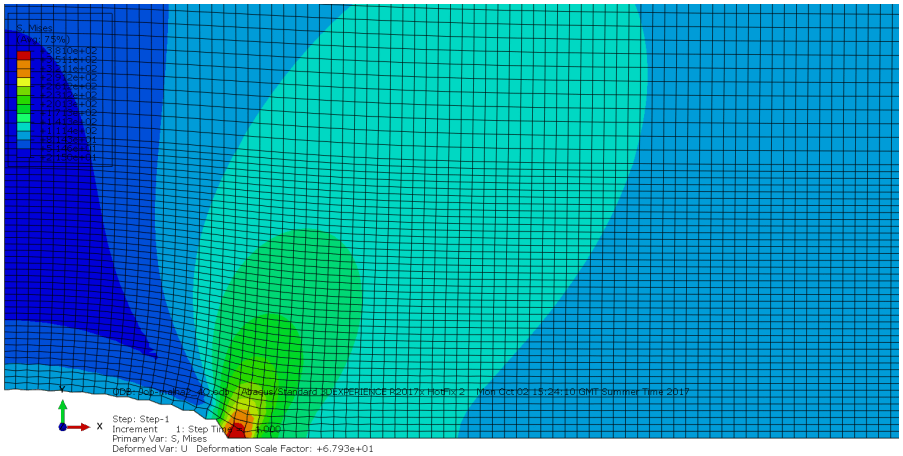


Figure A.8: Mesh 2 for 1/4 plate (CPS4R) - von Mises stress

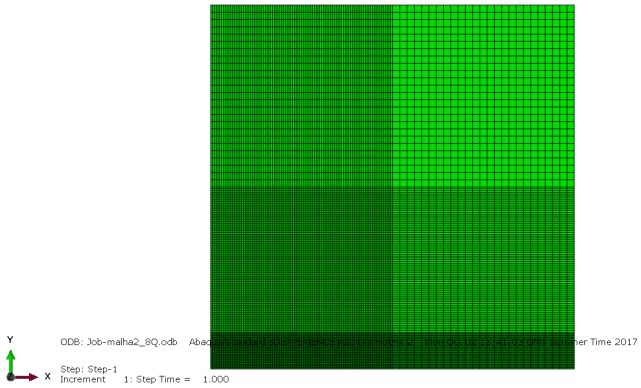


Figure A.9: Mesh 2 for 1/4 plate - CPS8R

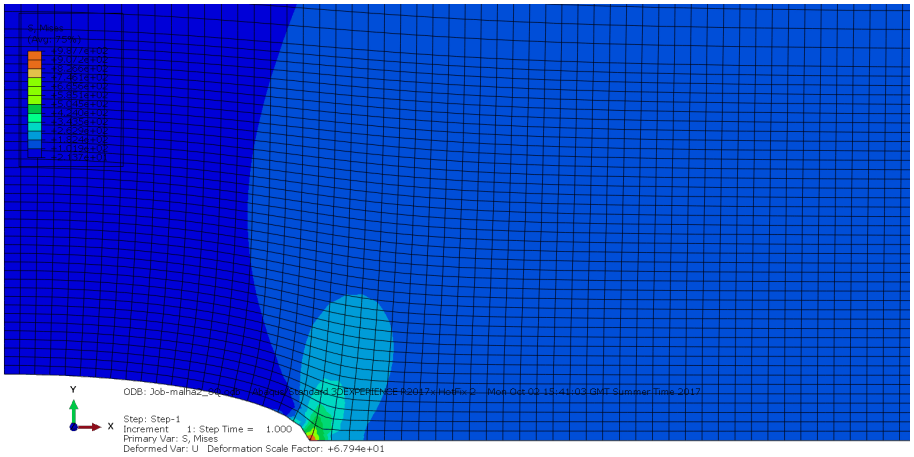


Figure A.10: Mesh 2 for 1/4 plate (CPS8R) - von Mises stress

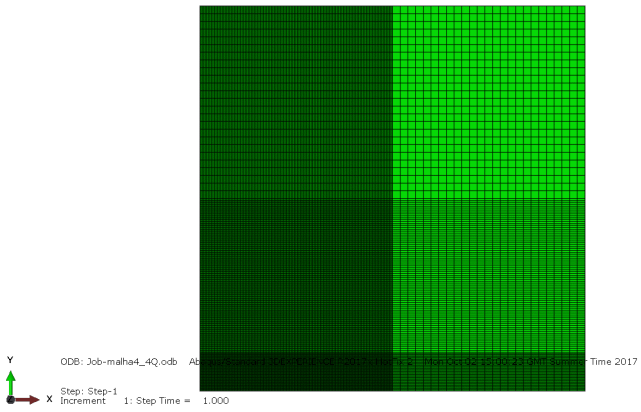


Figure A.11: Mesh 3 for 1/4 plate - CPS4R

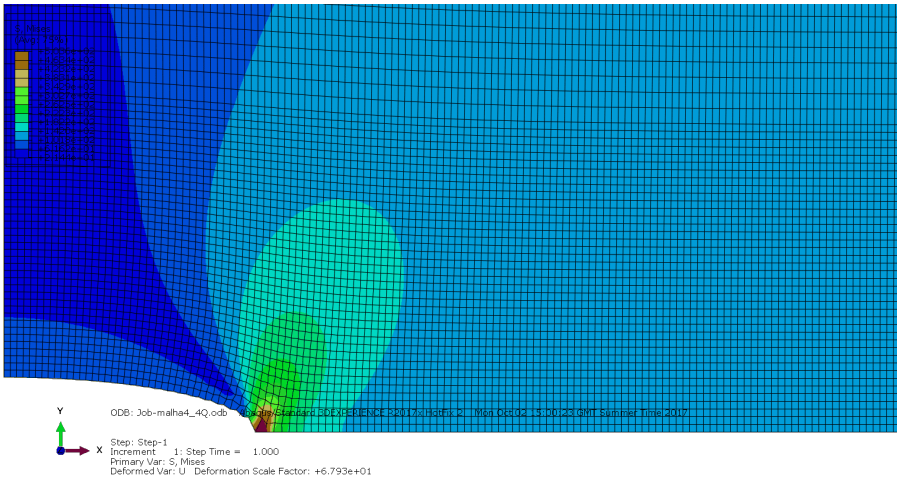


Figure A.12: Mesh 3 for 1/4 plate (CPS4R) - von Mises stress

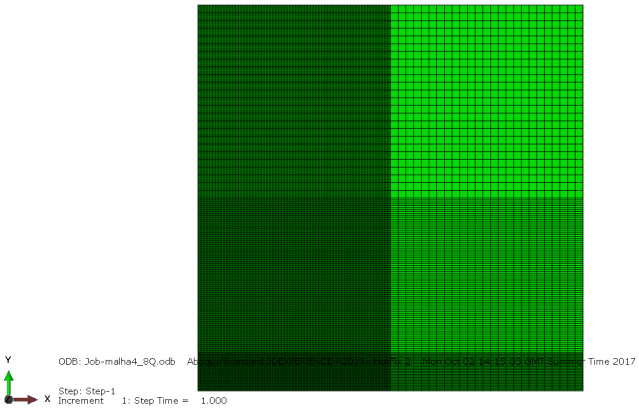


Figure A.13: Mesh 3 for 1/4 plate - CPS8R

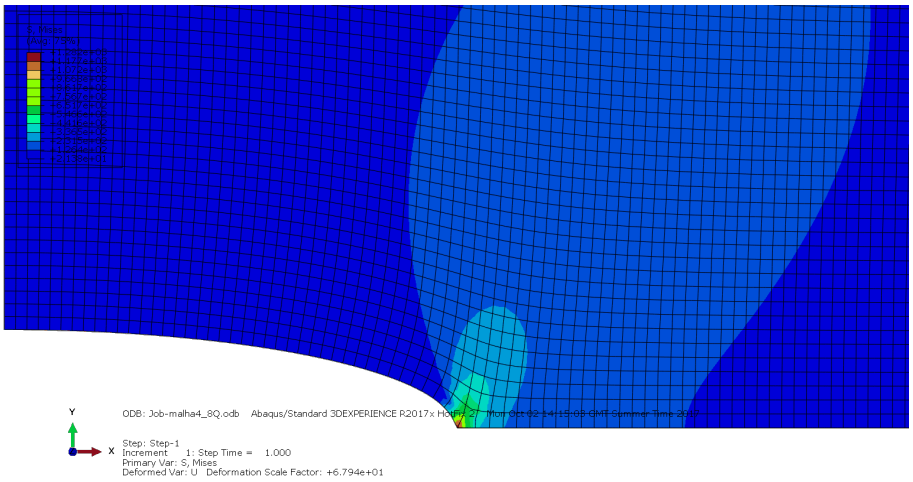


Figure A.14: Mesh 3 for 1/4 plate ($a = 1$, CPS8R) - von Mises stress

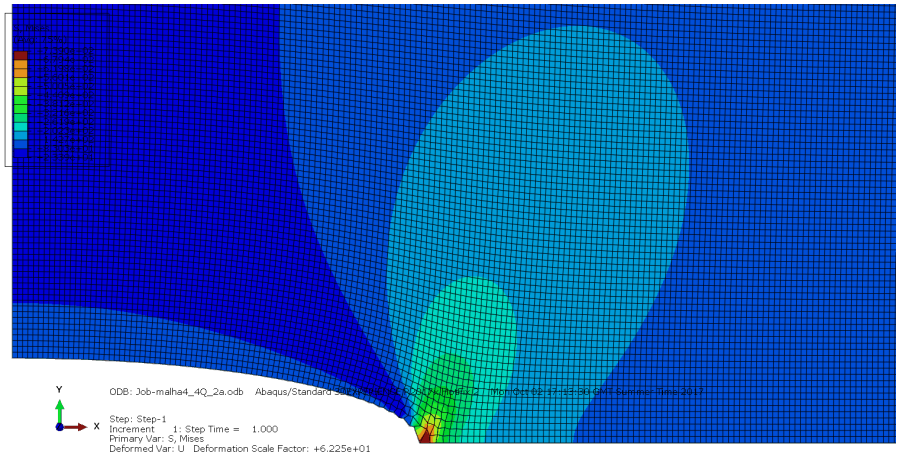


Figure A.15: Mesh 3 for 1/4 plate ($a = 2$, CPS4R) - von Mises stress

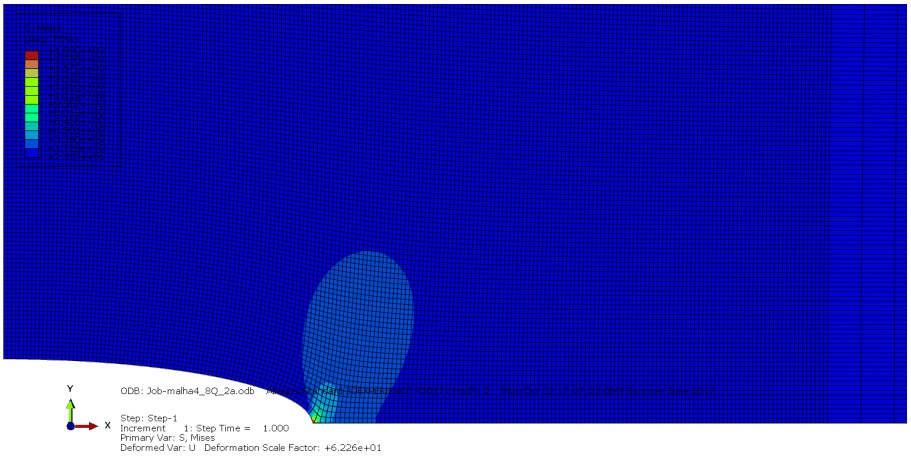


Figure A.16: Mesh 3 for 1/4 plate ($a = 2$, CPS8R) - von Mises stress

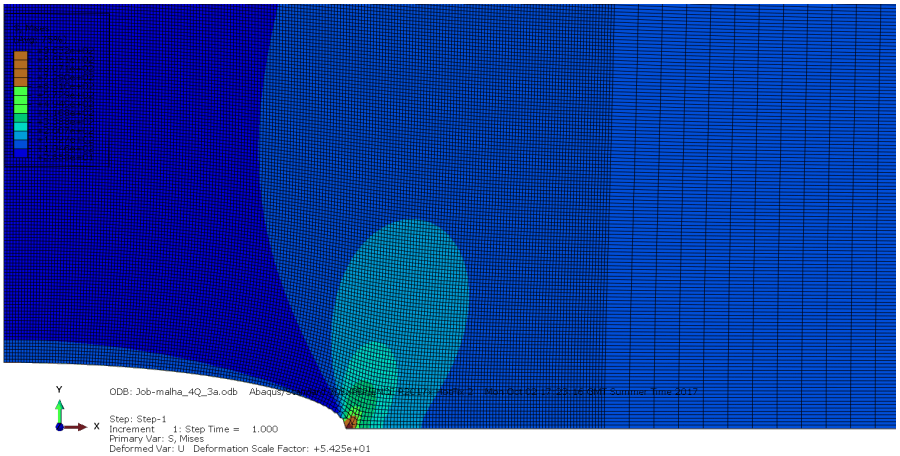


Figure A.17: Mesh 3 for 1/4 plate ($a = 3$, CPS4R) - von Mises stress

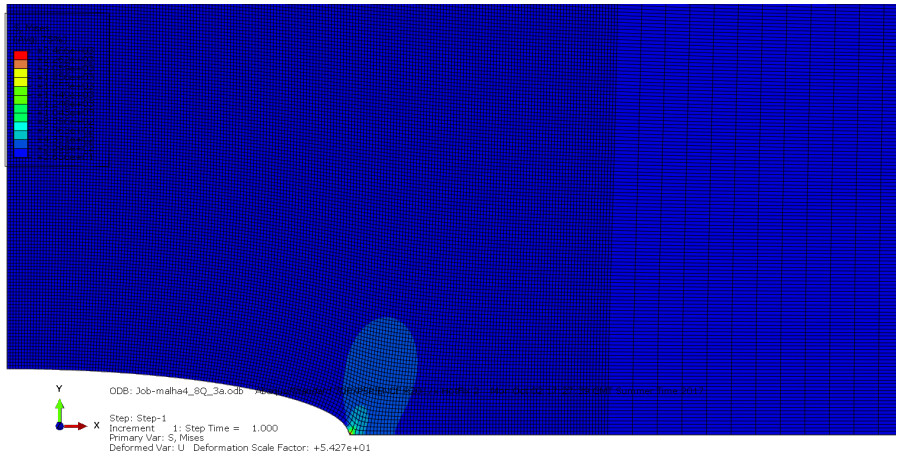


Figure A.18: Mesh 3 for 1/4 plate ($a = 3$, CPS8R) - von Mises stress

Annex B

Pre study case 2 ABAQUS models

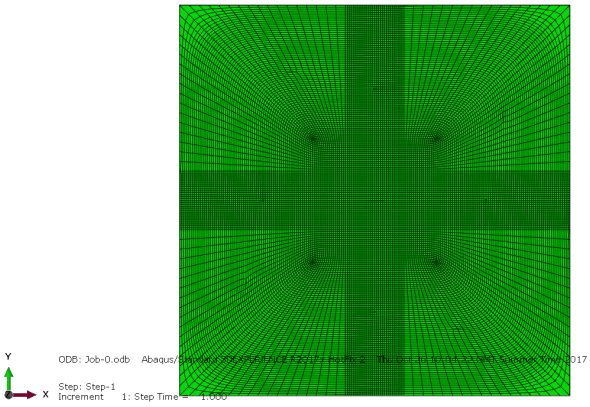


Figure B.1: Infinite plate with inclined crack $\alpha = 0°$ - Mesh

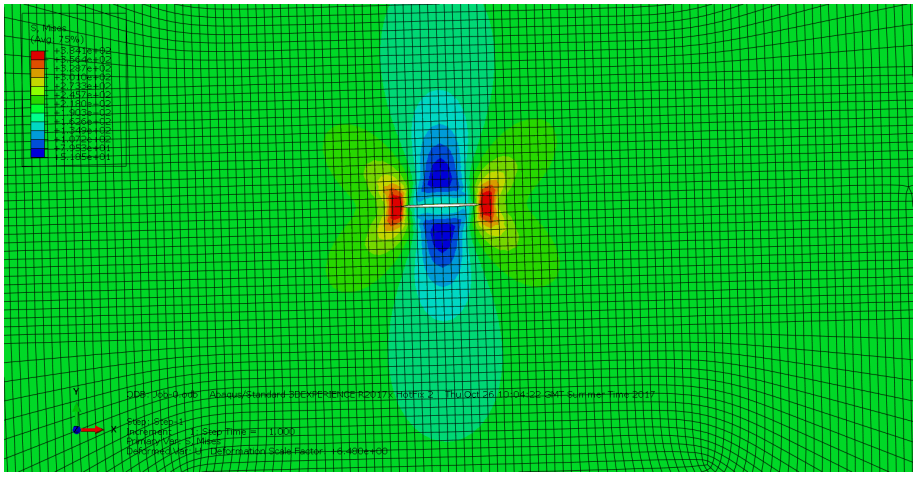


Figure B.2: Infinite plate with inclined crack $\alpha = 0°$ - von Mises stress

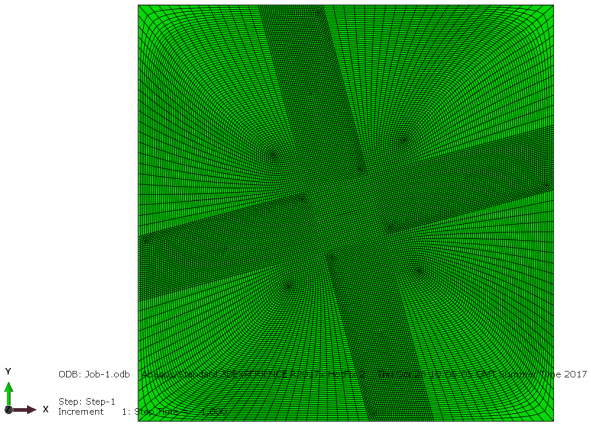


Figure B.3: Infinite plate with inclined crack $\alpha = 15°$ - Mesh

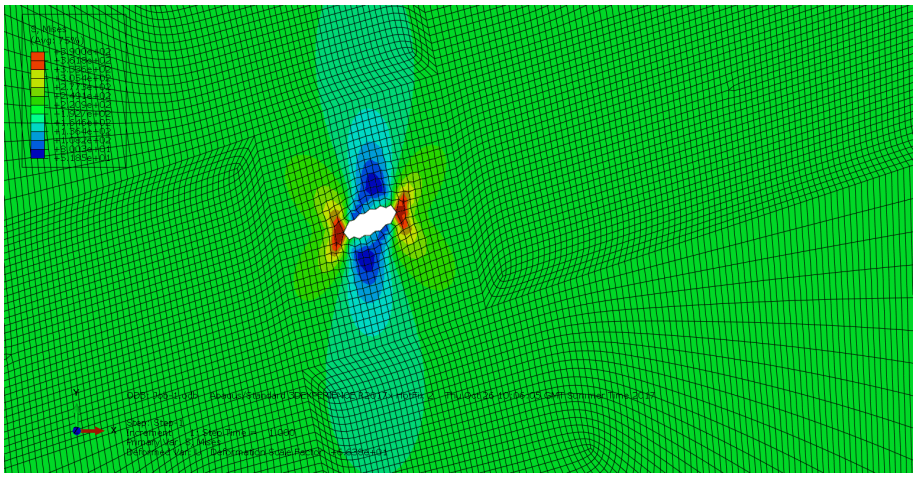


Figure B.4: Infinite plate with inclined crack $\alpha = 15°$ - von Mises stress

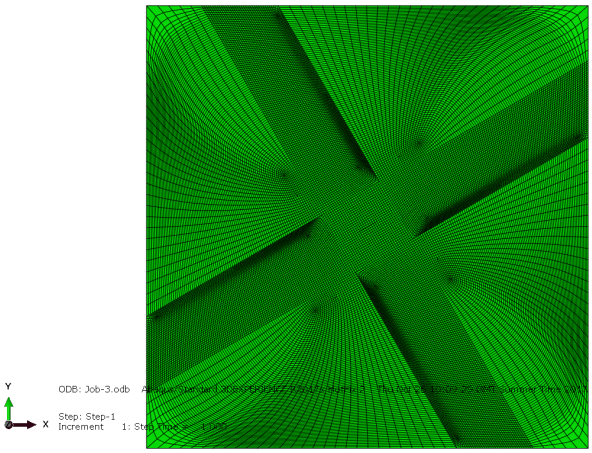


Figure B.5: Infinite plate with inclined crack $\alpha = 30°$ - Mesh

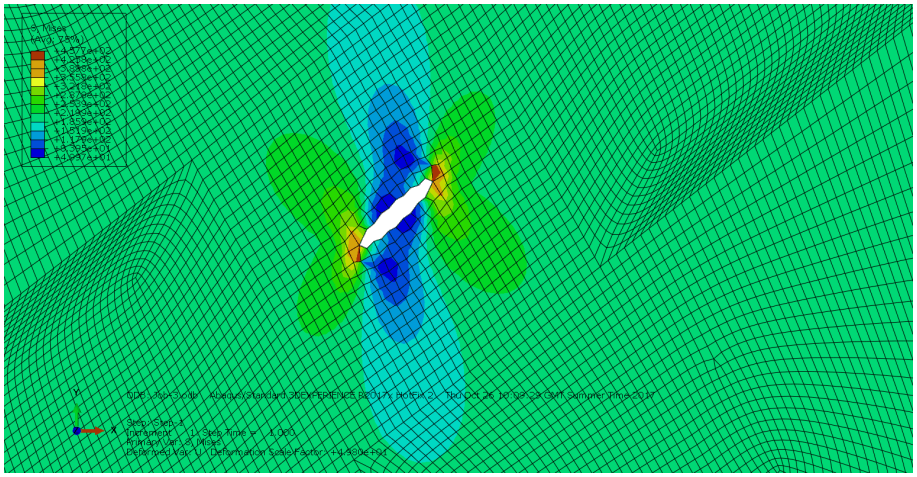


Figure B.6: Infinite plate with inclined crack $\alpha = 30°$ - von Mises stress

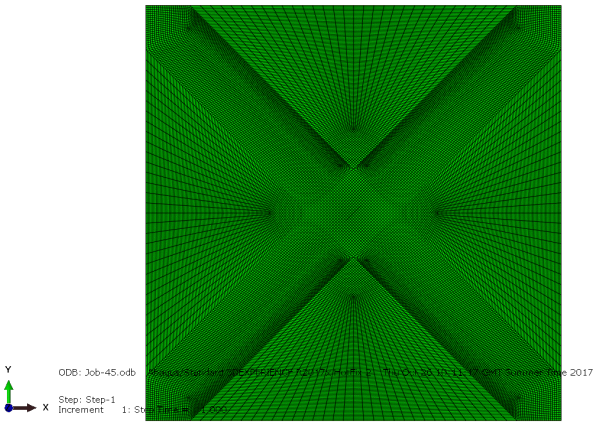


Figure B.7: Infinite plate with inclined crack $\alpha = 45°$ - Mesh

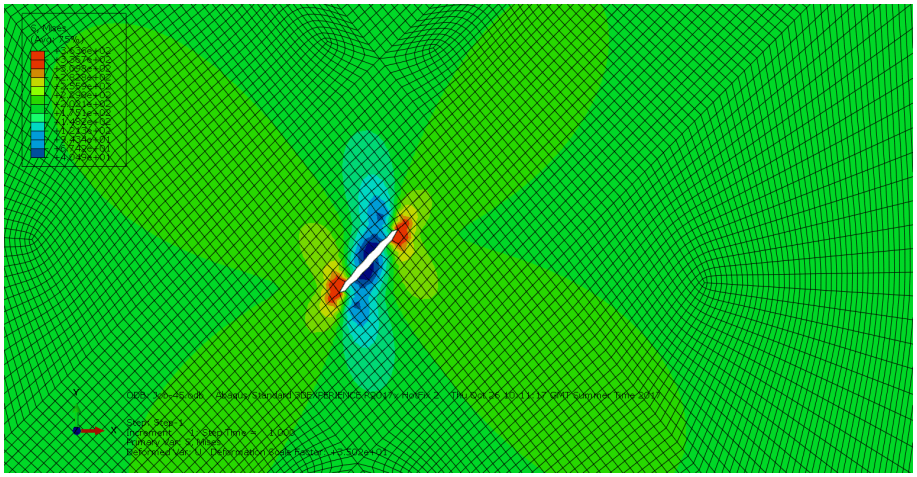


Figure B.8: Infinite plate with inclined crack $\alpha = 45°$ - von Mises stress

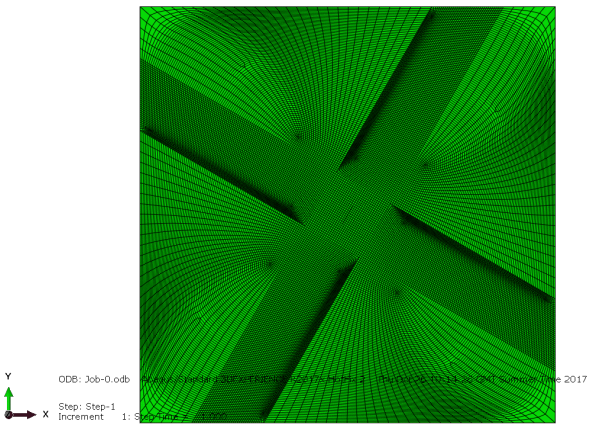


Figure B.9: Infinite plate with inclined crack $\alpha = 60°$ - Mesh

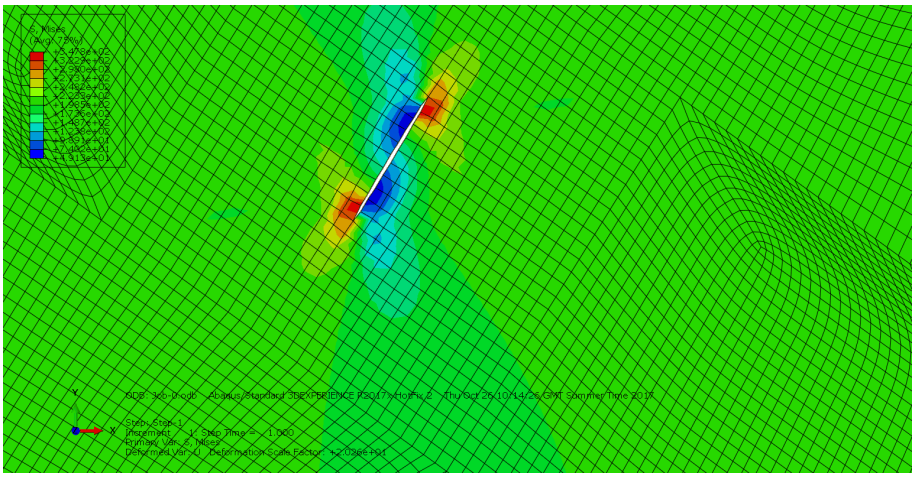


Figure B.10: Infinite plate with inclined crack $\alpha = 60°$ - von Mises stress

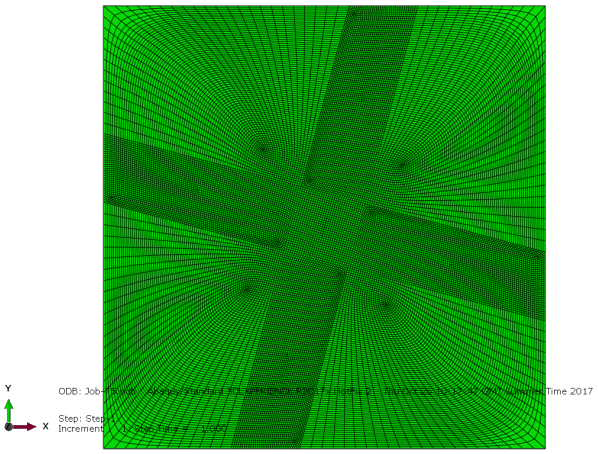


Figure B.11: Infinite plate with inclined crack $\alpha = 75°$ - Mesh

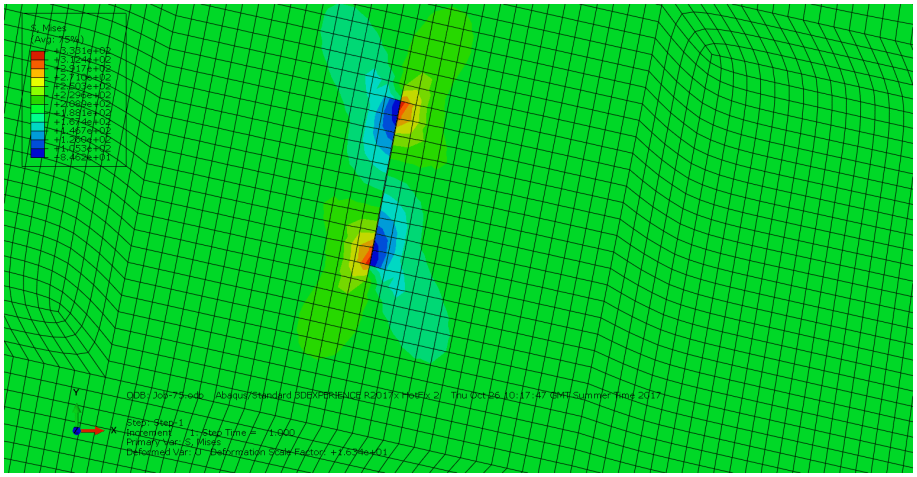


Figure B.12: Infinite plate with inclined crack $\alpha = 75°$ - von Mises stress

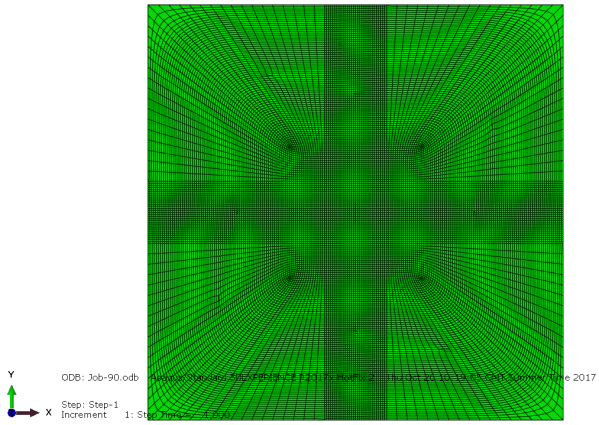


Figure B.13: Infinite plate with inclined crack $\alpha = 90°$ - Mesh

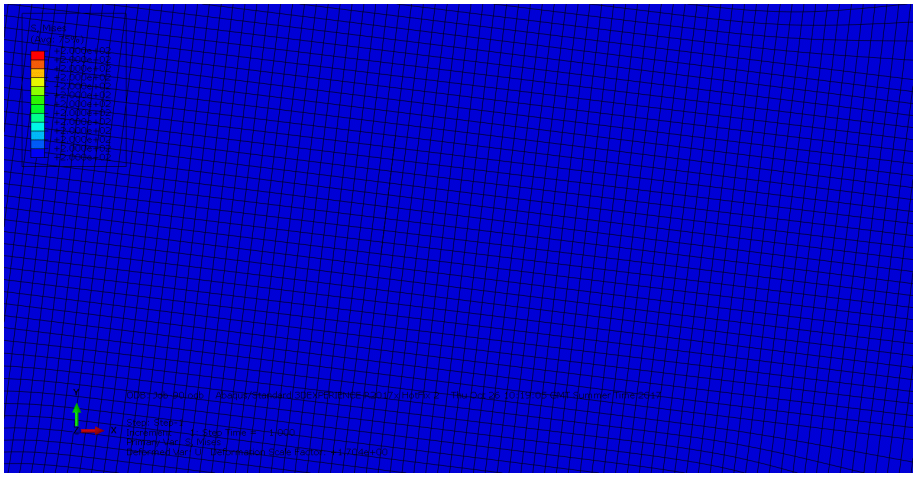


Figure B.14: Infinite plate with inclined crack $\alpha = 90°$ - von Mises stress

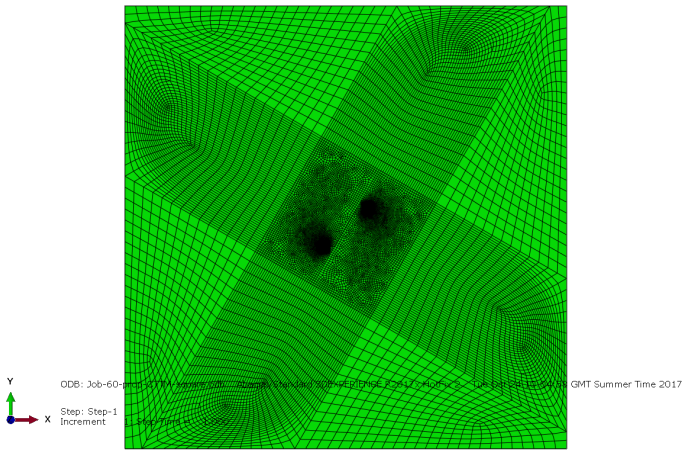


Figure B.15: Plate with inclined crack ($\alpha = 60°, \Delta a = 0.5$) using the MTS criteria - Mesh

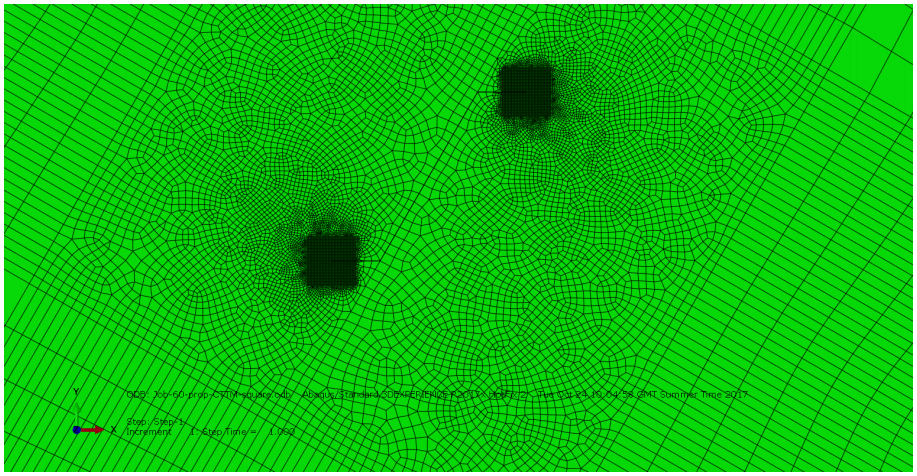


Figure B.16: Plate with inclined crack ($\alpha = 60°, \Delta a = 0.5$) using the MTS criteria - Mesh

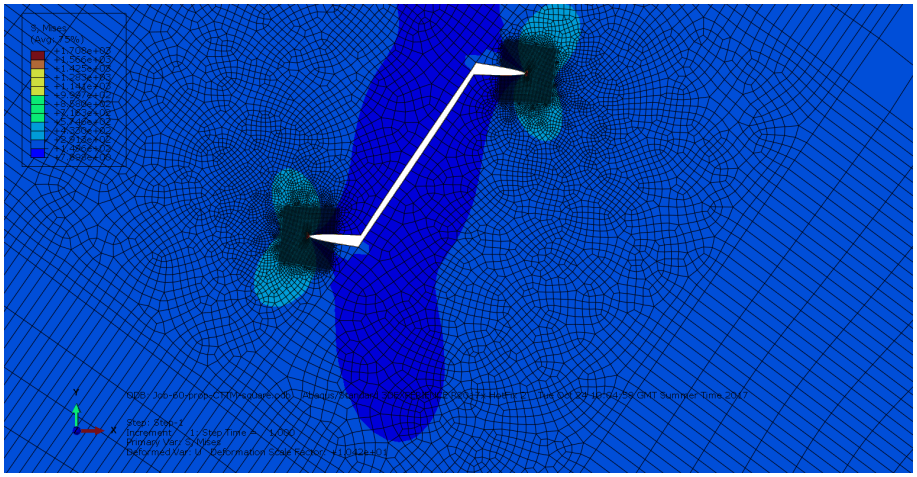


Figure B.17: Plate with inclined crack ($\alpha = 60°, \Delta a = 0.5$) using the MTS criteria - von Mises stress

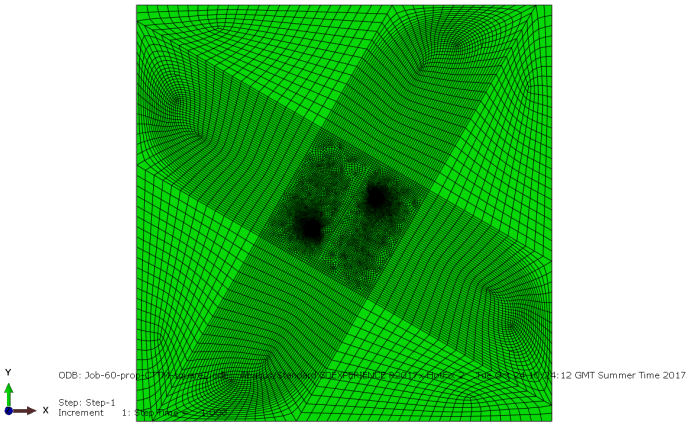


Figure B.18: Plate with inclined crack ($\alpha = 60°, \Delta a = 1$) using the MTS criteria - Mesh

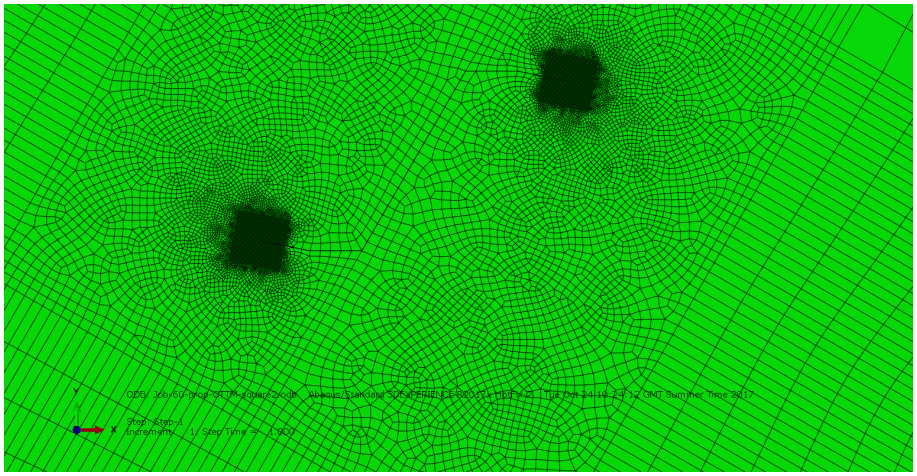


Figure B.19: Plate with inclined crack ($\alpha = 60°, \Delta a = 1$) using the MTS criteria - Mesh

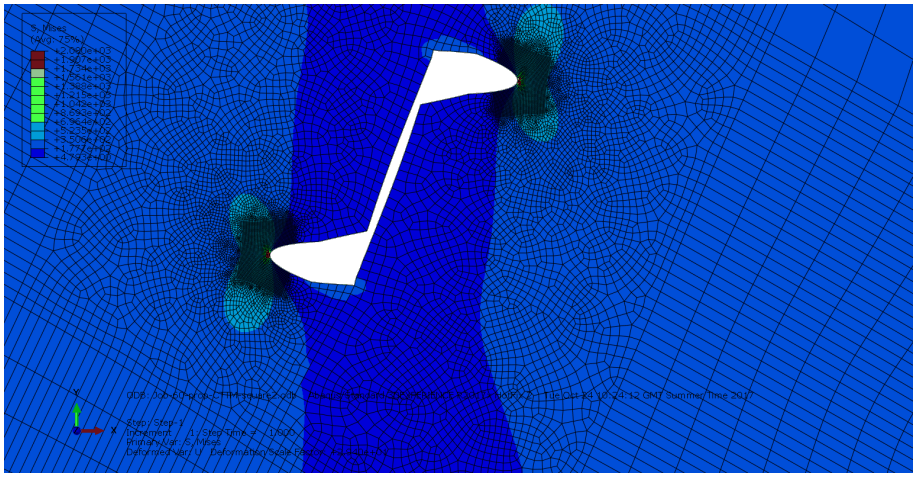


Figure B.20: Plate with inclined crack ($\alpha = 60°, \Delta a = 1$) using the MTS criteria - von Mises stress

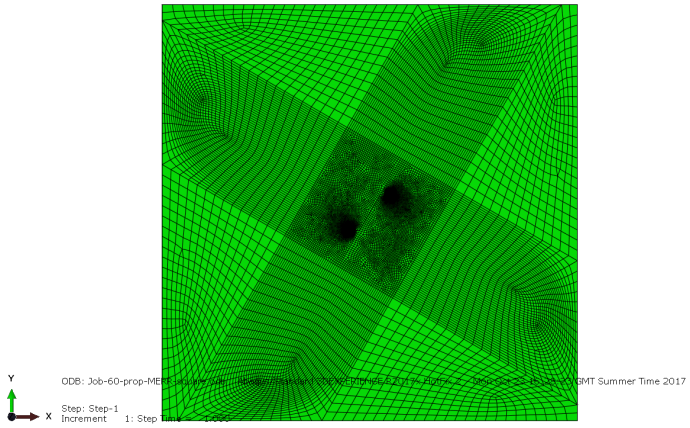


Figure B.21: Plate with inclined crack ($\alpha = 60°, \Delta a = 0.5$) using the MERR criteria - Mesh

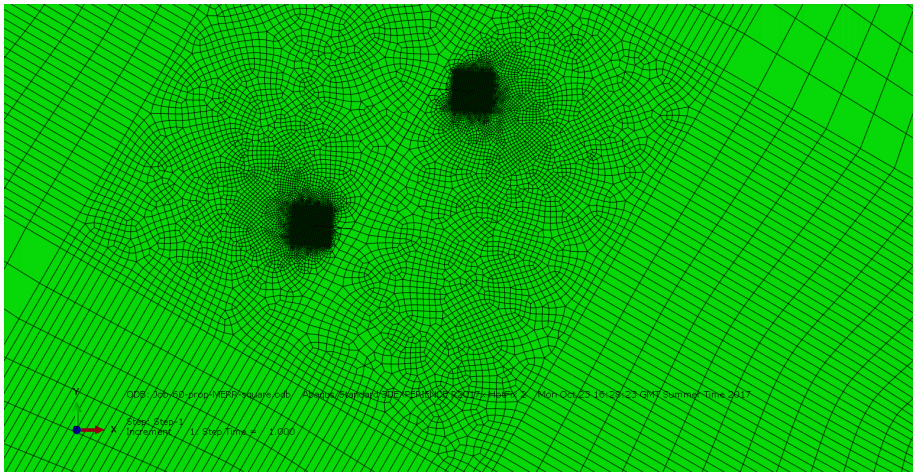


Figure B.22: Plate with inclined crack ($\alpha = 60°, \Delta a = 0.5$) using the MERR criteria - Mesh

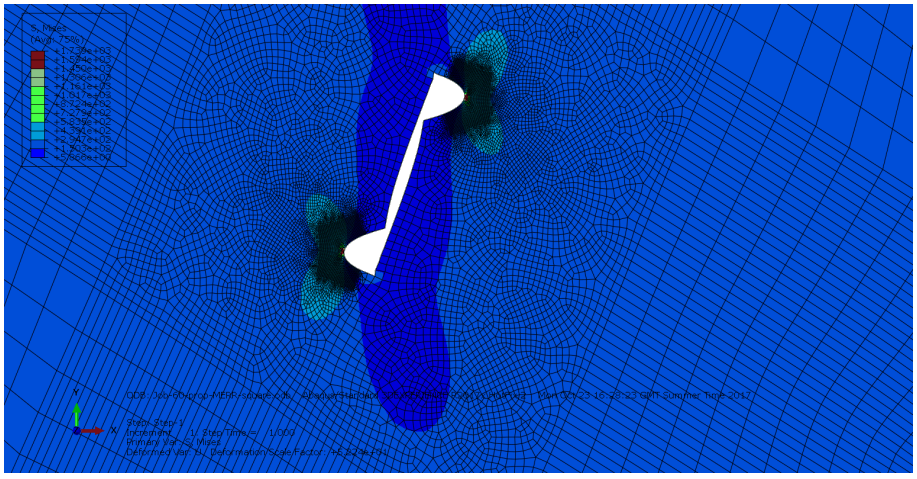


Figure B.23: Plate with inclined crack ($\alpha = 60°, \Delta a = 0.5$) using the MERR criteria - von Mises stress

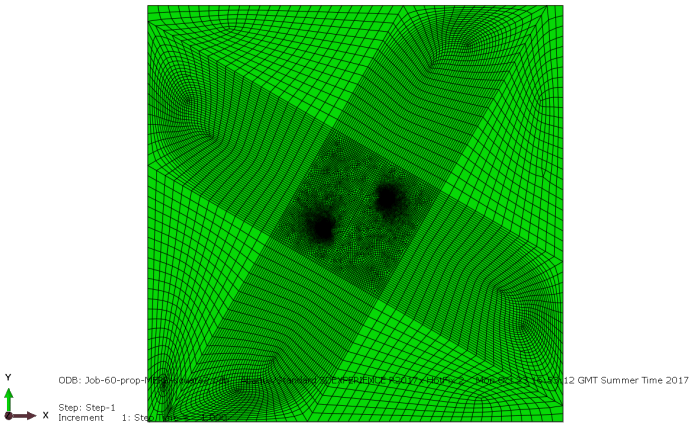


Figure B.24: Plate with inclined crack ($\alpha = 60°, \Delta a = 1$) using the MERR criteria - Mesh

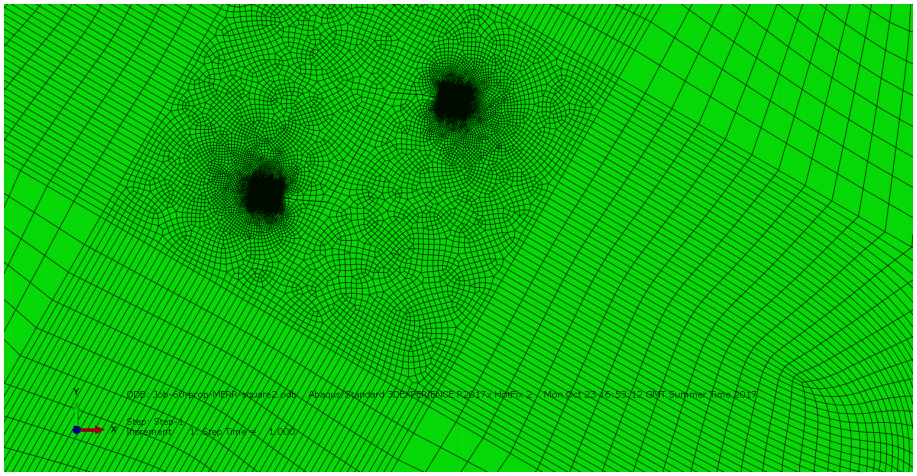


Figure B.25: Plate with inclined crack ($\alpha = 60°, \Delta a = 1$) using the MERR criteria - Mesh

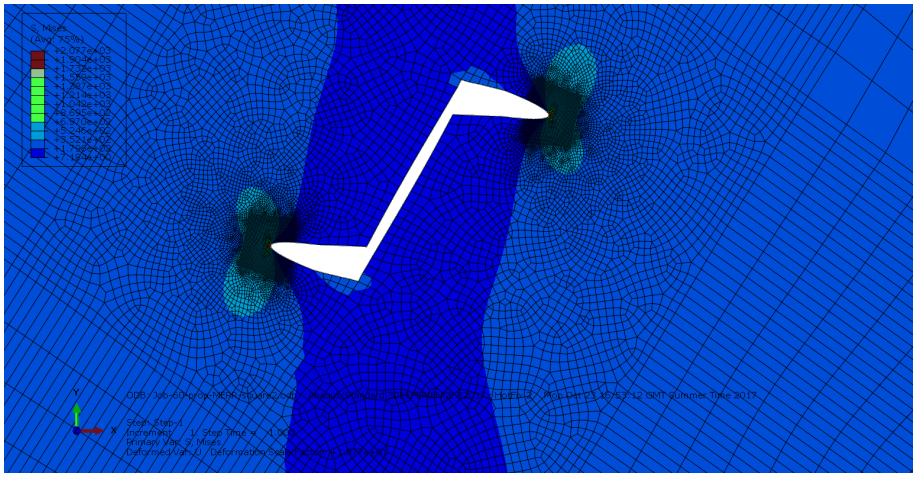


Figure B.26: Plate with inclined crack ($\alpha = 60°, \Delta a = 1$) using the MERR criteria - von Mises stress

Annex C

Experimental procedures ABAQUS models

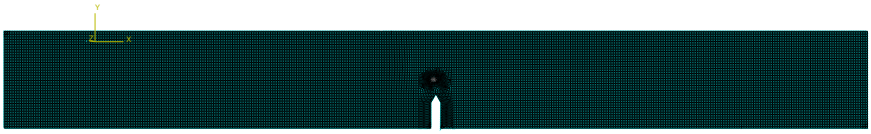


Figure C.1: Specimen 1 Mesh (CPS4 elements) - Pre-crack

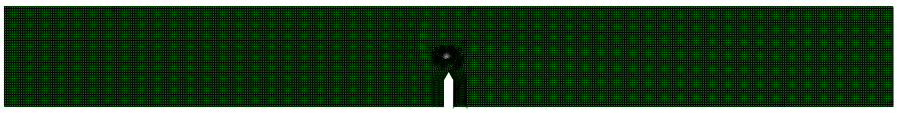


Figure C.2: Specimen 1 Mesh (CPS4 elements) - Pre-crack (undeformed)

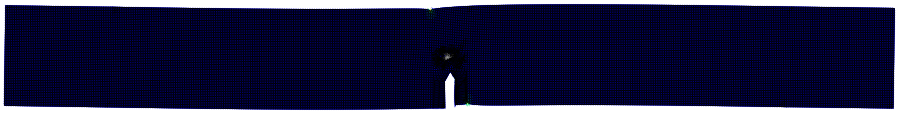


Figure C.3: Specimen 1 Mesh (CPS4 elements) - Pre-crack (deformed)

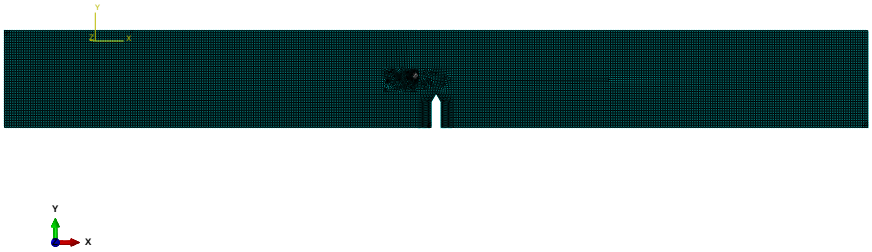


Figure C.4: Specimen 1 Mesh (CPS4 elements) - Photo 1

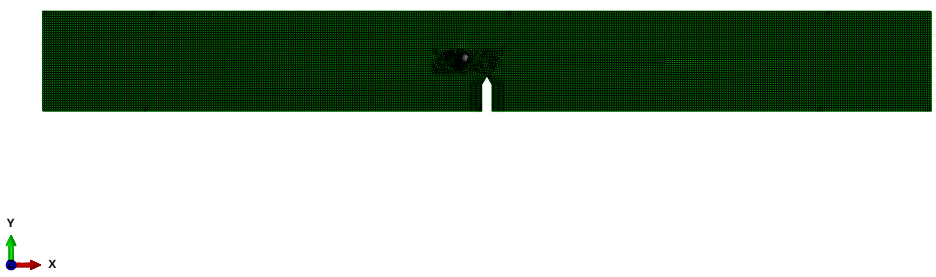


Figure C.5: Specimen 1 Mesh (CPS4 elements) - Photo 1 (undeformed)

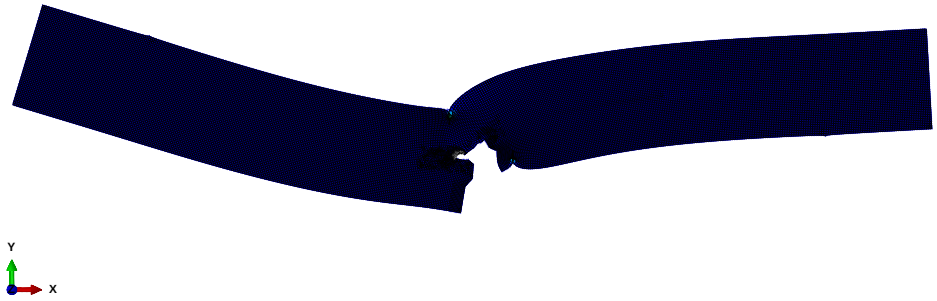


Figure C.6: Specimen 1 Mesh (CPS4 elements) - Photo 1 (deformed)

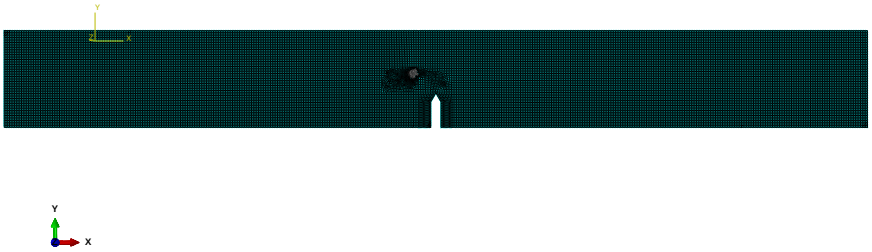


Figure C.7: Specimen 1 Mesh (CPS4 elements) - Photo 2

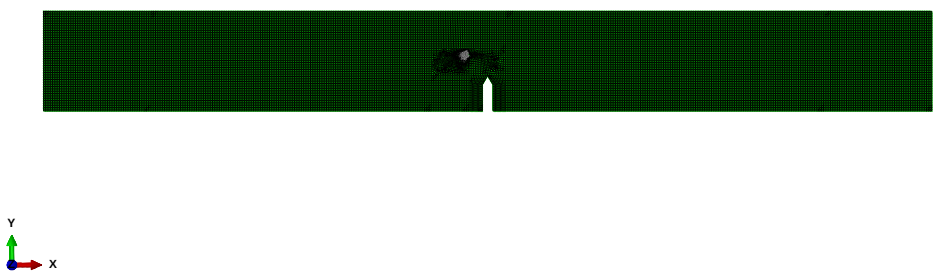


Figure C.8: Specimen 1 Mesh (CPS4 elements) - Photo 2 (undeformed)

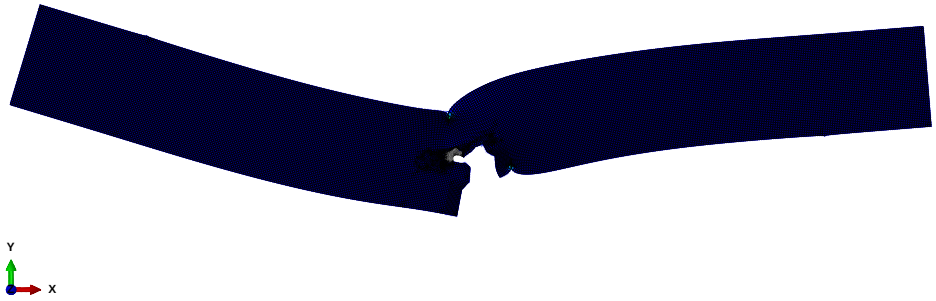


Figure C.9: Specimen 1 Mesh (CPS4 elements) - Photo 2 (deformed)

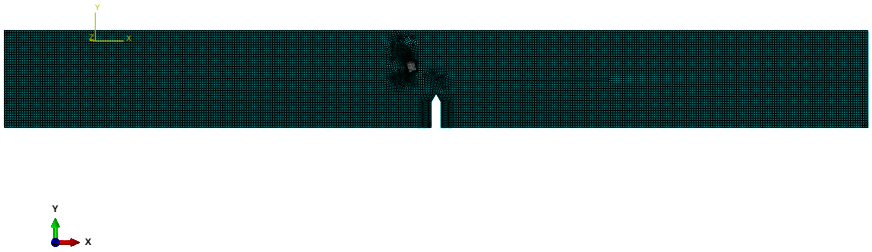


Figure C.10: Specimen 1 Mesh (CPS4 elements) - Photo 3

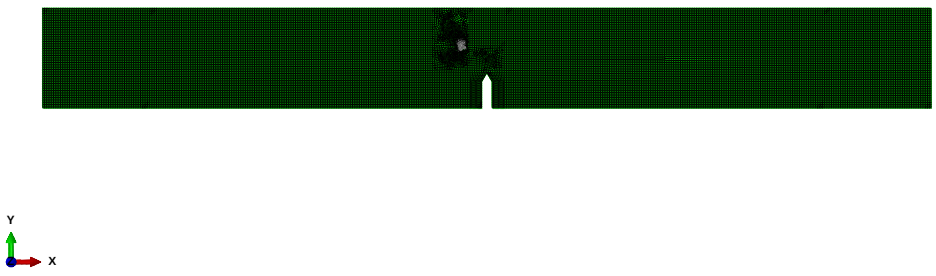


Figure C.11: Specimen 1 Mesh (CPS4 elements) - Photo 3 (undeformed)

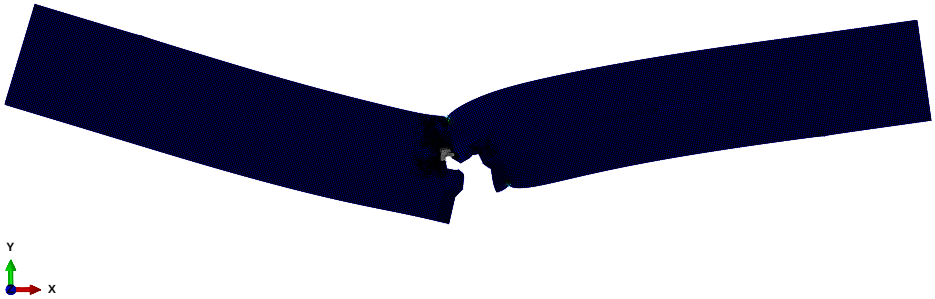


Figure C.12: Specimen 1 Mesh (CPS4 elements) - Photo (deformed)

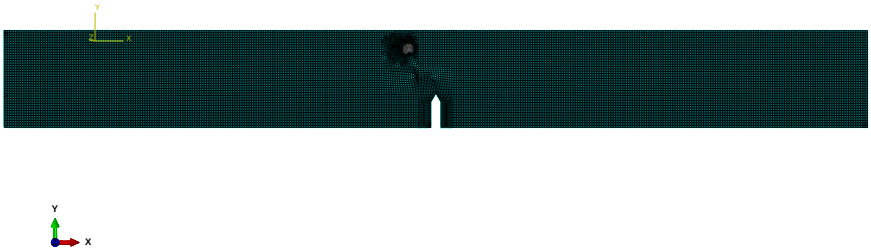


Figure C.13: Specimen 1 Mesh (CPS4 elements) - Photo 4

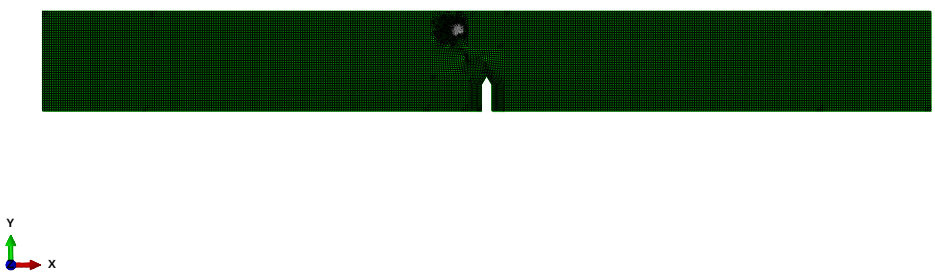


Figure C.14: Specimen 1 Mesh (CPS4 elements) - Photo 4 (undeformed)

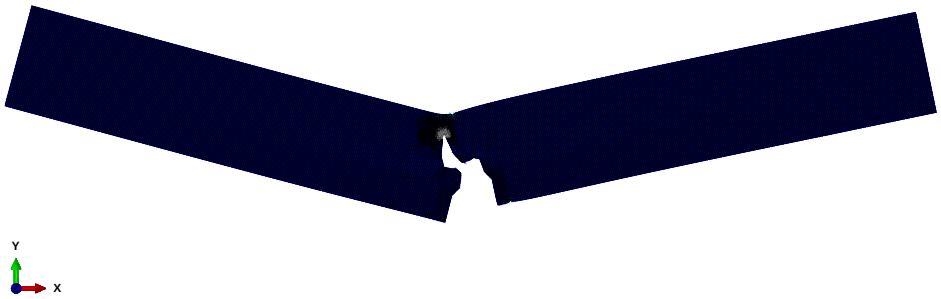


Figure C.15: Specimen 1 Mesh (CPS4 elements) - Photo (deformed)

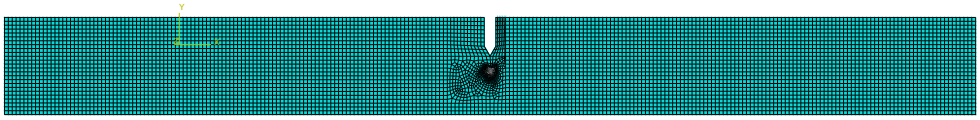


Figure C.16: Specimen 3 Mesh (CPS4 elements) - Pre-crack

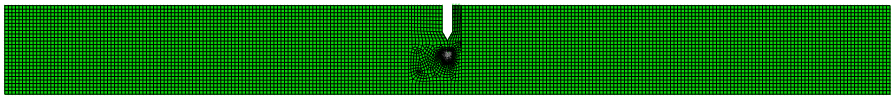


Figure C.17: Specimen 3 Mesh (CPS4 elements) - Pre-crack (undeformed)

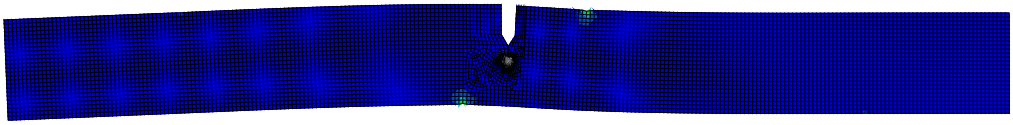


Figure C.18: Specimen 3 Mesh (CPS4 elements) - Pre-crack (deformed)

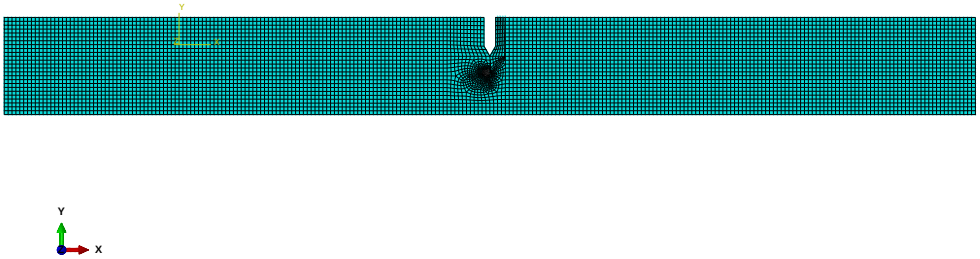


Figure C.19: Specimen 3 Mesh (CPS4 elements) - Photo 1

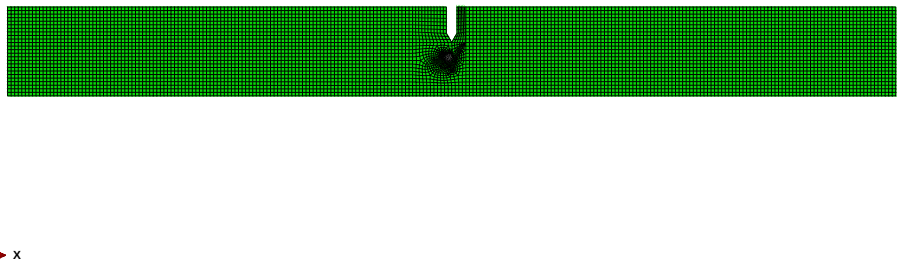


Figure C.20: Specimen 3 Mesh (CPS4 elements) - Photo 1 (undeformed)

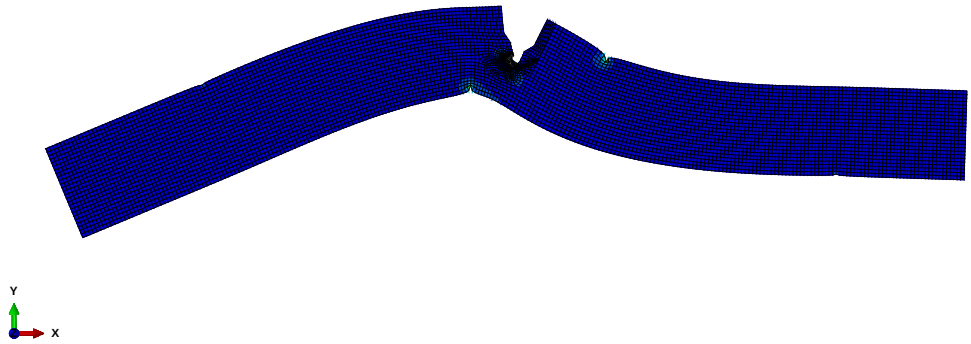


Figure C.21: Specimen 3 Mesh (CPS4 elements) - Photo 1 (deformed)

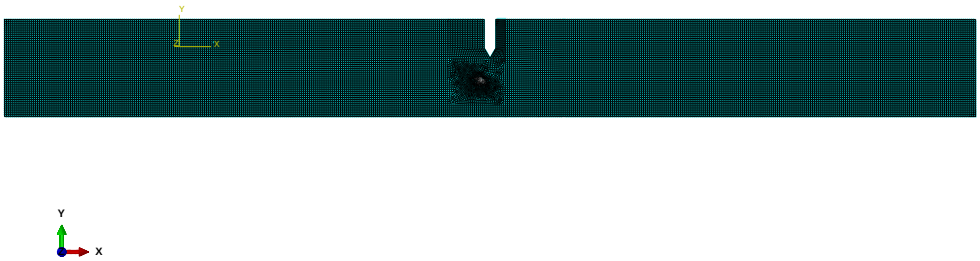


Figure C.22: Specimen 3 Mesh (CPS4 elements) - Photo 2

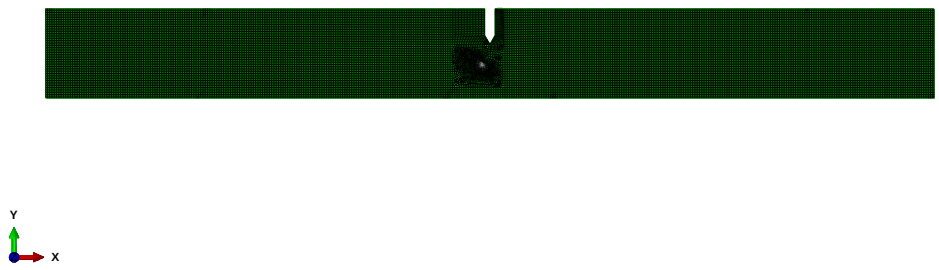


Figure C.23: Specimen 3 Mesh (CPS4 elements) - Photo 2 (undeformed)

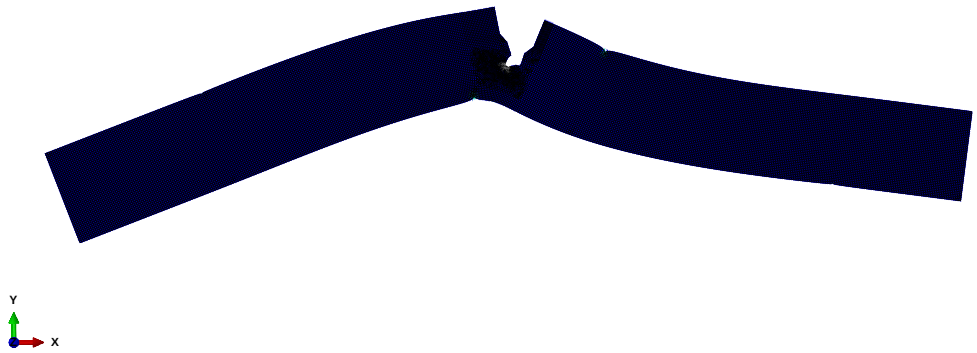


Figure C.24: Specimen 3 Mesh (CPS4 elements) - Photo 2 (deformed)

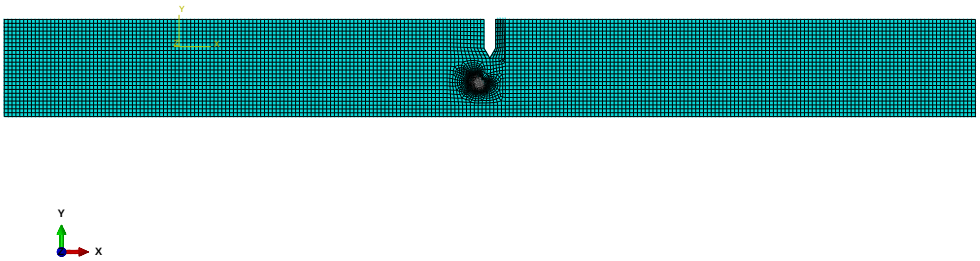


Figure C.25: Specimen 3 Mesh (CPS4 elements) - Photo 3

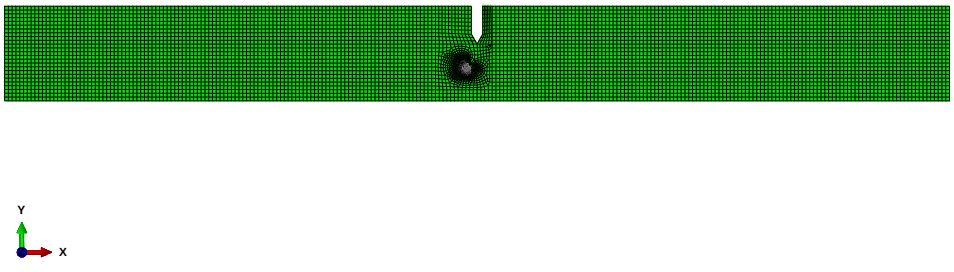


Figure C.26: Specimen 3 Mesh (CPS4 elements) - Photo 3 (undeformed)

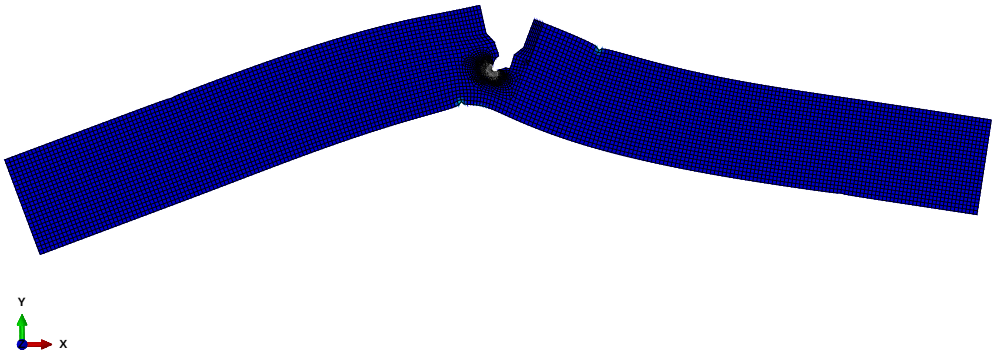


Figure C.27: Specimen 3 Mesh (CPS4 elements) - Photo 3 (deformed)

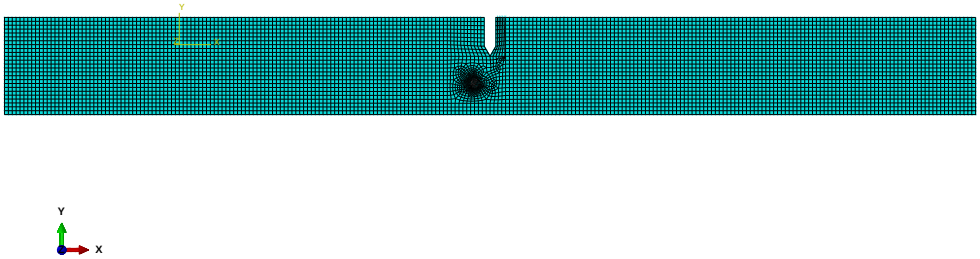


Figure C.28: Specimen 3 Mesh (CPS4 elements) - Photo 4

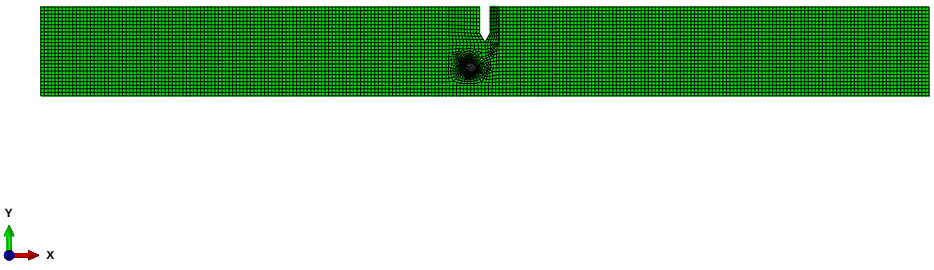


Figure C.29: Specimen 3 Mesh (CPS4 elements) - Photo 4 (undeformed)

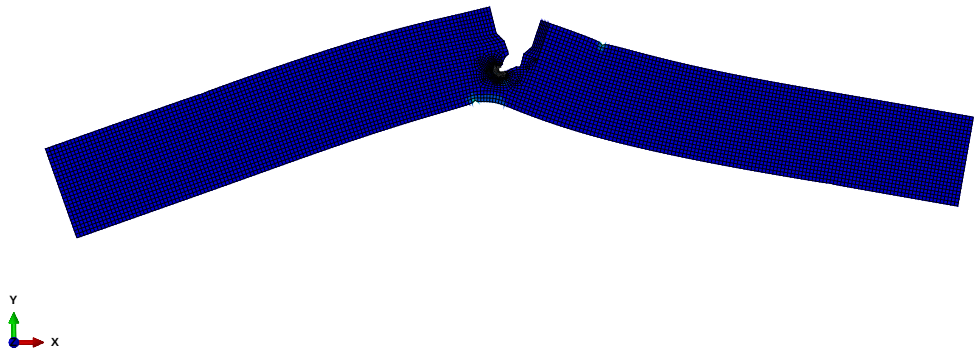


Figure C.30: Specimen 3 Mesh (CPS4 elements) - Photo 4 (deformed)

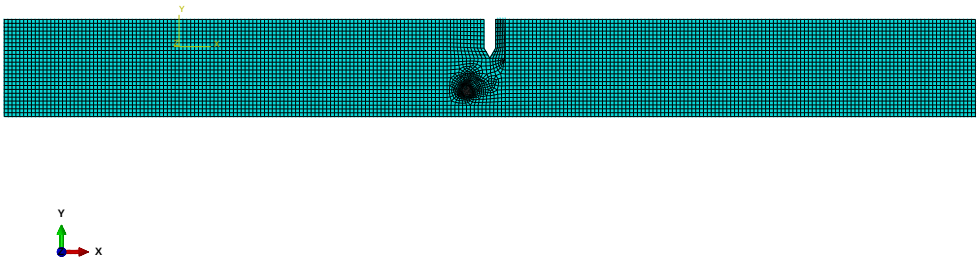


Figure C.31: Specimen 3 Mesh (CPS4 elements) - Photo 5

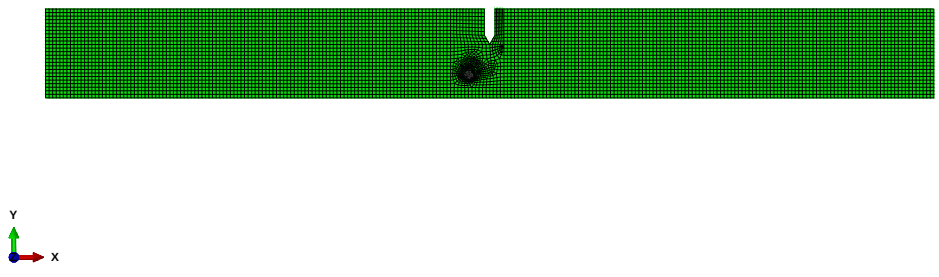


Figure C.32: Specimen 3 Mesh (CPS4 elements) - Photo 5 (undeformed)

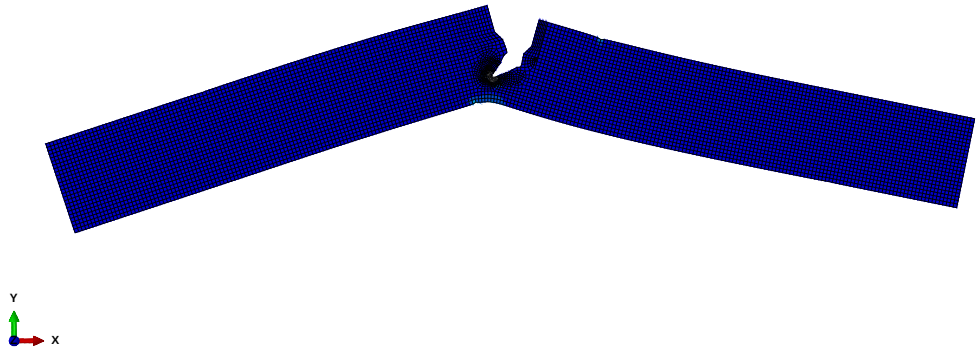


Figure C.33: Specimen 3 Mesh (CPS4 elements) - Photo 5 (deformed)